

CHARACTERIZATION OF SOOT IN TRAPPING AND OXIDATION PROCESS ON
METALLIC MICROFIBER PARTIAL FLOW DIESEL PARTICULATE FILTER



A THESIS REPORT SUBMITTED IN PARTIAL FULFILLMENT
OF THE REQUIREMENTS FOR THE DEGREE OF
MASTER OF ENGINEERING IN AUTOMOTIVE AND
ADVANCED TRANSPORTATION ENGINEERING
SCHOOL OF ENGINEERING
KING MONGKUT'S INSTITUTE OF TECHNOLOGY LADKRABANG
ACADEMIC YEAR 2022
KMITL-2022-EN-M-037-083

This material is reserved for educational use only, not allowed for commercial use.

Forbidden to modify the content, and cite the document when use.

CHARACTERIZATION OF SOOT IN TRAPPING AND OXIDATION PROCESS ON
METALLIC MICROFIBER PARTIAL FLOW DIESEL PARTICULATE FILTER



A THESIS REPORT SUBMITTED IN PARTIAL FULFILLMENT
OF THE REQUIREMENTS FOR THE DEGREE OF
MASTER OF ENGINEERING IN AUTOMOTIVE AND
ADVANCED TRANSPORTATION ENGINEERING
SCHOOL OF ENGINEERING
KING MONGKUT'S INSTITUTE OF TECHNOLOGY LADKRABANG
ACADEMIC YEAR 2022

KMITL-2022-EN-M-037-083

This material is reserved for educational use only, not allowed for commercial use.

Forbidden to modify the content, and cite the document when use.



COPYRIGHT 2022

SCHOOL OF ENGINEERING

KING MONGKUT'S INSTITUTE OF TECHNOLOGY LADKRABANG

This material is reserved for educational use only, not allowed for commercial use.

Forbidden to modify the content, and cite the document when use.

THESIS TITLE	Characterization of Soot in Trapping and Oxidation Process on Metallic Microfiber Partial Flow Diesel Particulate Filter
STUDENT	Ban-seok Oh
STUDENT ID	63601189
DEGREE	Master of Engineering
PROGRAM	Automotive and Advanced Transportation Engineering
THESIS ADVISOR	Assoc. Prof. Dr. Preechar Karin
CO-THESIS ADVISOR	Prof. Dr. Katsunori Hanamura

ABSTRACT

The metal fleece from a metallic microfiber partial flow diesel particulate filter (P-DPF) and PM in an exhaust after-treatment system consisting of a diesel oxidation catalyst (DOC) and P-DPF was analyzed in this research. The metal fibers that make up the metal fleece was covered by grains on the surface in a lengthwise linear manner. The material of the metal fleece and the metal foil were stainless steel alloys which consist of Fe, Cr, Al, and some C. Particulate matter (PM) trapping from an engine exhaust on the metal fleece was then observed. The metal fleece was also coated with ceria by physical vapor deposition to reduce the PM activation energy. Thermogravimetric analysis was done with model soot and real diesel PM on the metal fleece, without and with the catalyst coating. The catalyst coating reduced the activation energy of the model soot by 17% from 167 kJ/mol to 138 kJ/mol and for the diesel PM by 30% from 128 kJ/mol to 90 kJ/mol. Diesel PM had trace elements from the engine oil which were reduced by the DOC. Overall, the after-treatment system did not leak harmful elements into the PM. The agglomerate and primary particles of the PM increased in size as it travelled down the after-treatment system but with evidence of fragmentation. The nanostructure revealed that there was a decrease of graphitization and the crystallite sizes decreased along the after-treatment system. This was supported by measuring the opacity, temperature, CO₂, NO, and O₂ of the gas in the three stages of the exhaust after-treatment system.

Keywords: P-DPF, PM, Soot, Carbon Nanostructure, Exhaust After-treatment

ACKNOWLEDGEMENTS

First, I would like to thank the almighty I am for this opportunity to study what I want and where I want. I am grateful for my family, professors, and friends for their support during my studies and research.

My first special mention is to Professor Preechar for his patience, care, and knowledge during this period. Thank you to Dr. Sompong for his care, connections, and flexibility. I am indebted to Ajarn Witthawat for his experience, priceless help, and care for the sputtering experimentation and subsequent analysis. I am grateful for all the professors who lectured in our studies.

Special mention to the members of our laboratory: P'Palm, P'Bird, P'Bank, Phyo Wai, Leo, Myat, Ms. Zwemon, P'Ton, and P'Swe Zin. We have gone through quite a lot with the various experimentations, data analysis, seminars, meetings, and more. We would not have been able to do what we had without every member. Thank you again and best of luck in your future endeavors.

To my batch-mates, I'm sad that we were never able to meet during our studies, but I am glad to have shared experiences with various lectures and examinations. I also wish everyone the best of luck and blessings in your future endeavors. I was fortunate enough to become close with Phyo Wai and Leo because of our laboratory. Thank you again for being there and I am glad that we were able to know each other.

To the staff of TAIST-TokyoTech, NCTC, MTEC, KMITL Mechanical Engineering Department, KMITL Engineering Graduate School, and others, Thank you for your hard work and allowing my studies to be so smooth and without major inconveniences.

Ban-seok Oh

21th December 2022.

TABLE OF CONTENTS

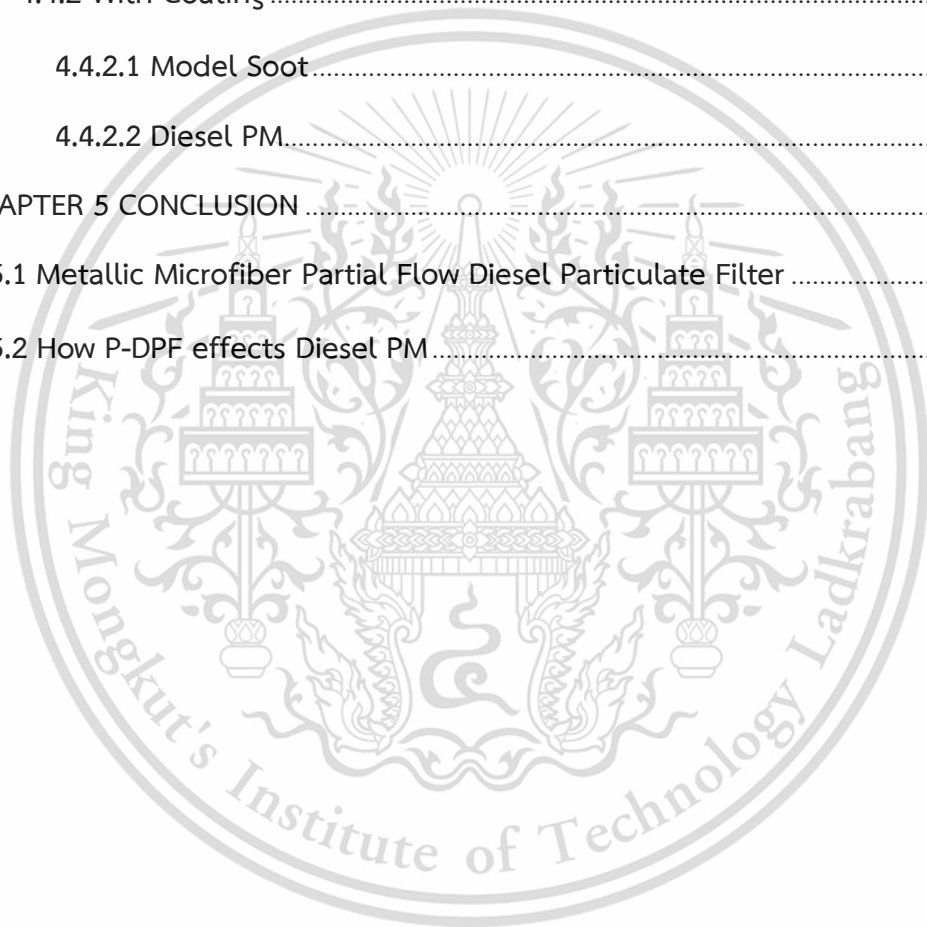
Chapters	Page
ABSTRACT	I
ACKNOWLEDGEMENT	II
TABLE OF CONTENTS	III
LIST OF TABLES	VI
LIST OF FIGURES	VII
CHAPTER 1 INTRODUCTION	1
1.1 Research background	1
1.2 Objectives	2
1.3 Scope	2
CHAPTER 2 LITERATURE REVIEW	4
2.1 Particulate Matter Formation	4
2.2 Particulate Matter Nanostructure and Oxidation	6
2.2.1 Elemental Composition and Nanostructure	6
2.2.2 Oxidation	9
2.2.3 Nanostructure and Oxidation	11
2.3 Exhaust after-treatment	14
2.3.1 Diesel Oxidation Catalyst	14
2.3.2 Full-flow Diesel Particulate Filter	16
2.3.3 Partial-flow Diesel Particulate Filter	16
2.3.4 Catalyst Coating	17
CHAPTER 3 METHODOLOGY	20
3.1 Experimental Equipment and Procedure	20
3.1.1 Engine and DPF	20

This material is reserved for educational use only, not allowed for commercial use.

Forbidden to modify the content, and ^{III} cite the document when use.

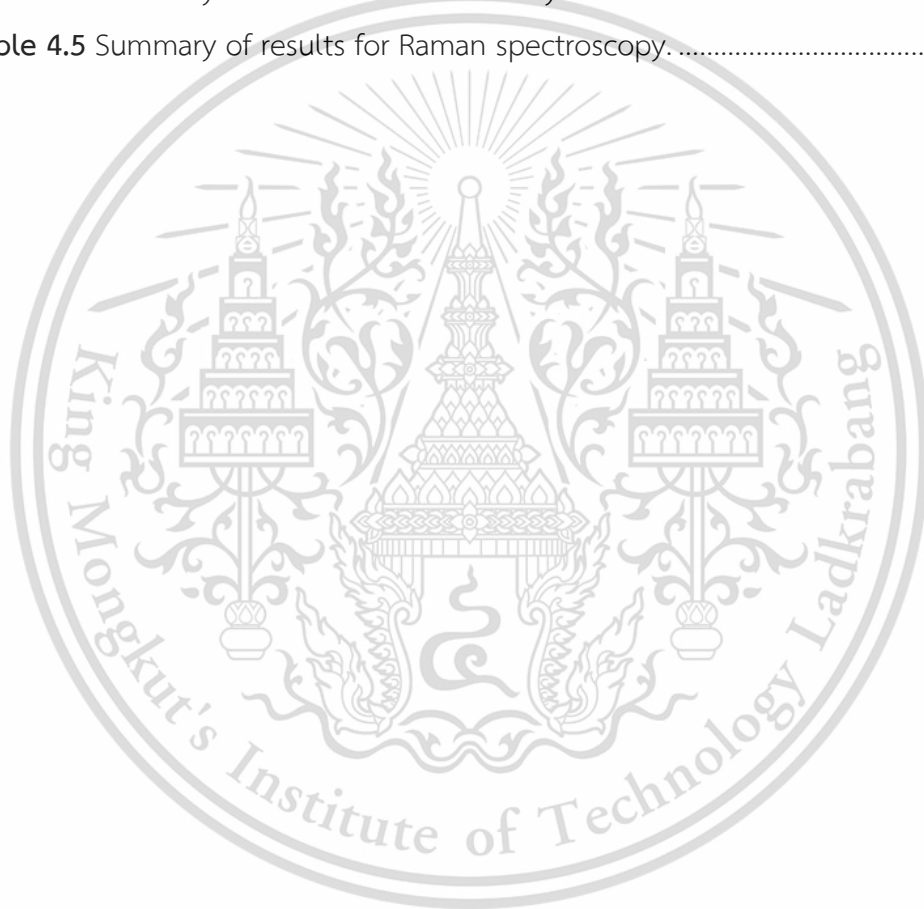
3.1.2 Soot Collection	22
3.1.3 Catalyst Coating.....	24
3.2 Analytical Equipment and Procedures	26
3.2.1 DLS.....	26
3.2.2 SEM-EDS	26
3.2.3 TEM.....	27
3.2.4 XRD	29
3.2.5 Raman Spectroscopy	31
3.2.6 TGA.....	31
3.2.7 Exhaust Emissions.....	34
CHAPTER 4 RESULTS AND DISCUSSION	35
4.1 P-DPF Material and Trapping	35
4.1.1 P-DPF Material.....	35
4.1.2 P-DPF Coating.....	37
4.1.3 P-DPF Trapping Behavior	41
4.2 Soot Nanostructure and Composition	44
4.2.1 Elemental Composition	44
4.2.2 Morphology.....	46
4.2.3 Nanostructure	48
4.2.3.1 TEM.....	48
4.2.3.2 XRD.....	53
4.2.3.3 Raman Spectroscopy.....	54
4.2.3.4 Comparison of results.....	55
4.3 Exhaust Emissions.....	58
4.3.1 Opacity.....	58

4.3.2 Temperature	59
4.3.3 CO ₂	59
4.3.4 NO	60
4.3.5 O ₂	61
4.4 Soot Oxidation.....	62
4.4.1 No Coating.....	62
4.4.2 With Coating	63
4.4.2.1 Model Soot.....	63
4.4.2.2 Diesel PM.....	65
CHAPTER 5 CONCLUSION	68
5.1 Metallic Microfiber Partial Flow Diesel Particulate Filter	68
5.2 How P-DPF effects Diesel PM.....	69



LIST OF TABLES

Tables	Page
Table 3.1 Engine and Aftertreatment System Specifications	21
Table 4.1 Summary of elemental composition using EDS.	37
Table 4.2 Summary of elemental composition of PM from different locations in exhaust after-treatment system using EDS.	46
Table 4.4 Summary of TEM fringe analysis.	49
Table 4.4 Summary of all nanostructure analysis.	54
Table 4.5 Summary of results for Raman spectroscopy.	55



LIST OF FIGURES

Figures	Page
Figure 2.1 Formation Process of PM [12].....	4
Figure 2.2 Particulate Matter and its composition [12].....	5
Figure 2.3 Size distribution of PM in terms of mass and number [16]	6
Figure 2.4 TEM images of soot derived from (a) Benzene, (b) Ethanol, and (c) Acetylene. [21]	8
Figure 2.5 TEM image of agglomerate PM particles from (a) GDI, (b) DDI, (c) carbon black. [22].....	8
Figure 2.6 Raman spectra of activated charcoal showing both bands. [23].....	9
Figure 2.7 Schematic of main steps in the oxidation of soot by NO _x . [28].....	11
Figure 2.8 TEM of soot showing the flaking and fullerene formation. [29]	12
Figure 2.9 TEM images of soot showing partial oxidation leaving behind hollow shells. [18].....	13
Figure 2.10 Experimental Full-flow or Wall-flow DPF. [30].....	16
Figure 2.11 Schematic of Partial-flow DPF with exhaust flow. [37].....	17
Figure 2.12 XRD spectrum with phase profiles for Ceria coating. [40].....	19
Figure 3.1 Engine connected to dynamometer and exhaust after-treatment system.	20
Figure 3.2 (a) Working principle of (b) partial flow DPF made up of metal (c) foil and (d) fiber.....	21
Figure 3.3 Working principle of microfiber trapping PM.....	22
Figure 3.4 Schematic diagram of positions of PM collection.	22
Figure 3.5 Real locations of soot collection for (a) pre-DOC, (b) post-DOC, and (c) post-P-DPF.....	23
Figure 3.6 Method to trap PM on metal microfiber fleece.....	23

Figure 3.7 (a) Working principle of sputtering PVD and (b) real life chamber used. [39]	24
Figure 3.8 Plate used to hold substrate (a) before and (b) during the sputtering process.	25
Figure 3.9 Equipment used for the dynamic light scattering nano particle analyzer.	26
Figure 3.10 Schottky field emission scanning electron microscopes used in this research.	27
Figure 3.11 Transmission electron microscope used in this research.	28
Figure 3.12 Example of measuring primary particle size.	28
Figure 3.13 Image processing steps of (a) selection, (b) cropping, (c) polarizing, (d) skeletonizing.	29
Figure 3.14 Example of measuring interlayer spacing showing (a) measurement locations and (b) sample plot.	29
Figure 3.15 XRD equipment used in this research.	30
Figure 3.16 Raman Spectroscopy equipment used in this research.	31
Figure 3.17 TGA equipment used in this research.	33
Figure 3.18 AVL equipment consisting of (left) gas analyzer and (right) opacimeter.	34
Figure 4.1 SEM of metal fibers in 300 magnification in (a) top view and (b) side view.	36
Figure 4.2 EDS spectra of (a) metal fiber and (b) metal flow guide.	36
Figure 4.3 SEM of metal fiber in 3000 magnification showing surface microstructure.	37
Figure 4.4 XRD spectra of Cerium Oxide coating using various power sources with profiles of two Cerium Oxide variants.	38
Figure 4.5 SEM showing (a) coating thickness, (b) coated metal fibers, and (c) coated surface of a metal fiber using 150W and 20min.	38
Figure 4.6 SEM showing (a) coating thickness, (b) coated metal fibers, and (c) coated surface of a metal fiber using 100W and 60min.	39

This material is reserved for educational use only, not allowed for commercial use.

Figure 4.7 SEM showing (a) coating thickness, (b) coated metal fibers, (c) coated surface of a metal fiber, and (d) shorn surface of coated metal fiber using 150W and 60min.	39
Figure 4.8 PM trapping on the metal fibers after 1s with (a) 10k magnification and (b) 1k magnification.....	41
Figure 4.9 PM trapping on the metal fibers after 30s with (a) 10k magnification, (b) 1k magnification, and (c) 300 magnification.....	42
Figure 4.10 PM trapping on the metal fibers using manual loading with (a) 10k magnification, (b) 1k magnification, and (c) 300 magnification.	43
Figure 4.11 EDS spectra of PM from (a) pre-DOC, (b) post-DOC, and (c) post-P-DPF..	45
Figure 4.12 TEM images of PM Agglomerates from (a) Pre-DOC, (b) Post-DOC, and (c) Post-P-DPF.	47
Figure 4.13 Particle size distribution from (a) scattering light method and (b) ImageJ with TEM analysis.....	48
Figure 4.14 TEM images showing nanostructure of PM from (a) Pre-DOC, (b) Post-DOC, and (c) Post-P-DPF.....	50
Figure 4.15 Black and white, 20x20nm images showing PM graphitic nanostructure from (a) Pre-DOC, (b) Post-DOC, and (c) Post-P-DPF.....	51
Figure 4.16 Process of analyzing TEM images for (a) Pre-DOC, (b) Post-DOC, and (c) Post-P-DPF.....	52
Figure 4.17 Fringe length distribution of PM along the exhaust after-treatment system.	52
Figure 4.18 XRD spectra of PM along the exhaust after-treatment system.	53
Figure 4.19 Raman spectra of PM along the exhaust after-treatment system.	54
Figure 4.20 Simultaneous Trapping and Oxidation on Metallic Partial Flow DPF.....	58
Figure 4.21 Opacity results along the exhaust after-treatment system.....	59
Figure 4.22 Temperature along the exhaust after-treatment system.	59
Figure 4.23 CO ₂ measurements along the exhaust after-treatment system.....	60

Figure 4.24 NO measurements along the exhaust after-treatment system..... 61

Figure 4.25 O₂ measurements along the exhaust after-treatment system. 61

Figure 4.26 (a) Mass conversion and (b) Arrhenius plot of soot on noncoated fleece.
 63

Figure 4.27 (a) Mass conversion and (b) Arrhenius plot of model soot on coated and
 noncoated metal fleece..... 64

Figure 4.28 (a) Isothermal mass conversion, (b) Arrhenius plot, and (c) non-isothermal
 mass conversion of diesel soot on coated and non-coated metal fleece.
 67



Chapter 1

INTRODUCTION

1.1. Research background

Due to the worsening global climate crisis, the adoption of electric vehicles have risen sharply in recent history and this trend will continue [1] [2] [3]. However, for the global south or for the developing parts of the world, the use of internal combustion engines is common and may stay relevant for the foreseeable future until financial factors of electrical vehicles can be reduced [4] [5] [6]. In the meantime, diesel combustion ignitions, or compression ignition engines, are widely used, especially for heavy-duty requirements. The diesel engine is also considered one of the more efficient internal combustion engines in regard to fuel economy and thermal efficiency. This is why in Thailand, light-duty diesel trucks make up a third of the total private automotive market share in terms of vehicle registration [7]. It is also why diesel fuel consumption is twice of that of gasoline consumption and half of total petroleum consumption. But this comes with the main drawback of diesel engines: particulate matter (PM). Vehicles are responsible for more than 40% of the total PM_{2.5} emissions in Bangkok, Thailand [8]. This is of high concern because diesel PM is widely known to be hazardous and detrimental to the health of the general public and to the environment [9] [10].

To counter this widespread problem of PM in the air and lungs in Thailand, the government has taken steps to limit the amount of PM that can be emitted from a given vehicle using classic and modern methods. The older classic regulations are tested by opacity or by light intensity, which is done by comparing the light intensity before and as black PM smoke passes through the sensor. For the newer modern regulations, an example is the European emission standard: EURO 6. This standard includes limits for particulate mass emission to 0.0045 g/km and 6×10^{11} particles/km for particulate number [11]. These emissions are measured by state-of-the-art sensors and equipment paired with a consistent driving standard, simulating both highway and city driving. The modern standards apply to new vehicles, and such would be in the responsibility of the automobile manufacturers. The classic standards apply to older

vehicles and would be in the responsibility of the vehicle owners during their registration tax renewal process. As the regulations tighten and the limit of allowable emitted PM decreases, there will be more and more need of particulate filters, such as diesel particulate filters (DPF).

1.2. Objectives

The objectives of this research were as follows:

- 1.2.1. To analyze the metallic microfiber P-DPF fiber layer in terms of microstructure, chemical composition, soot trapping, coating, and oxidation of the soot on the fiber layer.
- 1.2.2. To analyze diesel soot in terms of morphology (primary particle size and agglomerate size), nanostructure, and chemical composition with respect to exhaust after-treatment system.

1.3. Scope

This research was divided into 2 parts: the fiber layer from a metallic microfiber partial-flow DPF and how particulate matters (PM) is affected by it.

To understand the complex reactions and mechanisms that occur in the metallic microfiber P-DPF, the most important segment of the P-DPF was chosen for investigation: the metallic, fibrous filter layer, since all the trapping and oxidation, the main purpose of the DPF, would occur on this level. The microstructure of this fiber layer and its coating was observed and analyzed using scanning electron microscopy (SEM). The trapping of soot on the P-DPF was also investigated using SEM. The chemical and elemental composition of both the P-DPF and the subsequent coating were then analyzed with energy dispersive X-ray spectroscopy (EDS) and X-ray diffraction (XRD). Finally, soot was oxidized on the fiber layer to closely simulate the real oxidation that occurs in the exhaust after-treatment system.

To further investigate the after-treatment system, the level of focus was shifted to the effect of whole after-treatment system, consisting of the metallic microfiber P-DPF and a DOC, instead of just the fiber layer. This was done to adequately compare findings from the vital fiber layer to the effect of whole system on the PM. And so, to understand how the after-treatment system affects PM in the different stages, first the

This material is reserved for educational use only, not allowed for commercial use.

chemical composition was analyzed using EDS. Then the morphology was analyzed using dynamic light scattering (DLS) particle size analyzer and transmission electron microscopy (TEM) for the agglomerate size and primary particle size, respectively. The carbon nanostructure of the carbon chains that make up the primary particles were also analyzed using TEM in terms of fringes. This was then compared with two other nanostructure analysis methods: XRD and Raman Spectroscopy (RS).



This material is reserved for educational use only, not allowed for commercial use.

Forbidden to modify the content, and ³ cite the document when use.

Chapter 2

LITERATURE REVIEW

2.1 Particulate Matter Formation

In order to understand PM and its reduction, the formation must be analyzed as this is logically related to its structure. Engine borne PM are formed from the following steps: pyrolysis, nucleation, surface growth, coagulation, and aggregation [12]. This process is illustrated by **Figure 2.1**. Pyrolysis refers to the fuel breaking down into precursors of polycyclic aromatic hydrocarbons due to incomplete combustion [13]. This incomplete combustion is from a lack of oxygen during combustion which can be from a slow combustion compared to the timing of the engine cycle, or it could be from a local insufficiency of oxygen. In direct injection, the latter is most relevant as the combustion starts very locally where the sufficient mixing of fuel and oxygen is difficult. The broken-down fuel remnants then form into nuclei after intercepting other small hydrocarbons [12]. More and more broken-down components continue to deposit on the nuclei, forming primary particles, spherical in shape because of the nature of the surface growth. The latter stages of this surface growth are due to larger and larger carbon chains, which have had more time to form into more highly ordered crystallites compared to the less ordered carbon chains already intercepted by the nuclei. The carbon crystallites mentioned here are structured as multilayered hexagonal graphite sheets [14]. These crystallites can vary in curvature and size. These primary particles then lump together and aggregate with other single primary particles and other aggregates to form agglomerate particles. The composition of these agglomerates can be seen in **Figure 2.2**. It can be seen that there are also contents or portions in the agglomerate other than the carbon.

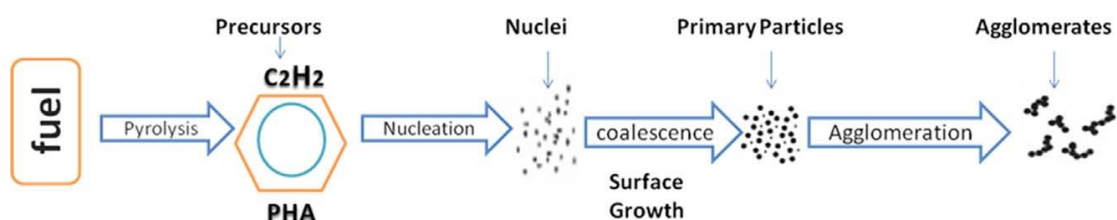


Figure 2.1 Formation Process of PM [12]

This material is reserved for educational use only, not allowed for commercial use.

Forbidden to modify the content, and cite the document when use.

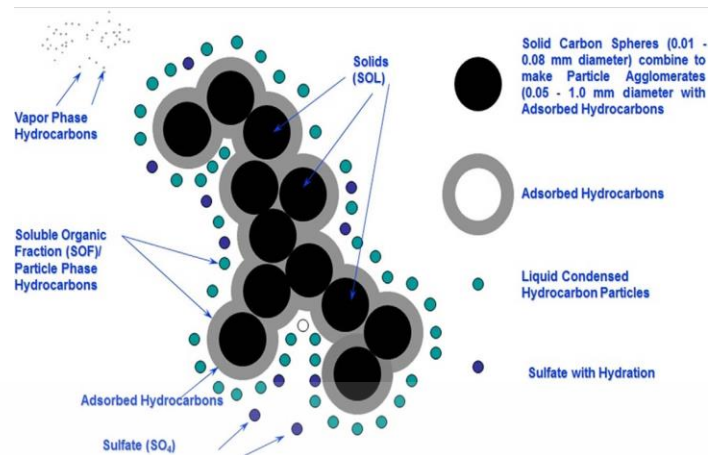


Figure 2.2 Particulate Matter and its composition [12]

With respect to the composition of the PM, engine PM usually fall into two main categories: the volatile or soluble fraction and the involatile or insoluble fraction. The soluble fraction includes the sulfate, nitrate, and organic fractions. The sulfate fraction contains sulfate ions and sulfuric acid. The nitrate fraction contains nitrate ions and nitric acid. The organic fraction contains thousands of different alkenes, alcohols, esters, acids, aromatics, and more. This soluble fraction tends to become absorbed by the PM agglomerate surface or cover the insoluble solid fraction in the particles that are seen as seen in **Figure 2.2**. The insoluble fraction includes the carbonaceous and ash fractions. The carbonaceous fraction is made up of solid phase carbon in an amorphous or graphitic structure. The ash fraction contains the remaining inorganic incombustible ash, which is mostly metal and its oxides [15].

The insoluble carbonaceous fraction in the PM is the most significant fraction in the entire PM as it can make up more than 90% of the total PM and is the fraction that is oxidized when a filter is undergoing regeneration [15]. However, another important aspect of PM is the size categorization because of the relation between the size of a harmful particle and how differently it can impact human health [9]. Engine PM can be divided into three size categories according to what mode of this formation process the particle is in: nucleation mode, accumulation mode, and coarse mode as seen in **Figure 2.3**. The first and second modes correspond to previously mentioned steps in the soot formation process with accumulation being a synonym for aggregation. The third mode, coarse mode, refers to the clumping of PM into even larger PM dust. The nucleation mode corresponds to the ~20nm size of individual primary particles. The aggregates formed from these primary particles make up the accumulation mode in

This material is reserved for educational use only, not allowed for commercial use.

the ~300 nm size. The aforementioned clumping of aggregates finally makes up the coarse mode in the ~5 μ m size range.

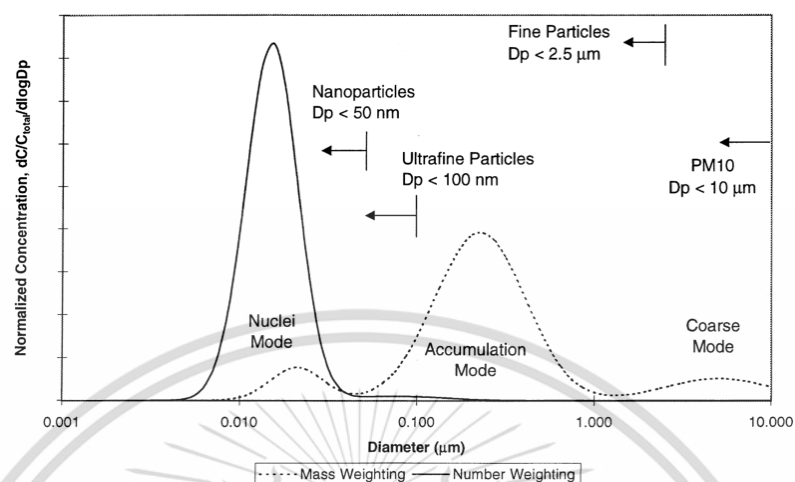


Figure 2.3 Size distribution of PM in terms of mass and number [16]

The previously mentioned two important aspects of the size categorization and carbon structure are the subject of most research related to PM as it can give information and important relationships about the soot reactivity and behavior to different treatment methods. There are numerous methods to analyze the soot nanostructure, morphology, composition, and reactivity which will be reviewed next.

2.2 Particulate Matter Nanostructure and Oxidation

2.2.1 Elemental Composition and Nanostructure

For the elemental composition of soot, there are various factors that can impact the elements that are found and how much of these elements are found in a given sample of PM. From the previous section, it is known that the soot has a soluble and insoluble fraction. The soluble fraction can clearly be seen in PM from various light duty diesel vehicle (LDDV) sample sets and heavy-duty diesel vehicle (HDDV) sample sets with more than 0.1% each of NO₃, Si, Al, SO₄, Ca, Na, Cl, and NH₄ [17].

For the insoluble carbonaceous fraction, soot analysis must be done with various methods including transmission electron microscopy (TEM), X-ray diffraction spectroscopy (XRD), and Raman spectroscopy (RS). TEM images can show the carbon

This material is reserved for educational use only, not allowed for commercial use.

nanostructure through fringes that represent the carbon graphitic crystallites [18] [14]. These fringes can be analyzed for length, interlayer spacing, and curvature. These parameters can then be compared with the analysis of RS and XRD which can give information about the amorphous and graphitic structure of the carbon in the PM [19].

Vazquez Santos et al 2011 [19] compared these different methods on carbon fibers to better relate and understand the different methods as the method and what they analyze are different. The TEM images in this particular research was not used to quantitatively analyze the nanostructure but rather to observe it. The XRD and RS were used quantitatively and in detail. The XRD analysis is divided into two important bands: a graphitic or highly ordered band and turbostratic or less ordered band. The graphitic band is represented by the 002 phase peak which is due to the stacking of the graphene layers that make up the crystallites which make up the PM particles [19]. As the order of the graphene layers increases, the peak will become narrower and shift right towards larger angles [19]. The turbostratic band is represented by the 10(X) band which becomes narrower and increases in intensity as the composition of the carbon is less graphitic and more disordered [19]. The XRD also allows calculations of the interlayer spacing and crystallite size. The RS method will be discussed later using earlier research which this paper also cites frequently.

Pahalagedara et al 2012 [20] investigated various carbon black and diesel soot for methods to characterize the carbonaceous soot. They proposed a model of considering soot particles saying that the primary particles are composed of the inner core, made up of fine particles and several distorted carbon layers, and the outer shell, made up of micro crystallites with structures of planar graphene.

Vander Wal et al 2005 [21] investigated the relation between the carbon nanostructure of soot and its oxidation. Soot from ethanol, benzene, and acetylene were used here. The soot from each source were observed with TEM and these images show the fringes that make up the soot as seen in **Figure 2.4**. Benzene soot consisted of short amorphous fringes which meant there was a higher relative quantity of edge sites. The acetylene soot consisted of longer fringes which meant there was a lower relative quantity of edge sites. Ethanol soot consisted of long but curved fringes which could allow oxidation sites. For the oxidation, the more graphitic acetylene soot took more time to oxidize fully. As such, as the fringe length decreases, there would be more edge sites which would allow faster oxidation and vice versa. The curved fringes

This material is reserved for educational use only, not allowed for commercial use.

also show a similar trend with more curvature or tortuosity being linked with faster oxidation.

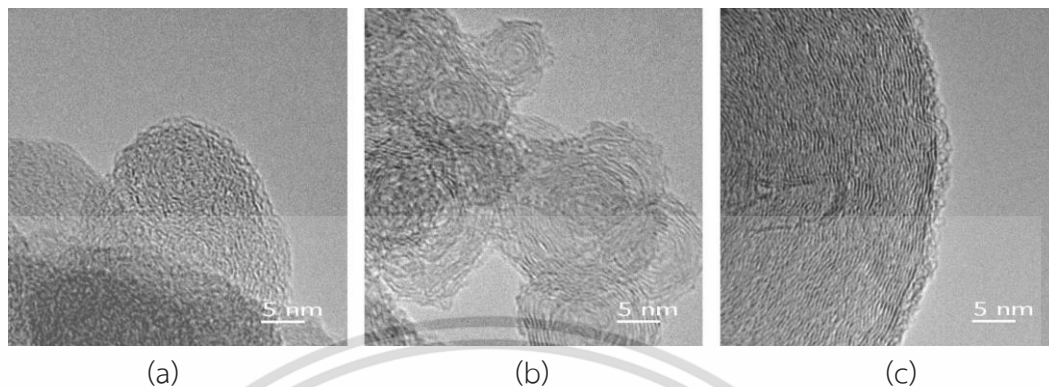


Figure 2.4 TEM images of soot derived from (a) Benzene, (b) Ethanol, and (c) Acetylene. [21]

Hay Mon Oo et al 2021 [22] analyzed the PM emitted from a gasoline direct injection (GDI) engine and diesel direct injection (DDI) engine to compare with model soot (carbon black). The soot elemental composition was analyzed using EDS, the morphology with TEM, the nanostructure with TEM and XRD, and the oxidation kinetics with TGA, which will be discussed later. The EDS revealed that the PM from all three sources were made up of carbon and oxygen with no soluble fraction detected. The morphology of the primary particles, seen in **Figure 2.5**, revealed that the carbon black primary particles were the largest at an average of 31 nm, followed by PM from DDI and GDI with 26 nm and 24 nm, respectively [22]. The fringe analysis showed that the carbon black was most graphitic with lower inter-planar spacing and longer fringes [22]. The least graphitic or most amorphous was GDI PM which was confirmed with the XRD analysis [22].

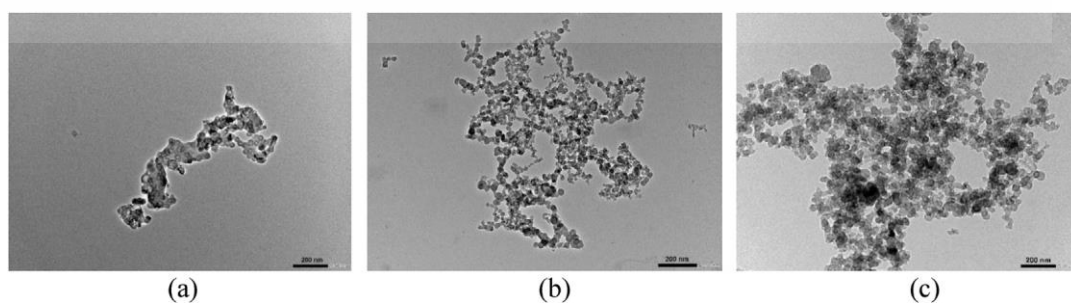


Figure 2.5 TEM image of agglomerate PM particles from (a) GDI, (b) DDI, (c) carbon black. [22]

This material is reserved for educational use only, not allowed for commercial use.

Forbidden to modify the content, and cite the document when use.

Tuinstra and Koenig 1970 [23] reported two bands in Raman spectra when analyzing graphite and other graphitic material as seen in **Figure 2.6**. The intensities of these bands were inversely proportional to the crystallite size of the graphite and allowed an estimation of the crystallite size as well as analysis of the structural order of the carbon as an overall [23]. The first band, which would be called the G band or graphitic band, was at 1575 cm^{-1} which showed up in the single crystal graphite. The second band, which would be called the D band or disorder band, was at 1355 cm^{-1} which showed up in commercial graphite, activated charcoal and others. After further analysis of commercial graphite and activated charcoal, a double peak was found with the peak at 1575 cm^{-1} corresponding to the single crystal graphite order and the peak at 1355 cm^{-1} corresponding to the polycrystalline graphite or amorphous carbon [23]. The intensity ratios of these bands would then allow calculations of the crystallite size [19].

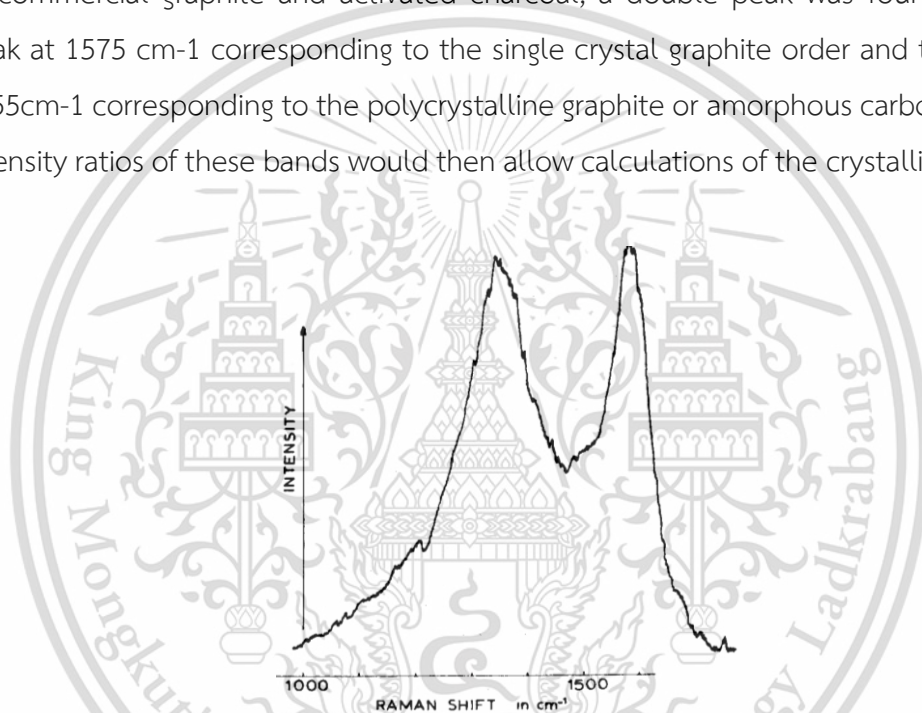


Figure 2.6 Raman spectra of activated charcoal showing both bands. [23]

Cuesta et al 1998 [24] compared results from analyzing carbonaceous materials using XRD and Raman spectroscopy. Various carbon materials were compared using these two methods. They showed that although the quantitative results were not the same, the trends from both methods complimented each other. XRD was considered more accurate for the crystallite length or L_a calculation [24].

2.2.2 Oxidation

This material is reserved for educational use only, not allowed for commercial use.

Forbidden to modify the content, and cite the document when use.

The oxidation of soot is of high interest because there are two main methods to clean a filter: to physically dislodge the trapped particles, by using fluids such as air or a water solution, and to burn the trapped particles, as is, inside the filter. The latter is commonly used in DPFs and studying the oxidation of the trapped soot allows the improvement of the filter design. The main design criteria, however, is to use the exhaust gas instead of intaking fresh atmospheric gas.

Raj et al 2012 [25] explored reaction mechanisms for surface oxidation by O_2 . 3 pathways were proposed in terms of soot molecular structure to go from the unoxidized soot to CO and CO_2 . It was observed that carbon oxidation by O_2 at low non flame temperatures (150-450°C) increased the weight of the soot because of the formation of oxides on the surface. This then led to the desorption of CO and CO_2 . It should be noted that carbon gasification involves the free barrierless addition of O_2 at radical sites of soot. This forms a higher energy barrier as some areas become more stable meaning more activation energy is required to oxidize the soot. It should be noted that although the energy released by the addition of O_2 should be enough to start reactions in other parts of the soot, soot oxidation does not start until higher temperatures of over 450°C.

Karin and Hanamura 2010 [26] explored the trapping and oxidation of PM on wall flow DPF with a SiC coating. This improves the filtration performance and reduces the activation energy for oxidizing the soot. More importantly, the SiC nanoparticles play a significant role in the oxygen mobility during soot oxidation. The oxidation here was done with 7% O_2 . The unstable oxides from the SiC coating nanoparticles may have caused higher oxygen mobility around the soot oxidation sites, enhancing the oxidation of the soot.

Matarrese et al 2017 [27] explored varying levels of O_2 , NO_2 , and H_2O and its effect on soot oxidation to simulate real exhaust conditions (250-350°C, 0-5v% O_2 , 0-500 ppm NO_2 , 0-5v% H_2O). It was found that NO_2 initiated the oxidation of soot at low temperatures where oxygen was unreactive. But during soot oxidation, NO_2 and O_2 worked together instead of inhibiting each other. When only NO_2 is used, NO_2 is thought to be absorbed onto the carbon surface in the form of nitrates ad-species when it is first introduced to soot. It also oxidizes the soot although this increases after the initial absorption of NO_2 . It was also found that a substantial contribution of molecular

This material is reserved for educational use only, not allowed for commercial use.

oxygen was supplied to the soot oxidation process instead of being absorbed. Faster oxidation was observed when both NO_2 and O_2 were used then with just NO_2 or just O_2 . The oxidation rate increased in the presence of H_2O possibly due to the formation of nitric and nitrous acid which enhanced oxidation by NO_2 and O_2 .

Leistner et al 2012 [28] investigated soot oxidation by NO_2 , NO , $\text{NO} + \text{O}_2$, the mechanisms of which are shown in **Figure 2.7**. The gas mixture determined whether N_2 or NO_2 and CO_2 were produced. When just NO is used, NO is absorbed by the surface and form “ C^*NO ” species. When NO_2 is used, NO is produced because the “ C^*NO_2 ” species is not stable. The reaction with NO_2 is controlled by the formation of the “ C^*ONO_2 ” complex when T is lower than 600°C . Higher temperatures show the reaction being more dependent on the temperature. The reaction with NO is limited by the NO absorption at all temperatures, explaining why it is less reactive compared to NO_2 . $\text{NO} + \text{O}_2$ enhanced the oxidation because of the increased number of C^*O species. C^*O is preferred and forms C^*ONO_2 then CO and/or CO_2 . C^*NO forms C^*O and C^*N which can form N_2 . But this N_2 formation does not occur when O_2 or NO_2 are present.

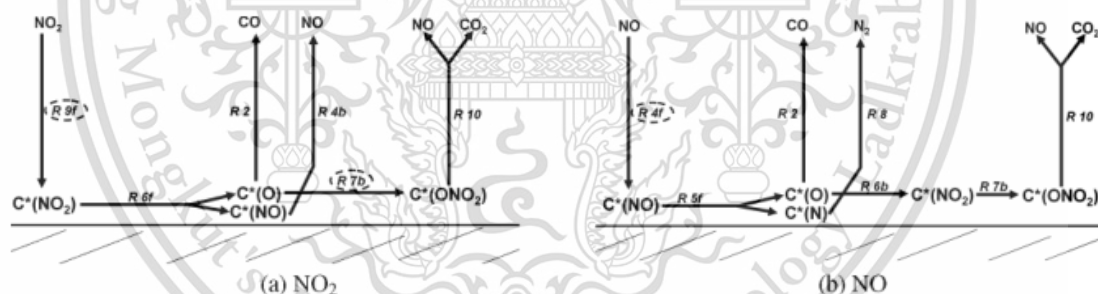


Figure 2.7 Schematic of main steps in the oxidation of soot by NO_x . [28]

2.2.3 Nanostructure and Oxidation

Pahalagedara et al 2012 [20] also investigated the relationship between the oxidation and the morphology by the gasification of soot using 10% O_2 . It was found that smaller particles have higher surface oxidation activity because their high surface area to volume ratio allows better contact with the oxidant. It is thought that the high surface area means there are more defects on the surface which corresponds to a less dense outer shell. As said previously, because the outer shell consists of numerous

smaller crystallites, if the surface area to volume ratio is higher, there are relatively more edge sites leading to higher oxidative activity. This means that surface oxidation is dependent on the surface condition of the particle such as the surface area to volume ratio and the actual surface area.

Toth et al 2019 [29] observed the two dominant oxidation models in real-time in situ experimentation. These are the shrinking core model and the internal burning model. The shrinking core model is characterized by the size of the primary particle decreasing with time as oxidation occurs on the surface and therefore reduces its overall size. Internal burning is characterized by the overall size not changing significantly but the mass decreasing more significantly due to oxidation that occurs inside the primary particle instead of on the surface. In the referenced research, surface oxidation was dominant. Three types of surface oxidation mechanisms were also observed: Flaking, Partial detachment of BSU (Basic structural units) stacks, and Fullerene formation. Flaking refers to single-layer graphene detaching from the primary particle in a peeling or flaking manner. Partial detachment of BSU stacks refer to similar phenomena as the flaking but with multiple graphene sheets at a time. Fullerene is spherical carbon nanostructure. This occurred because fullerene is favored over the partially gasified and etched graphene. These mechanisms can be seen in **Figure 2.8**. The shrinking core model can be considered for larger particles.

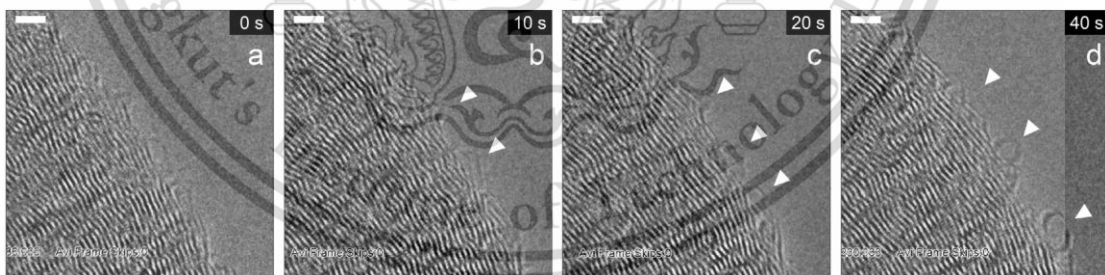


Figure 2.8 TEM of soot showing the flaking and fullerene formation. [29]

Toth et al 2019 [29] also observed internal burning in smaller particles. It was observed that oxidation occurred primarily at the core and formed loose graphene sheets attached to the inside of the outer shell. This was then oxidized and left behind a hollow shell. Toth also compared this to other literature where biodiesel soot more easily fell into this model. Oxygen is thought to diffuse into the core and burn since

the core is more reactive because it is generally more amorphous. This will be investigated more in the next reference literature.

Vander Wal et al 2007 [18] studied soot from diesel PM on DPFs. The PM from this study were partially oxidized and showed the internal burning phenomena. On top of this phenomenon, a densification of graphitization occurred in the remaining carbon. The internal burning phenomenon occurred due to a preferential oxidation of amorphous carbon. Among this amorphous carbon includes the edge sites and cross-links that may interfere or inhibit the graphitic carbon to reorient and realign. This realignment would happen in the low oxygen and relatively low temperature conditions commonly experienced in DPFs.

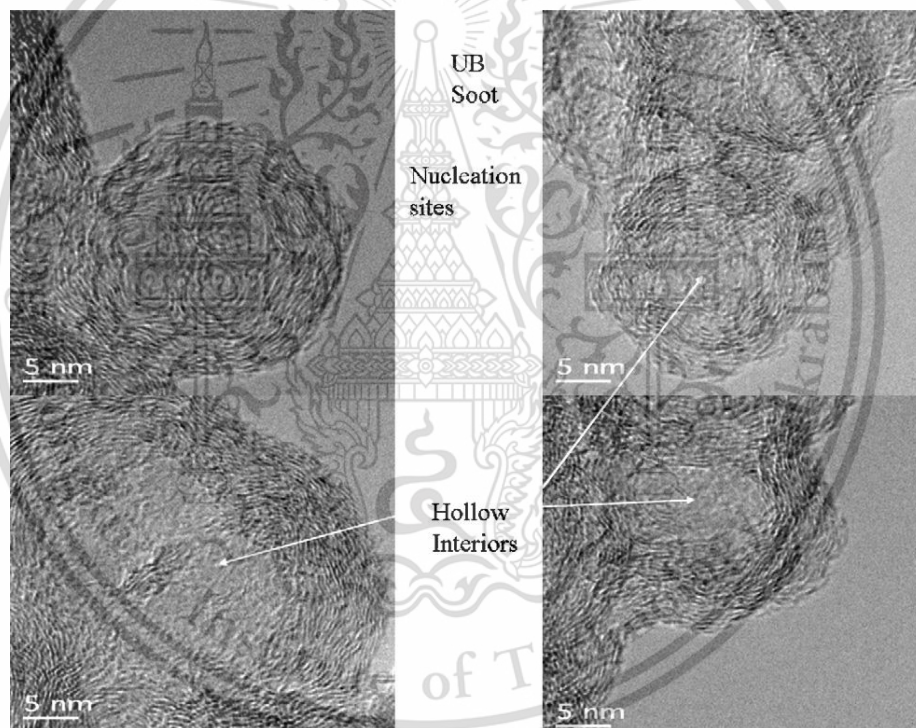


Figure 2.9 TEM images of soot showing partial oxidation leaving behind hollow shells. [18]

Srilomsak and Hanamura 2020 [30] recorded a time-lapse visualization of shrinking soot during active regeneration using 10% O₂. This study did not show internal burning meaning that the soot used in this study could have passivated outer shells that do not allow O₂ diffusion. This meant that the oxidation was dominated by surface oxidation. Shrinkage of the primary particle diameters was also observed. This could

This material is reserved for educational use only, not allowed for commercial use.

be caused by the surface oxidation or by a mixture of both the surface oxidation and internal burning. The non-intuitive phenomenon of separation between the soot cake and the DPF was also investigated. This separation is not intuitive because the gas flow was toward the DPF wall which should compress the soot cake toward the DPF. But the electrostatic forces between the soot and the DPF decrease as the soot aggregate decreases, due to the ongoing oxidation. This may be a cause for separation to occur.

2.3 Exhaust after-treatment

2.3.1 Diesel Oxidation Catalyst

As said in the introduction, the newer and stricter exhaust emission regulations mean that internal combustion engines must be paired with an exhaust after-treatment system. In diesel applications, this is usually done with a diesel oxidation catalyst (DOC) to catalyze the reduction and oxidation of harmful emissions by using special material catalysts. As such, Fino et al 2016 [31] reviewed soot oxidation in catalyst coated surfaces. Soot oxidation catalysts depend on structural parameters and the reaction mechanisms. Concerning redox processes, when Ceria and Pt are used together, ceria's ability to absorb and diffuse molecular oxygen to the Pt sites was reported. Ceria also stores NO_2 at temperatures below 400°C and assists in oxidation. Ceria is therefore popular as a support for other catalysts. Although noble metals are dominant in catalysts because of their stability and performance, ceria is an increasing popular catalyst option.

Neha et al 2020 [32] reviewed soot formation, catalyst types, and soot oxidation via ceria-based catalysts. It was reported that loose contact or simple manual loading of the soot with the catalyst powder did not result in effective catalytic performances due to low contact frequency. Under these conditions, catalytic activity is governed by the mobility of the oxidizing intermediates. This review paper also discussed metallic monolith catalysts which utilizes the higher open frontal area and low resistance. A disadvantage of these monoliths is, however, the low specific surface area but this could be assisted with alumina coating as mentioned previously.

Liu et al 2015 [33] reviewed developments in ceria-based catalysts and soot oxidation mechanisms over the various catalysts. As said previously, ceria is a popular

base and works well with other catalysts due to its ability to absorb and transfer oxygen. There have been developments for various special morphologies of ceria-based catalysts for higher surface area and mobility like nanoscale fibers and exposed lattice planes of catalyst. For ceria-based catalytic mechanisms, it has been established that there are two mechanisms. They are the “active oxygen assisted mechanism” where ceria promotes the formation of highly reactive oxygen species which spillover to the soot surface and oxidizes soot efficiently, and the “NO₂ assisted mechanism” where ceria oxidizes NO into NO₂ this oxidizes the soot indirectly. The latter mechanism is applied more for loose contact and the former for tighter contact. Although CeO₂ is considered stable, the thermal stability is rather poor and is prone to thermal aging. Additives are therefore added to increase its durability. Ceria is also known to be prone to sulfur poisoning due to its alkaline nature. This could be remedied by adding sacrificial alkaline additives, acidic species, or noble metals.

Koop and Deutschmann 2012 [34] investigated the surface reaction mechanism for Pt catalyzed conversion of exhaust gases. This model used 73 elementary-step reactions among 22 surface and 11 gas-phase species. The conversions were done for CO, CH₄, C₃H₆, and NO_x. The catalyst here was a cordierite monolith with Pt alumina wash-coat. Similar to the literature of Chatterjee et al. [35], the oxidation of the hydrocarbon consists of two pathways. Adsorption of the hydrocarbon comes with the splitting of an H-atom. This is followed by the carbon atoms being oxidized to CO and CO₂. The other path splits off an H-atom and it reacts with an adsorbed oxygen atom to form a hydroxyl species. In lean conditions, NO is oxidized to NO₂ but at 350°C, equilibrium is found, and further oxidation is restricted. There are 2 possible reaction pathways for NO to NO₂: the Langmuir-Hinshelwood (LH) and Eley-Rideal (ER). ER says that NO from the gas phase simply reacts with an adsorbed oxygen atom. LH says that there are more steps between this. The forward reaction of NO to NO₂ is requires a high activation of 133 kJ/mol and is increasing limited with carbon monoxide. But the reverse reaction is less activated and acts as an effective source of surface oxygen on Pt even in an oxygen rich condition due to the decomposition of NO₂. In rich gas conditions, oxygen primarily reacts with CO and the hydrocarbons and does not allow NO oxidation. So NO reacts with hydrogen, hydrocarbons, and CO to reduce into nitrogen gas. However, the reduction via hydrogen is a direct surface since the adsorbed hydrogen lowers the activation energy to reduce. But this is strongly inhibited

This material is reserved for educational use only, not allowed for commercial use.

by the presence of CO. These mechanisms were confirmed by testing results of a diesel catalyst on a dynamic engine test bench.

2.3.2 Full-flow Diesel Particulate Filter

To further reduce emissions and trap PM, DPFs are used more and more commonly. They are categorized into full-flow, or wall-flow, and partial-flow [36]. Full-flow DPFs are usually ceramic and consists of a porous microstructure in a honeycomb macrostructure. The design is such that all the exhaust gas must flow through the walls of the filter, which is where the “full-flow” part of the name comes from. An example of this filter macrostructure can be seen in **Figure 2.10**. The PM deposits on the high internal surface area of the pores and this trapping occurs at efficiencies of around 90% [35]. As PM is being trapped on the filter, the exhaust flow is increasingly restricted and will increase the pressure in the exhaust pipe, causing back pressure. This leads to higher and higher amount of work being required to overcome this pressure to exhaust the post combustion gases. To reduce this pressure and restore the filter to trap more PM, the already trapped PM is oxidized by an external energy input like a burner [36]. To control this external energy input as well as the back pressure to know when the energy is needed, a control system is needed. Therefore, the regeneration of this filter is called an active regeneration because an active input is needed.



Figure 2.10 Experimental Full-flow or Wall-flow DPF. [30]

2.3.3 Partial-flow Diesel Particulate Filter

The partial-flow DPF (P-DPF) differs in this regard because it does not require an external energy input. As the name suggests, only a portion of the exhaust gas flows

through the filter. An example of this is a metallic P-DPF made up of layers of gas flow guides and microfiber fleece as seen in **Figure 2.11**. Because this type of DPF is designed to be used without a monitoring system or external energy input, the trapping of PM must not significantly affect the backpressure. To do achieve this, the trapping efficiency is lower than the full-flow DPF at approximately 50% [37]. However, due to the lack of control system and simplicity of its design, this filter has been popular as an important first step in reducing PM emissions, especially as a retrofit exhaust after-treatment system [37]. The P-DPF is usually used concurrently with a catalytic converter like a DOC to help treat emission gases as well as help with PM oxidation. It must be heavily noted that this after-treatment system utilizes continuous and simultaneous trapping and soot oxidation, unlike the full-flow DPF. This means that the soot cake layer phenomena that occurs in the full-flow DPF, when the flow of the exhaust forces and condenses the soot as all exhaust must pass through the filter, does not occur in the partial-flow DPF. Significant condensing of the soot is not possible as the filter is not fine enough. Because the filter is not fine enough, oxidation will also occur while soot is being trapped. This will be further explored in this research.



Figure 2.11 Schematic of Partial-flow DPF with exhaust flow. [37]

2.3.4 Catalyst Coating

To save cost and space in the undercarriage or engine bay, DPFs have been coated to combine the functions of a DOC and DPF. To understand this, coating methods need to be understood as well. Govender et al 2017 [38] reviewed the preparation of

monolith catalysts. Among the topics reviewed was the preparation of metallic monoliths. After an initial alumina coating to improve the coating bond, there are various methods of depositing the catalyst coating onto the monolith. A common method is wet impregnation. It is used in ceramics and metals alike. A solution containing the catalyst is prepared and drawn up by the monolith channels through capillary forces. Another method is deposition precipitation where the catalyst and a precipitating agent are in liquid phase and the monolith is dipped into the solution. It is then calcined, during which the precipitating agent decomposes.

Qing et al 2020 [39] reviewed techniques for catalyst coating catalytic membranes as well as advantages and disadvantages. They include, but are not limited to, dip coating, sol-gel, CVD, and PVD techniques. Dip coating involves submerging the support substrate into a solution containing the catalyst then drying. This allows complex inner geometries to be coated but there tends to be uneven coating due to the “wedge effect” where the coating is thicker towards the bottom. Sol-gel or solution-gelation technique consists of synthesizing solid materials from small molecules. This is done in four stages: Hydrolysis, Monomers condensing to form chains and ions, Growth of particles, and Aggregation of the polymer. This forms a very homogeneous coating and is very controllable, but it is also time consuming, costly, and is prone to delamination and cracking. CVD is a method where a catalyst precursor is vaporized in an inert atmosphere by heat light or plasma. The vapors then react on the solid surface to produce the coating. This method allows precise layering. PVD includes a wide variety of deposition methods, but they generally consist of evaporating the target material then transmitting the vapor to a surface for condensation under a vacuum, low-pressure, or plasma environment. PVD produces functional thin films that are resistant to abrasion, corrosion, and conductivity. As such, this may be an ideal method to coat the P-DPF as the coating would need to be thin enough to not affect the back pressure but maintain its catalytic performance.

To see if PVD can be used with ceria, the previously mentioned popular catalyst material, Chen and Wang 2020 [40] explored RF sputtering cerium oxide on glass and silicon substrates. The grain size and film thickness were also analyzed. RF or radio frequency sputtering has relatively low cost, good adhesion, and deposits onto the substrate at lower temperatures and the substrate does not need to be a conducting material. This study focused on controlling the key parameters like Ar/O₂ ratio, sputter

This material is reserved for educational use only, not allowed for commercial use.

voltage, and deposition time. A 4-inch Ce target was used. The first step was to decrease the pressure in the vacuum chamber to 10^{-6} Torr then let the Argon/O₂ mixture flow into the chamber. 100 and 120W were used with deposition times from 1 to 3 hrs and Ar/O₂ ratios of 1:2 and 2:1. It was seen that as deposition times increased, the film become smoother and thicker. The crystal size decreased as the deposition time increased. This was because the CeO₂ film formed layer by layer and the supersaturated vapor in the chamber became higher as time increased. This meant more nuclei formed and grew continuously which resulted in more crystals of smaller sizes. The crystal size also decreased with the increase of the Ar/O₂ ratio. It was also found that sputtering power significantly affected the film thickness due to the generation of higher supersaturated vapors under higher sputtering power. Deposition time had less of an effect on the conducting material (Si) then the nonconducting material (glass). The deposition time's effect on ceria coating was analyzed using XRD as seen in **Figure 2.12**. This figure also shows the phases seen in a ceria coating.

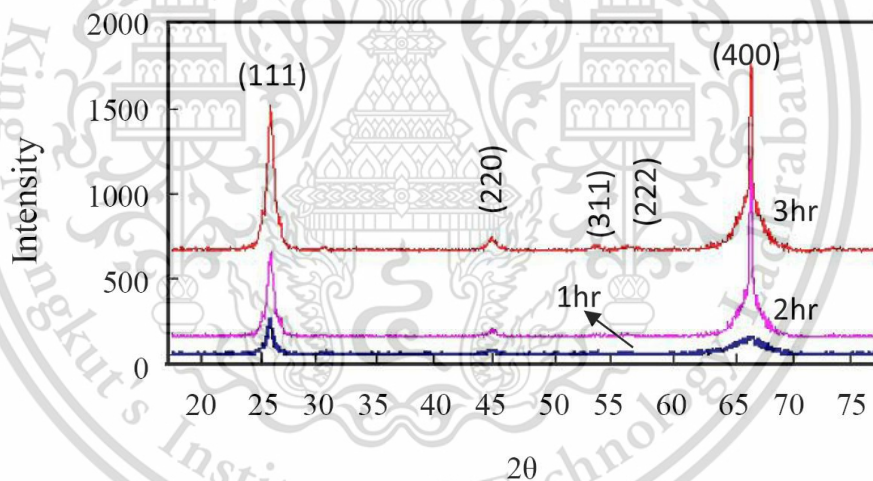


Figure 2.12 XRD spectrum with phase profiles for Ceria coating. [40]

Chapter 3

RESEARCH METHODOLOGY

3.1 Experimental Equipment and Procedure

3.1.1 Engine and DPF

This research utilized a four-cylinder, diesel direct injection engine with a displacement of 2.99 L. The engine was paired with an engine dynamometer, as seen in **Figure 3.1**, to test under various loads and speeds all while using commercial, standard diesel, which is B10 and is composed of 90% fossil fuel derived diesel and 10% biodiesel. B0 or 100% fossil fuel derived diesel is no longer available in Thailand to the public and such this is the most common, and therefore most relevant, fuel.



Figure 3.1 Engine connected to dynamometer and exhaust after-treatment system.

The DOC and DPF used in this research were not made in house and such have the specifications already defined. This is useful because the aim of this research was to investigate the simultaneous trapping and oxidation that occurs in a metallic microfiber inside the partial-flow DPF. The DOC and P-DPF specifications can be seen in Table 3.1. The specifics of the engine and exhaust after-treatment can be seen in Table 3.1.

This material is reserved for educational use only, not allowed for commercial use.

Forbidden to modify the content, and cite the document when use.

Table 3.1 Engine and Aftertreatment System Specifications

Engine Model	4JJ1-TC
Engine Type	4-Cylinder Compression Ignition
Injection System	Common Rail Direct Injection
Air Intake	Turbocharged
Displacement (cc)	2999
Bore and Stroke (mm)	95.4 × 104.9
Power	94.25 kW @ 3000 rpm
Torque	300 Nm @ 2000-3000 rpm
DOC Cell Density	300 CPSI
DOC Coating	Platinum-based Catalyst
P-DPF Cell Density	300 CPSI
P-DPF Overall Porosity	85%

The P-DPF used here was of a similar design as previous literature [37]. This P-DPF was made up of metal flow guide foil layers and metal microfiber fleece. The working principle of this design of P-DPF is seen in **Figure 3.2** as well as a cross-sectionally cut P-DPF showing the many layers that make up the P-DPF. The metal foil and fibers can also be seen in this figure. It can be seen from the working principle of the microfiber fleece in **Figure 3.3** that only a portion of the exhaust is directed towards the filter layer meaning the specific trapping efficiency is very low. However, due to the sheer number of layers and length of the filter, the overall trapping efficiency is at an acceptable level such that it has been used in real life applications.

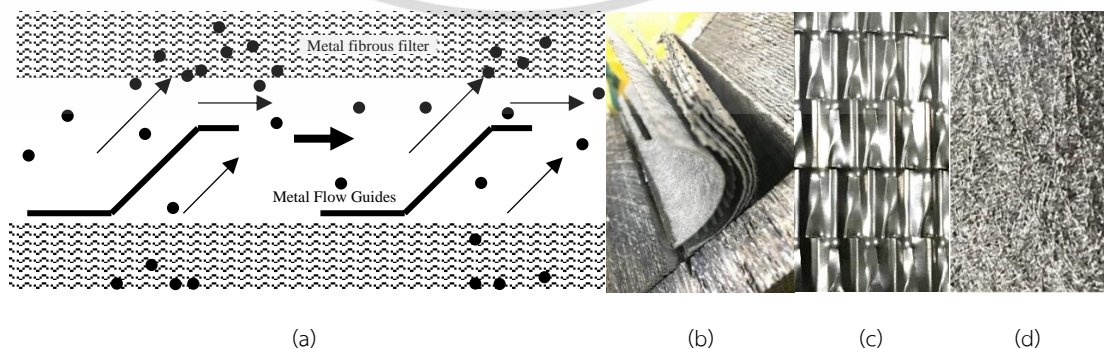


Figure 3.2 (a) Working principle of (b) metallic microfiber partial flow DPF made up of metal (c) foil and (d) fiber.

This material is reserved for educational use only, not allowed for commercial use.

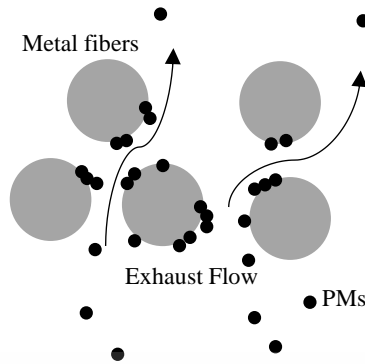


Figure 3.3 Working principle of microfiber trapping PM.

3.1.2 Soot Collection

To understand how the DOC and metallic microfiber P-DPF affected PM, three positions in the exhaust after-treatment system were chosen as shown in **Figure 3.4**. These positions were accessed by disassembling the after-exhaust system as seen in **Figure 3.5**. The disassembled portions would then reveal the inner walls covered with PM. These inner walls would then be scraped gently with a scalpel to physically remove the PM. The PM was then collected in an airtight container and stored at room temperature until it was examined with the various equipment used in this research.

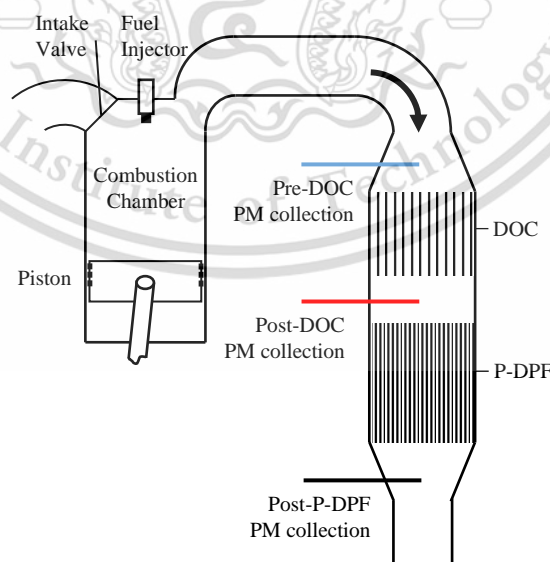


Figure 3.4 Schematic diagram of positions of PM collection.

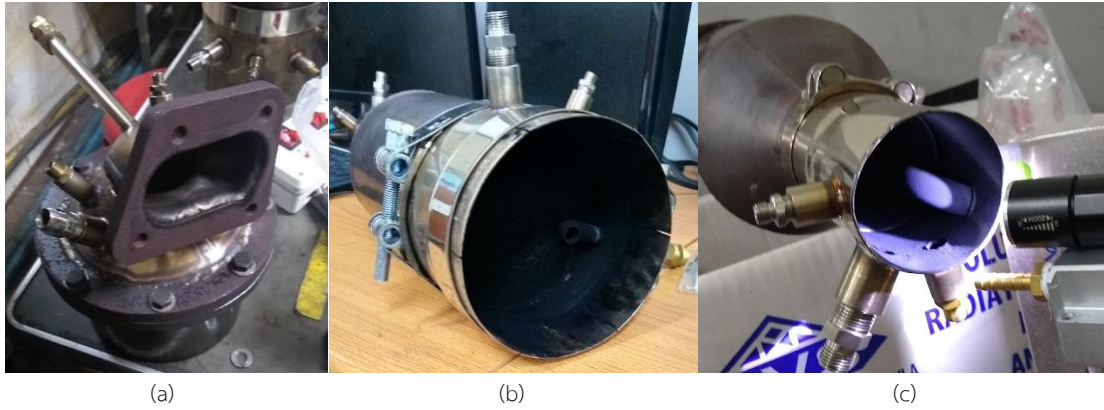


Figure 3.5 Real locations of soot collection for (a) pre-DOC, (b) post-DOC, and (c) post-P-DPF.

However, this was not the only method used in this research to collect soot. The second method was used to observe the trapping behavior of the PM on the metal microfibers. This was done by simulating real phenomena of exhaust going through the metal fibers in a similar manner which was seen in the working principle in **Figure 3.2**. As such, a piece of metal microfiber fleece was clamped by both ends and introduced to the raw exhaust, as seen in **Figure 3.6**, for 1 second then another piece was introduced for 30 seconds to see the evolution of the trapping behavior. These two conditions were deemed adequate for analyzing the trapping behavior as the nature of the metallic partial flow DPF would not allow a formation of a soot cake layer.

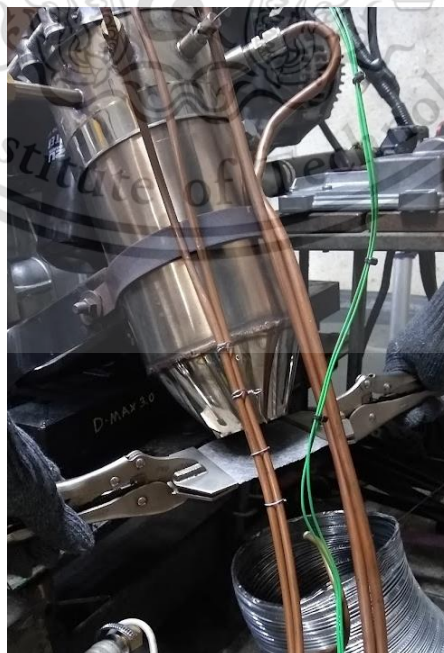


Figure 3.6 Method to trap PM on metal microfiber fleece.

This material is reserved for educational use only, not allowed for commercial use.

3.1.3 Catalyst Coating

To obtain a thin enough coating to minimize its effect on the trapping behavior, a PVD method, the working principle of which is seen in **Figure 3.7**, was used to coat CeO_2 onto the fibers. Ceria was used because it is a cost effective and popular catalyst material. The usage of this catalyst would also compliment the Pt based catalyst already used in this research, although this was outside of the scope of this research. Previous research proved that this thin coating method is possible on fibers smaller than the ones used here [41]. The target that would be used to coat the substrate was a CeO_2 ceramic target and radio frequency (RF) sputtering was used to deposit the thin layer of catalyst material using the chamber seen in **Figure 3.7**. Because the scope and aim of this research was to study the catalyst performance and not specifically the coating method, a Ce metallic target was not used. A CeO_2 ceramic target was used, although it was more fragile, because of the relative ease of the atmosphere balance. This is desired because to form CeO_2 with the metallic target, the O in the chamber must be in delicate control. Else, the formation of Ce_2O_3 may occur, which is not desired because of the O deficiency. Due to this, O was controlled even when using the ceramic CeO_2 target [42]. But for the sake of ease, this research will attempt to avoid controlling the O and confirm Ce_2O_3 does not form by XRD.

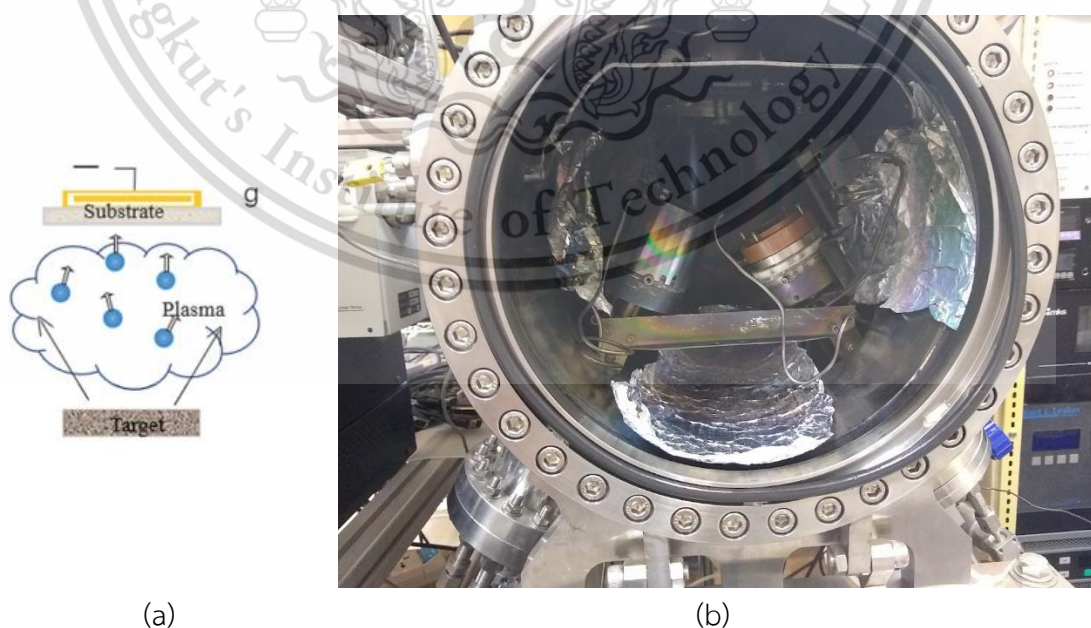


Figure 3.7 (a) Working principle of sputtering PVD and (b) real life chamber used. [39]

This material is reserved for educational use only, not allowed for commercial use.

Forbidden to modify the content, and cite the document when use.

For the coating process, pre-sputtering was first done to get rid of any contaminants on the target or metal fleece. The metal fleece, which will be called the substrate in this section, can be seen in its prepared form in **Figure 3.8a** with the substrate plate. 10W power and a substrate bias of -109 V was used for 20 minutes with the target shutter closed so that the substrate was not coated during this cleaning. The sputtering atmosphere was Ar at a base pressure of 70 mtorr and a deposition pressure of 6.3×10^{-2} mbar. The substrate was at room temperature with a voltage bias of -10V and was rotated in a speed of 1rpm. The substrate was not separately heated because previous literature showed that this was not necessary [42]. The bias was used to help the substrate attract the coating material and increase the deposition rate as well as improve the coating performance for this filter material. The rotation was to help the uniform deposition of the coating material. Initial powers of 100W, 125W, and 150W would be used on a Si wafer to ascertain the coating material in terms of CeO_2 or Ce_2O_3 using XRD. The coating thickness would also be analyzed with SEM to determine the power and a deposition time to do the final coating on the metal fibers. The thickness would then be confirmed with the Si wafer using SEM again.

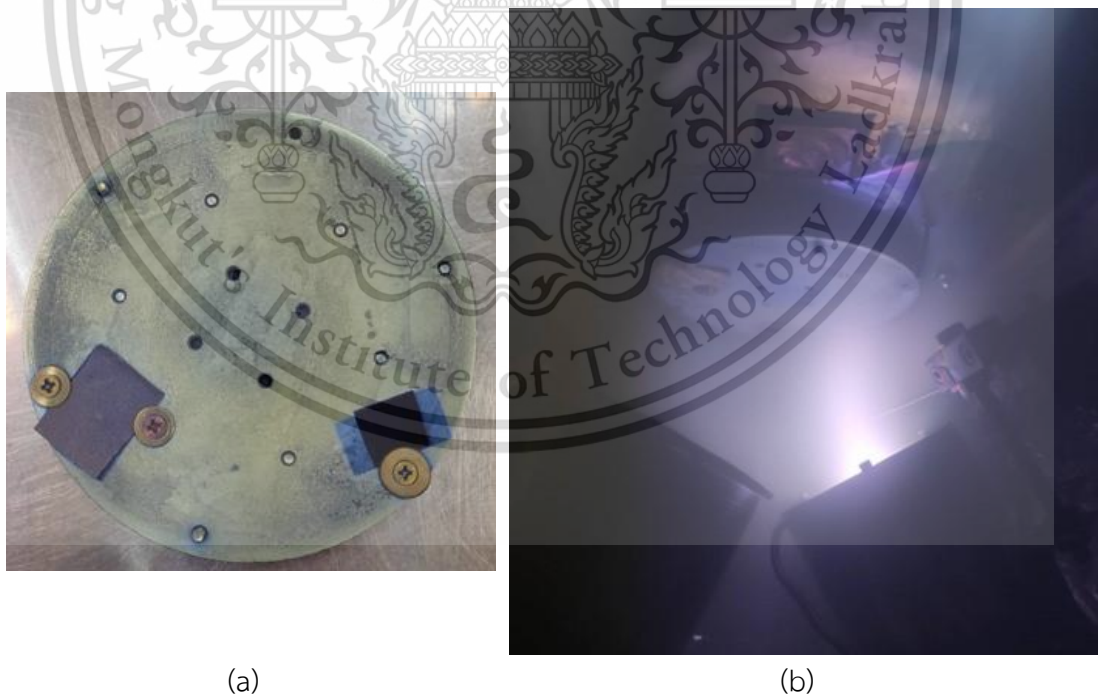


Figure 3.8 Plate used to hold substrate (a) before and (b) during the sputtering process.

3.2 Analytical Equipment and Procedures

3.2.1 DLS

To analyze the morphology of PM from the pre-DOC, post-DOC, and post-P-DPF positions, the PM powders were analyzed using a dynamic light scattering nano particle analyzer (Horiba SZ-100V2). 1 mg powder PM was suspended in 10 ml of anhydrous ethanol to set the conditions for the light scattering principle. This solution was then sonicated so the particles would be suspended instead of sinking. This vial was then inserted into the equipment. The output data of the equipment was the particles size and relative quantity of these particles in each size category. The equipment used here can be seen in **Figure 3.9** with a vial that contains a solution of suspended PM particles also being shown.

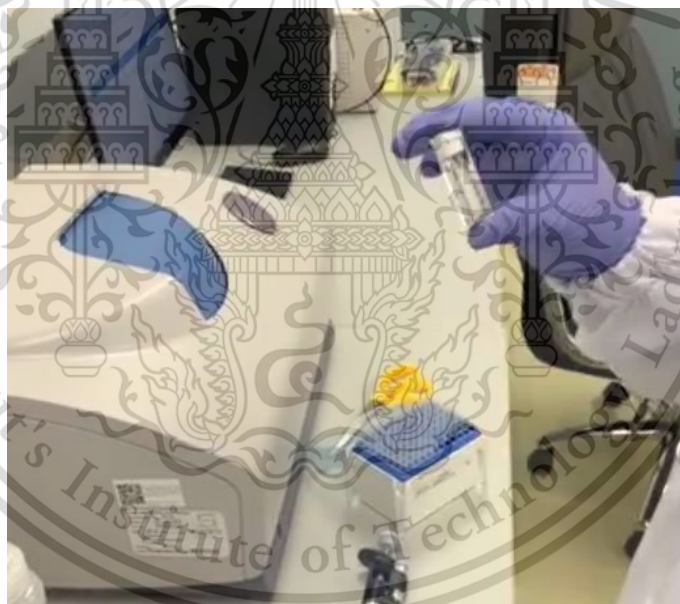


Figure 3.9 Equipment used for the dynamic light scattering nano particle analyzer.

3.2.2 SEM-EDS

SEM was used for various purposes in this research. These include the elemental composition using the EDS function in the SU5000, the microstructure of the metal fibers, the trapping behavior of soot on the metal fibers, the coating of the catalyst material on a Si wafer, and the coating on the metal fibers. Two separate equipment

This material is reserved for educational use only, not allowed for commercial use.

Forbidden to modify the content, and cite the document when use.

were used for the same purpose of magnifying the surface of a given point of interest. These were the SU5000 and JSM-7800F, seen in **Figure 3.10**, are both Schottky field emission scanning electron microscopes which allow high magnifications.



Figure 3.10 Schottky field emission scanning electron microscopes used in this research.

3.2.3 TEM

The morphology and nanostructure of the PM was analyzed using TEM (JEM-2100 Plus), seen in **Figure 3.9**, under magnifications of 100k and 800k, respectively. An image processing software (ImageJ) was used to do analyze the morphology and nanostructure quantitatively. The particle size analysis of the PM was done by measuring the sizes of individual ovular primary particles. This data would allow the plotting of the size distributions of the PM. An example of this can be seen in **Figure 3.12** with the pre-DOC position. The nanostructure was analyzed by converting the cross-sectional graphene sheets into single pixel wide fringes so that they could be analyzed quantitatively. The steps are shown in **Figure 3.13** and consist of cropping a 10nmx10nm square in the single primary particle. This square is then processed by converting it into grayscale, then polarizing into absolute black and white, then removing chaos lines that come up from the conversion process, then skeletonizing into single pixel wide lines. These lines are then analyzed automatically using a plugin to determine the fringe lengths. The average, maximum, and total fringe length as well as the number of counted fringes would be analyzed. The crystallite length, L_c , would be compared to the maximum fringe length here as done in literature [22].

This material is reserved for educational use only, not allowed for commercial use.

To analyze the space between these fringes, the intermediary image before removing the chaos lines were skeletonized. Then lines were drawn perpendicular to fringes. These lines were then used to make a profile plot of the intensity of the color for a given distance like **Figure 3.14**. The distance between the peaks would represent the distance between the fringes. This was done ten times and averaged for each 10x10nm square, and five squares were analyzed for each position. The interlayer spacing here would be compared to the interplanar spacing, d_{002} , for the crystallites in subsequent analysis methods.



Figure 3.11 Transmission electron microscope used in this research.

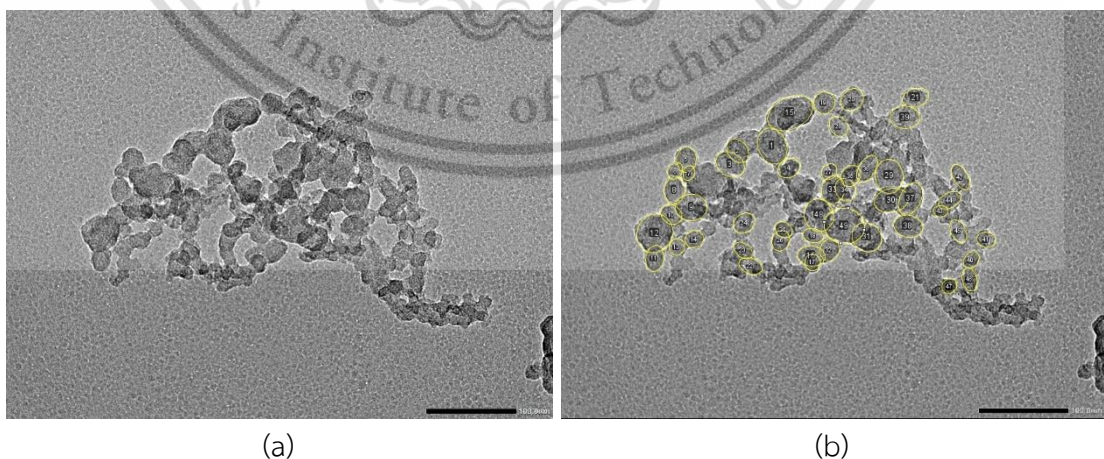


Figure 3.12 Example of measuring primary particle size.

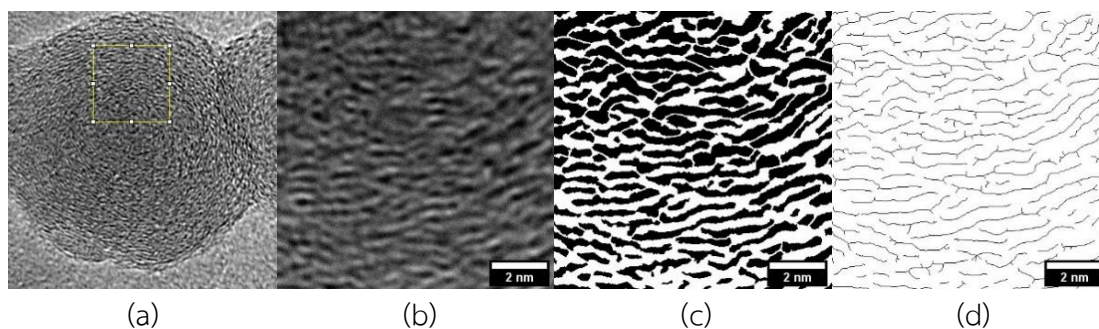


Figure 3.13 Image processing steps of (a) selection, (b) cropping, (c) polarizing, (d) skeletonizing.

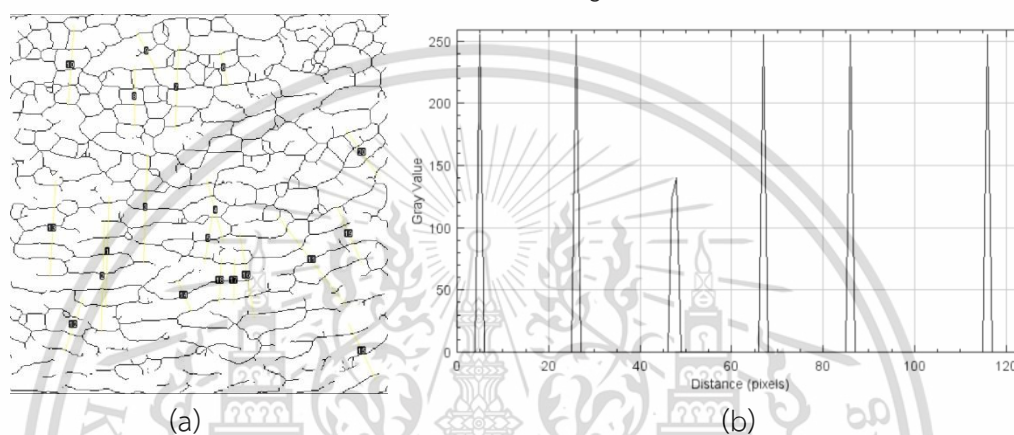


Figure 3.14 Example of measuring interlayer spacing showing (a) measurement locations and (b) sample plot.

3.2.4 XRD

XRD was done using an X-ray powder diffractometer (Bruker D8 Advance) with $\text{CuK}\alpha$ radiation source as seen in **Figure 3.15**. There were two separate tests done for two different purposes. The first analysis was done for the catalyst coating which could reveal information about the chemical structure of the catalyst coating. This is important as the previously mentioned desired material is CeO_2 and not Ce_2O_3 . For the sake of simplicity, the scanning angle range here was $20^\circ < 2\theta < 60^\circ$ as this was the range in which most of the phase profiles were in. The phase profiles were from publicly available databases. The other analysis was for the carbonaceous powder PM and done in the range of $10^\circ < 2\theta < 90^\circ$. The data from this analysis was processed using Bragg's law shown in (3.1) and Scherrer's formulae shown in (3.2), (3.3), and (3.4). These equations were used in literature and were for the 002 and 100 plane peaks.

$$d_{002} = \frac{\lambda}{2 \sin \theta_{002}} \quad (3.1)$$

$$L_C = \frac{0.89 \lambda}{\beta_{002} \cos \theta_{002}} \quad (3.2)$$

$$N = \frac{L_C}{d_{002}} \quad (3.3)$$

$$L_a = \frac{1.84 \lambda}{\beta_{100} \cos \theta_{100}} \quad (3.4)$$

where λ is the X-ray wavelength (0.15406 nm), β is the full-width-at-half-maximum of the respective planes, and θ is the angle at which the respective plane is centered at.

These equations allowed comparisons between the XRD and other nanostructure analysis by giving the crystallite width, height, interplanar spacing, and stacking number for L_C , L_a , d_{002} , and N , respectively. The d_{002} would allow direct comparisons to the results from the interlayer spacing measurements in the TEM. The N would show the stacking density to compare between the stages. It is important to note that XRD is a bulk diffraction analysis and is based on hkl planes in a crystallite form. For graphite materials, the plane peaks that are analyzed are the 002 peak and 100 peak. The 002 peak is related to the orientation or degree of graphitization of the carbonaceous aromatic layers while the 100 peak is related to the degree of condensation or size of said aromatic layers [43].



Figure 3.15 XRD equipment used in this research.

This material is reserved for educational use only, not allowed for commercial use.

3.2.5 Raman Spectroscopy

The final nanostructure analysis was done with RS (LabRAM HR Evolution), seen in **Figure 3.16**, which utilized a 532nm wavelength laser. The Raman shift range used here was 500 – 2000 cm^{-1} . The peaks from this analysis were processed to give the intensity ratio of the amorphous and graphitic carbon structure as well as a comparison of the crystallite width using the equation proposed by Knight and White [44] seen in (3.5).

$$L_a = \frac{4.4}{I_D/I_G} \quad (3.5)$$

where I_D and I_G represents the intensity of the D band and G band, respectively.

It should be noted that Raman spectroscopy is a more local, vibrational analysis. This results in two main peaks for crystallite carbon: the D-band and G-band which was discussed in the literature review. This analysis was used to get just the crystallite height, L_a which could be compared with the same parameter calculated from the XRD and the fringe length from TEM. There are systematic differences in the different analyses and methods seen in TEM, XRD, and RS, but they allow findings from each method to support a general conclusion [19].



Figure 3.16 Raman Spectroscopy equipment used in this research.

3.2.6 TGA

TGA (Netzsch TG209-F3), seen in **Figure 3.17**, was utilized to observe and analyze the oxidation of soot on the metal fibers. The oxidation would be compared between
This material is reserved for educational use only, not allowed for commercial use.

the bare untreated metal fleece and the catalyst coated fleece. PM was coated on the metal fleece in a manner that will be discussed later. This was then oxidized using the isothermal method with temperatures of 525°C for 120 minutes and 550, 575, and 600°C for 60 minutes. Each temperature and coated/noncoated condition was done with a fresh piece of metal fleece. The non-isothermal method was done with a temperature ramp of 10°C/min from room temperature to 630°C. The analyzed oxidation mechanism from the isothermal method was the activation energy of the soot oxidation. The chemical equation of the reaction that occurs here can be seen in (3.6) where the solid C reacts with gaseous O₂ to convert into CO₂ which would decrease the mass of the sample as the chemical product of CO₂ is gaseous and would flow out. This reaction is also represented by (3.7) and can be modeled in terms of chemical reaction kinetics.



$$-d[\text{C}]/dt = k[\text{C}]^n[\text{O}_2]^m \quad (3.7)$$

where C is the mass of the carbonaceous PM, t is time, k is the chemical reaction rate, and m and n are the reaction orders of PM and O₂, respectively.

The reaction order n is assumed to be 1 as a complete internal surface diffusion model where the rate of reaction would be proportional to the PM mass. This reaction can be expressed as the Arrhenius equation in (3.8).

$$k = A e^{-E_a/RT} \quad (3.8)$$

where A represents the frequency factor, E_a is the activation energy, R is the universal gas constant, and T is the temperature in Kelvin.

(3.7) and (3.8) can be combined to form (3.9) which represents the change of the PM mass as a percentage.

$$\frac{-d[\text{C}]/dt}{[\text{C}]} = A e^{-E_a/RT} [\text{O}_2]^m \quad (3.9)$$

This can be derived into an Arrhenius equation as seen in (3.10) where constant represents the constant in (3.11). This allows a simple linear calculation of the activation energy where the left hand side is the y-axis, the $-E_a/R$ represents the linear constant, and the $1/T$ represents the x-axis similar to a $y=mx+b$ form.

$$\ln\left(\frac{-d[C]/dt}{[C]}\right) = \left(-\frac{E_a}{R}\right)\left(\frac{1}{T}\right) + \text{constant} \quad (3.10)$$

$$\text{constant} = \ln(A) + \ln(O_2) \quad (3.11)$$

The activation energy of a reaction is the energy input required for said reaction. This is especially important for PM because the most convenient way to regenerate a DPF, after it is saturated with PM, is to oxidize the PM on the DPF while in use. This will allow the DPF to trap PM while also minimizing back pressure which could hinder the engine's performance.

Model PM and real diesel PM were oxidized on the metal fleece to compare oxidation of different soot nanostructures. The real diesel PM was sourced from the same light-duty diesel engine as with other analysis. The model PM is CBN330 and it is almost entirely carbon with primary particles that are on average 30 nm in diameter [45]. Although both diesel PM and CBN330 are primarily carbon, diesel PM is made up of unstable hydrocarbons and disordered carbon [22]. CNN330 is generally more graphitic and more difficult to oxidize due to this higher ordered carbon but this is the most similar in size to the primary particles that make up the carbonaceous soot in diesel PM [45]. By analyzing the oxidation of both PM, the impact of the experimental catalyst coating on different nanostructures will also be shown.



Figure 3.17 TGA equipment used in this research.

This material is reserved for educational use only, not allowed for commercial use.

3.2.7 Exhaust Emissions

Emission exhaust before the DOC, after the DOC, and after the P-DPF were analyzed using the pipes seen in the engine bench **Figure 3.1** with a gas analyzer (DITEST GAS 1000) and smoke analyzer (DISMOKE 480), both in **Figure 3.18**. This equipment did not include the measurement of NO_2 and the measured unit for CO could not be compared with CO_2 and so they were not included here. The emission properties that were analyzed were the gas opacity, temperature, CO_2 , NO, and O_2 . Each property was detected and measured using different sensors. The gas opacity was based on the comparison of how much light was absorbed or diffracted by the black PM smoke using a laser source where 0% having no change in the light when comparing the laser source and sensor. The gas opacity machine was used here because it is the same method and technique that current old vehicles are tested with. The engine was run at three engine speeds of 1000, 1500, 2000 rpm and two engine loads of 112 and 140 Nm. Generally, higher loads produce more PM and higher engine speeds produce less PM but the inverse for NO_x .

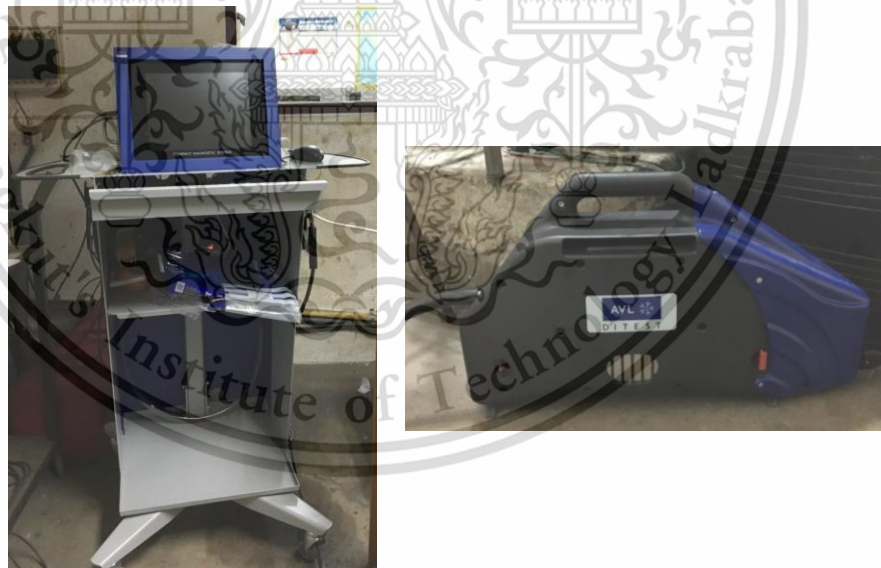


Figure 3.18 AVL equipment consisting of (left) gas analyzer and (right) opacimeter.

Chapter 4

RESULTS AND DISCUSSION

4.1 P-DPF Material and Trapping

4.1.1 P-DPF Material

First to analyze the metal fibrous fleece, SEM was done with **Figure 4.1** showing the metal fibers that make up the metal fleece used in this research. These fibers are 20-30 μm in diameter. To produce the P-DPF, these fibers are randomly nonwoven into a fleece. This fleece is then wound together with a flow guide foil such that a portion of the exhaust gas is forced towards the filter. This filter allows some PM to become trapped on the fibers. To maintain its peak trapping performance, the filter has to oxidize the trapped soot, which will be discussed in a later section.

Next, EDS was done with the SEM equipment, and it shows that the fibers alone do not have catalyzing elements. The resulting spectra is shown in **Figure 4.2**. It is made up of Fe, Cr, Al, and C with a trace amount of Si. The first three elements must be the main elements that make up the alloy used in this fiber, which would be a type of stainless steel due to the presence of the Cr. Stainless steel makes sense as a material to be used here because of its corrosion resistant properties and ability to withstand thermal cycling. These properties should also allow a long lifetime of the product with little to no maintenance. The C detected here could be from the contamination of dust and from the strengthening alloy. The Si should from the lubrication that is used to produce these metal microfibers [46]. The elements detected by the EDS can be seen in **Table 4.1**.

Figure 4.3 shows the microstructure of the metal fibers at a magnification of 3000x. It can be seen that the surface is full of small external grains less than 1 micron in diameter. They also seem to be in some pores of the fiber. These grains also seem to be in a linear formation with relation to the length of the fiber. The lack of chips and the mentioned continuous linear pattern points towards a drawing method which was used by some manufacturers [47]. Now that the raw metal fleece that make up the P-DPF is known to have no catalyzing material and is made of a stainless steel alloy, the coating will be done.

This material is reserved for educational use only, not allowed for commercial use.

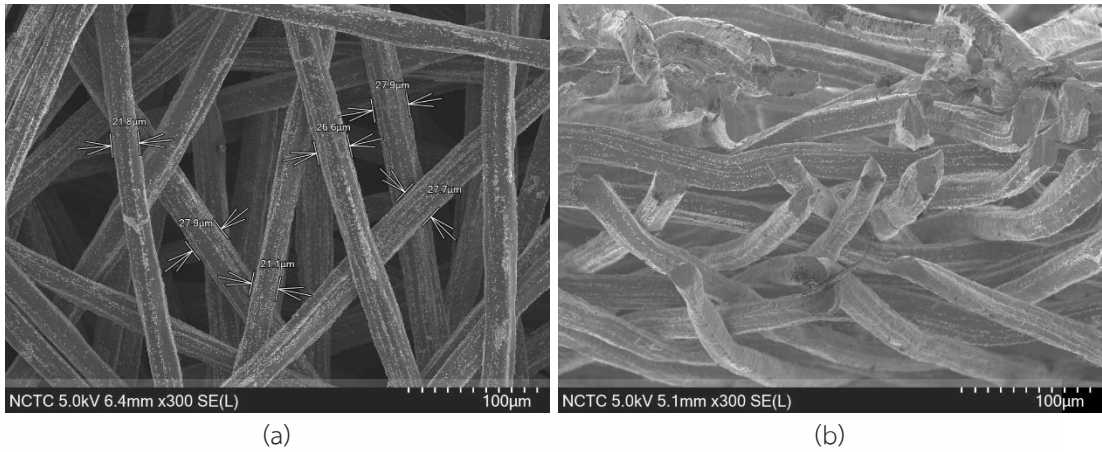


Figure 4.1 SEM of metal fibers in 300 magnification in (a) top view and (b) side view.

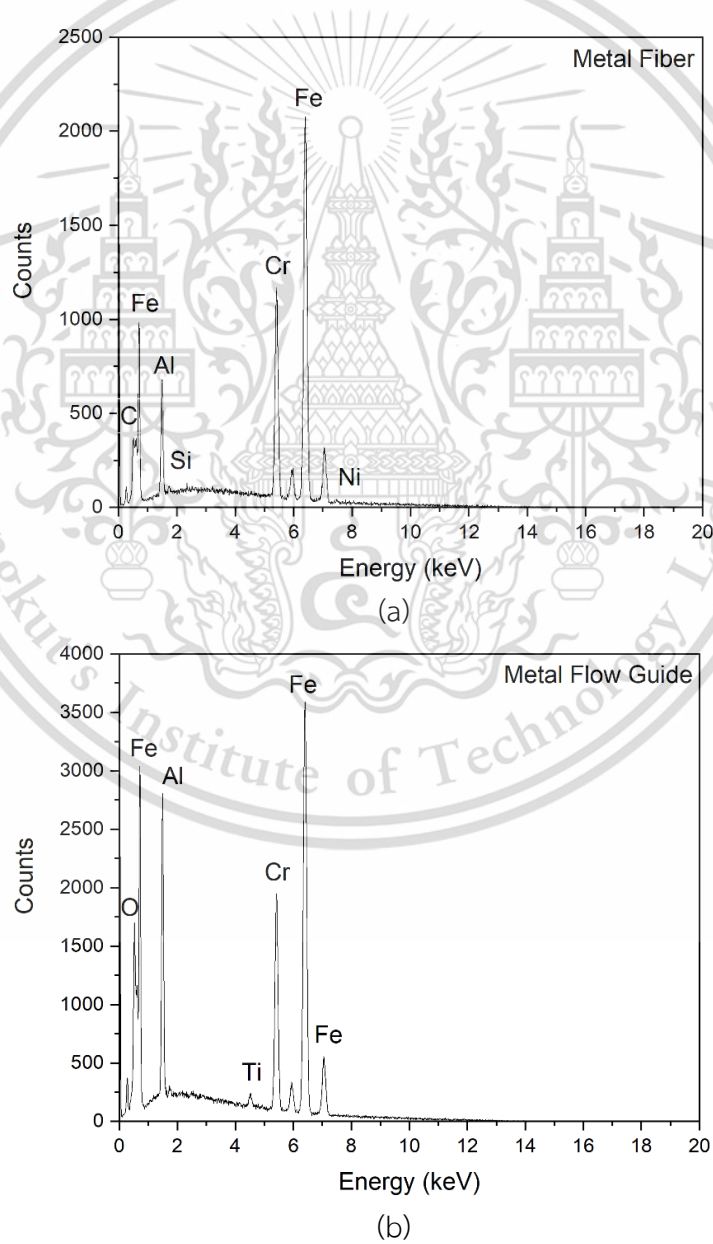


Figure 4.2 EDS spectra of (a) metal fiber and (b) metal flow guide.

This material is reserved for educational use only, not allowed for commercial use.

Table 4.1 Summary of elemental composition using EDS.

	Elements (weight %)							
	Fe	Cr	Al	C	O	Ni	Si	Ti
Metal Fiber	69.4	20.7	3.3	3.0	2.6	0.9	0.2	-
Metal Flow-guide	60.9	17.9	6.9	5.1	8.4	-	-	0.7

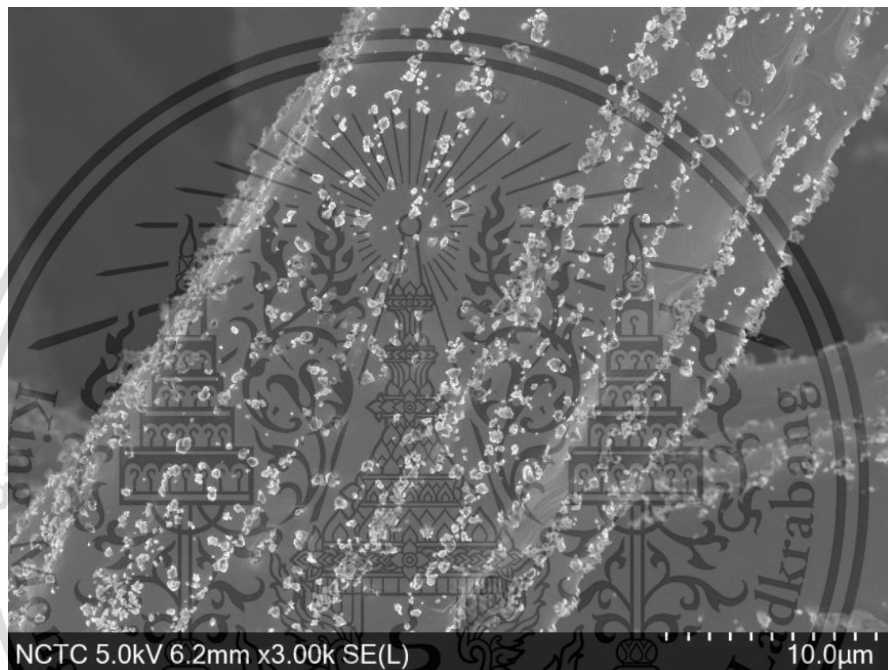


Figure 4.3 SEM of metal fiber in 3000 magnification showing surface microstructure.

4.1.2 P-DPF Coating

Power sources of 100W, 125W, and 150W were used for 20 minutes on a Si wafer to confirm the sputtered coating was in fact CeO_2 instead of the O deficient Ce_2O_3 . The O deficient Ce_2O_3 is less efficient in catalytic performance as well. The analysis can be seen in **Figure 4.4** where x-ray diffraction was used to determine the phase locations of the sputtered coating. This graph also shows the phase profiles of CeO_2 and Ce_2O_3 from literature and public databases to compare the raw data with [48] [49]. All three power sources showed that the coating matched better with the CeO_2 phase locations than the Ce_2O_3 phase locations.

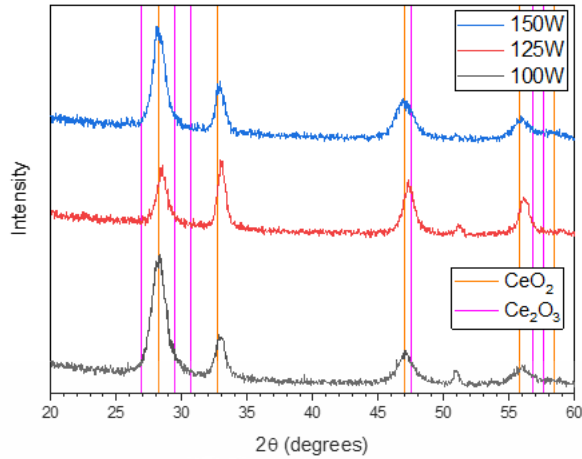


Figure 4.4 XRD spectra of Cerium Oxide coating using various power sources with profiles of two Cerium Oxide variants.

After the phases were confirmed, the 100W and 150W power sources were investigated to determine the deposition rates, the ideal power source, and depositing time. The initial coating trial can be seen for the 150W power source in **Figure 4.5**

Figure 4.5a shows the coating on a Si wafer to determine the coating thickness. The coating thickness was 70-92nm for the 150W power source and so the calculated deposition rate was over 5 nm/min.

Figure 4.5b and **c** show the metal fibers with the 20-minute coating. The fibers seem much smoother compared to **Figure 4.1** and **Figure 4.3**. This is due to both the coating and the cleaning that occurs during the pre-sputtering phase which may oxidize some contaminants on the surface of the fibers.

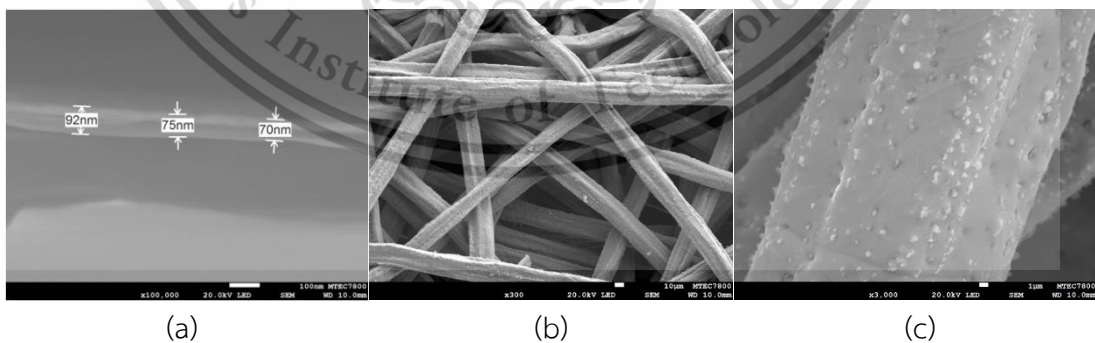


Figure 4.5 SEM showing (a) coating thickness, (b) coated metal fibers, and (c) coated surface of a metal fiber using 150W and 20min.

For the next step, the deposition time of 1 hour was chosen to achieve a minimum of 300nm coating thickness. The result of the coating can be seen in **Figure 4.6** and This material is reserved for educational use only, not allowed for commercial use.

Figure 4.7, for the 100W and 150W power sources. The thickness was measured to be around 125-135 nm for the 100W power source and 337-354 nm for the 150W.

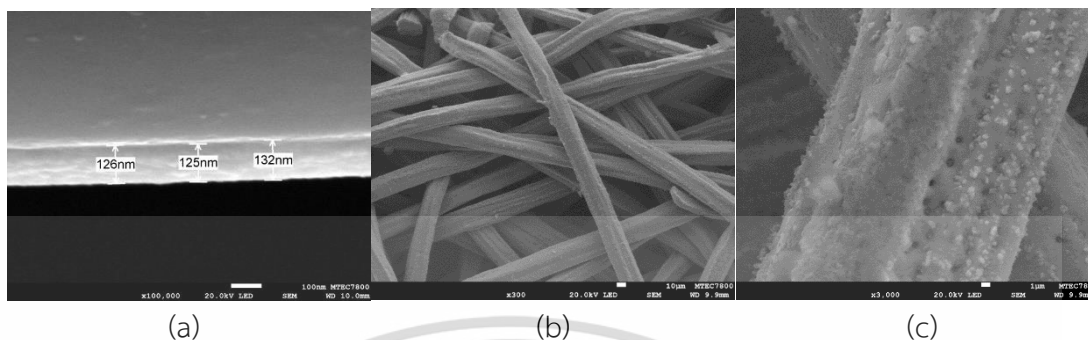


Figure 4.6 SEM showing (a) coating thickness, (b) coated metal fibers, and (c) coated surface of a metal fiber using 100W and 60min.

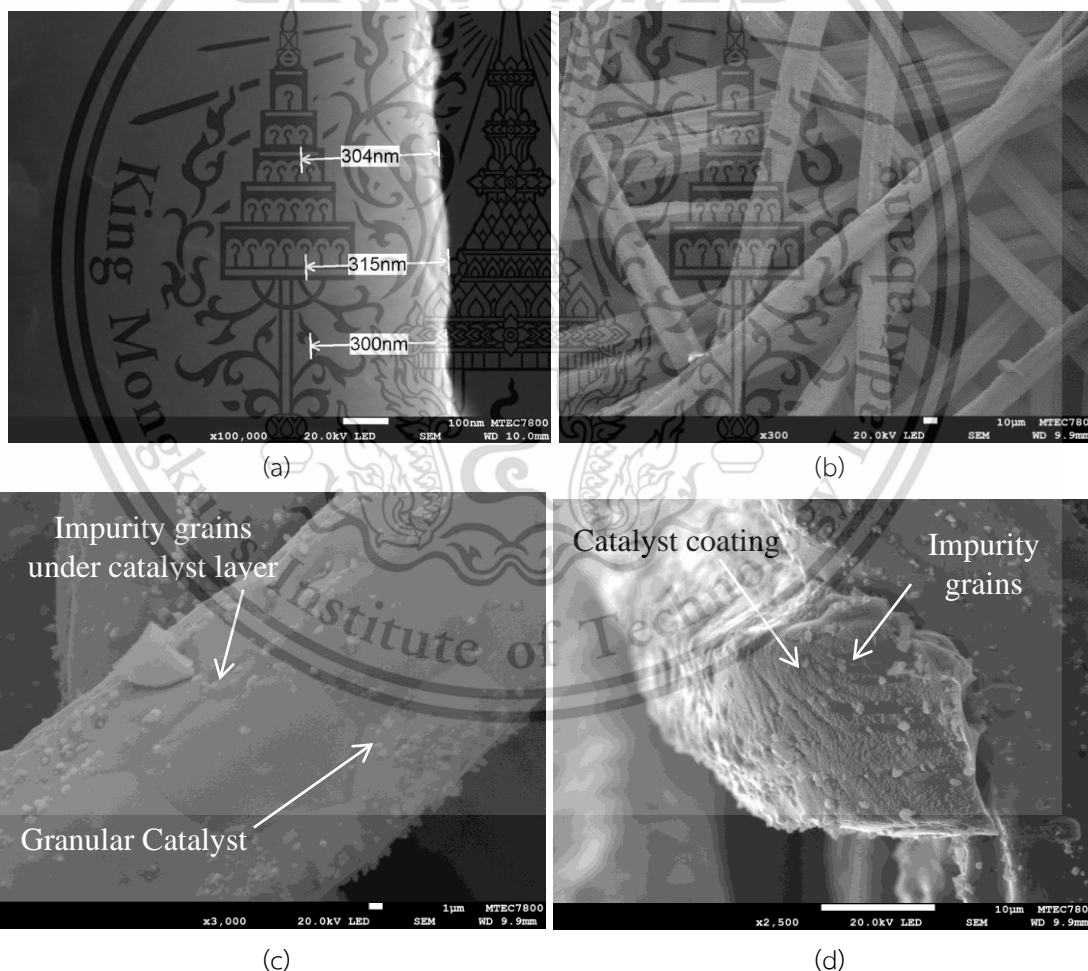


Figure 4.7 SEM showing (a) coating thickness, (b) coated metal fibers, (c) coated surface of a metal fiber, and (d) shorn surface of coated metal fiber using 150W and 60min.

This material is reserved for educational use only, not allowed for commercial use.

Forbidden to modify the content, and cite the document when use.

Since the substrate type does not significantly alter the deposition and formation of the coating in a sputtering PVD method, a consistent deposition rate was assumed across both the Si wafer and the metal micro-fibrous fleece [50]. This would mean that the coated fibers would still maintain their high porosity as this addition of thickness was only 2% of the original diameter. This was less than the deviation of the fiber diameter seen in **Figure 4.1** which would mean porosity of the filter media would stay virtually unchanged.

The coated fleece that would be used with soot in the TGA was the fleece that used the 150W power source for 60 minutes seen in **Figure 4.7b - d**. The surface is much smoother than before due to the uniform coating by the PVD method. The impurity grains can still be seen but it is essentially buried under the CeO_2 coating. The coating is also quite difficult to distinguish at some areas due to how thin of a film it is. However generally, the coating seems to be a much lighter in color compared to the raw fleece. But before the TGA was done, the quality of the coating needed to be analyzed.

Figure 4.5 SEM showing (a) coating thickness, (b) coated metal fibers, and (c) coated surface of a metal fiber using 150W and 20min. **Figure 4.6a**, and **Figure 4.7a** shows the dense coating with no pores or internal cavities. This meant that the PVD method with the RF sputtering was effective in the coating process. However, when this coating was done on the metal microfiber fleece, some areas formed granular CeO_2 instead of a uniform coating. This can be noticeable in **Figure 4.7b**. This can be mistaken for the previously rough surface of the uncoated metal fibers, but the grains are different in that they are grouped together and on top of each other instead of in a linear formation. They are also larger than the impurity grains from before. Although the catalyst grains are not ideal in terms of the coating, it could be beneficial to the oxidation of the PM as there is more surface area and therefore more potential contact between the catalyst and the soot. However, the grains could mean that the coating was not dense and could flake off.

And so, a section of the metal fleece was cut off using a metal shear to see how the coating would behave when under stress. This can be seen in **Figure 4.7d**. This image shows the direction of the cut, but it also shows that the coating behaved like flour stuck on a piece of dough. The coating did not flake off and when the deformation occurred, the coating moved with the metal material. This shows that the

This material is reserved for educational use only, not allowed for commercial use.

coating was well done with the material bonding well with the metal fiber instead of forming a shell-like outer layer of the coating.

4.1.3 P-DPF Trapping Behavior

Before analyzing it, PM was trapped on the P-DPF microfibers and observed using SEM. The trapping behavior and mechanism is complex in the P-DPF because of the partial flow nature and the deposition of the PM on the fibers. The initial trapping was simulated by introducing raw diesel engine exhaust to a piece of metal microfiber fleece for 1 second. The resulting trapping can be seen in **Figure 4.8** at magnifications of 1000x and 10000x. This initial PM trapping is focused on the impure grains and shows some dendritic formation, with the soot layer being approximately 1 μ m thick on top of these grains. The smooth metal areas with no impurity grains seem to have little to no PM on it. It should be noted that these images are taken from a top view of the fiber, where the flow of the exhaust was forced towards. This may influence what the SEM was able to observe.

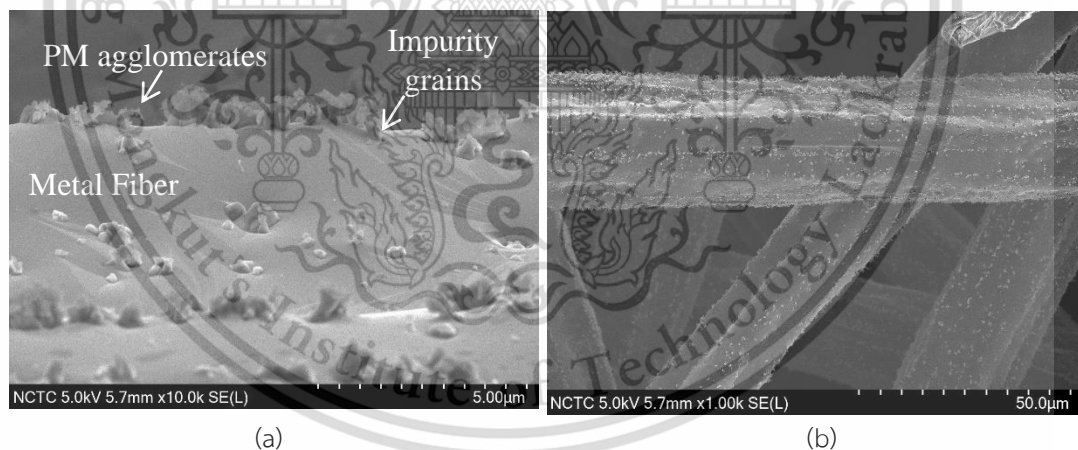


Figure 4.8 PM trapping on the metal fibers after 1s with (a) 10k magnification and (b) 1k magnification.

Figure 4.9 shows the metal fibers after 30s of trapping PM. This shows the subsequent \sim 5 μ m thick soot layer formation and growth of the trapped PM. The PM is seen to be attracted to each other and is on top of other PM instead of the clean metal surface. The growth of the PM on top of other PM instead of new surfaces also suggests a preferential behavior and supports the dendritic growth model. The contact

This material is reserved for educational use only, not allowed for commercial use.

between the fibers and the PM is quite low as a significant portion of the PM is located on top of other PM. Due to this trapping behavior, it can be reasonable to say that oxidation on the fibers will be dominated by the exhaust gas and high interaction between the gases and the trapped PM instead of the effect of the fibers themselves. This also shows that since trapping does not produce a soot cake layer, oxidation will occur simultaneously. But this will be tested using TGA later.

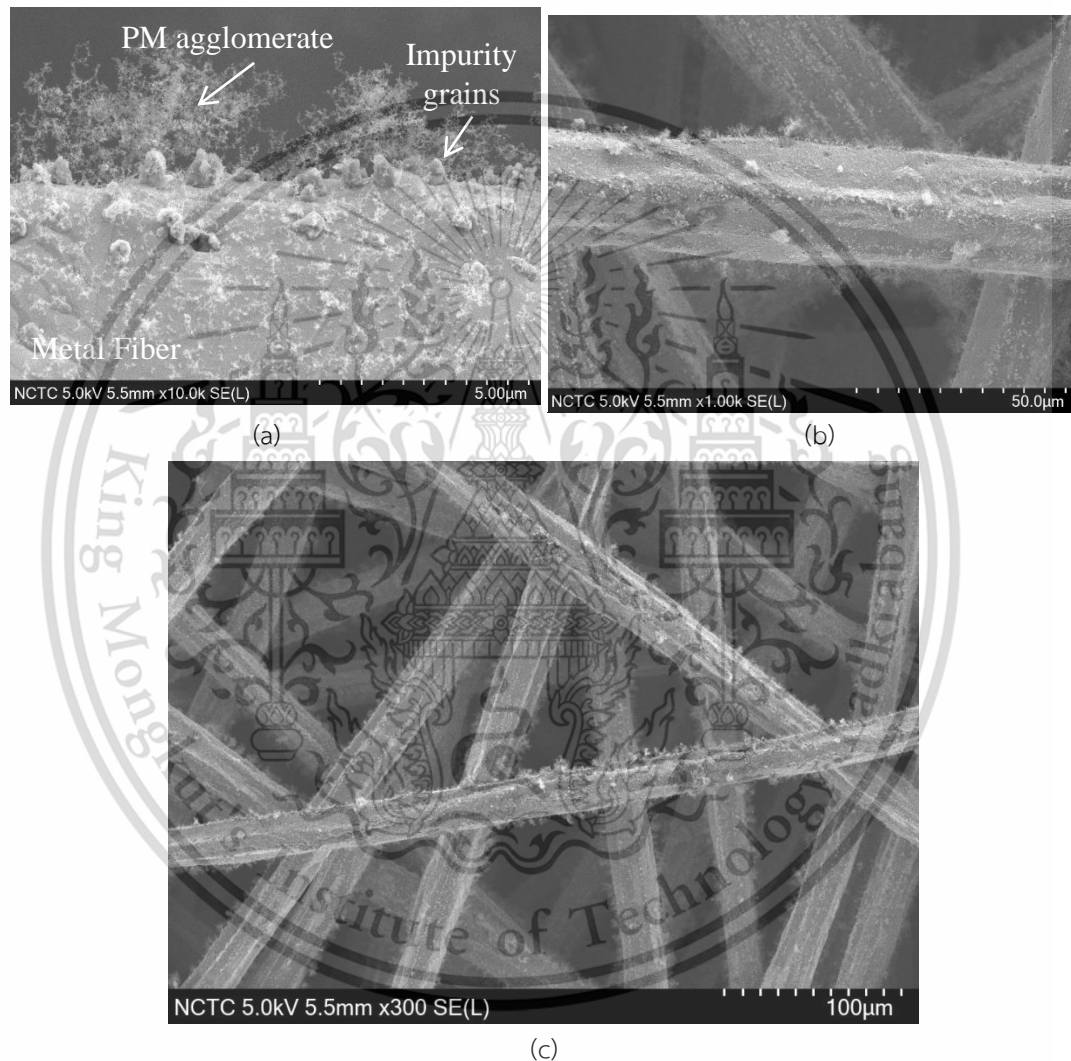


Figure 4.9 PM trapping on the metal fibers after 30s with (a) 10k magnification, (b) 1k magnification, and (c) 300 magnification.

The overall image of the 30s trapping seen in **Figure 4.9** can be compared with the manually loaded fleece in **Figure 4.10**. The manually loaded fleece was done to consistently load PM on the metal fleece when preparing the samples for the TGA.

These two methods would be compared to see if the manually loaded fleece could

represent the heavily loaded realistic PM trapping. The realistic simulated trapping shows PM trapped in dendritic clumps on top of the initial layer of PM. The manual soot trapping is much denser and is not as uniformly distributed as the realistic trapping. It seems that some sections of the metal fleece has no PM trapped. Fig.12 shows the contact between the PM and the metal fibers. The manually trapped PM is denser and there seems to be more PM on the fibers than the realistic trapping, but the PM trapping is quite similar for both trapping conditions in some segments of the surface. It should be noted that there is more contact between the PM and the fiber which may allow more influence of the catalyst, although the higher interaction between the airous PM and the exhaust gases will not be replicated in the TGA.

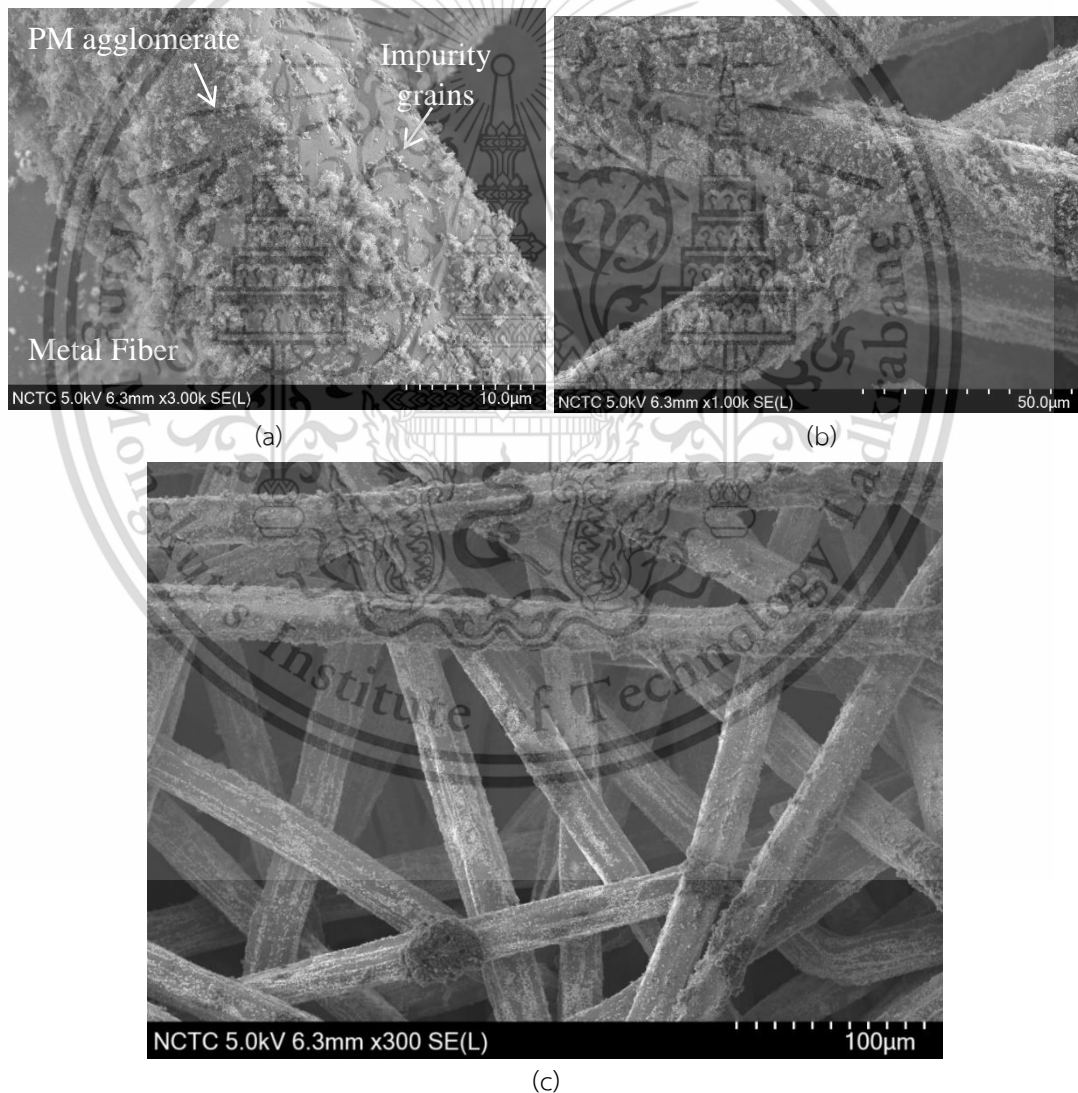


Figure 4.10 PM trapping on the metal fibers using manual loading with (a) 10k magnification, (b) 1k magnification, and (c) 300 magnification.

This material is reserved for educational use only, not allowed for commercial use.

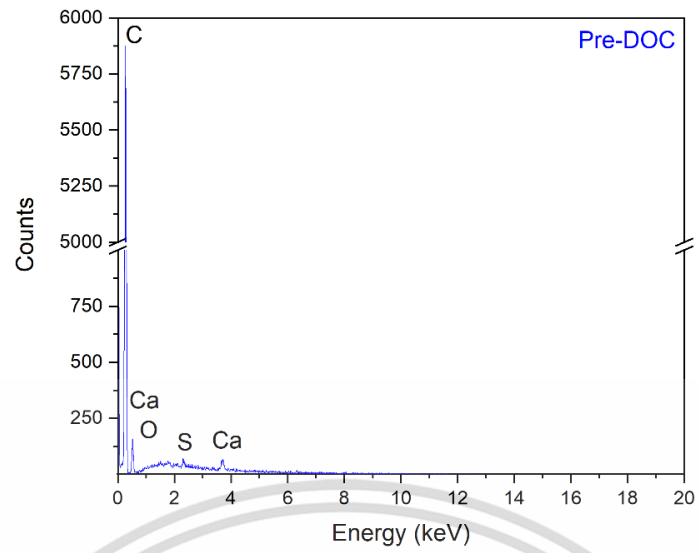
Forbidden to modify the content, and cite the document when use.

4.2 Soot Nanostructure and Composition

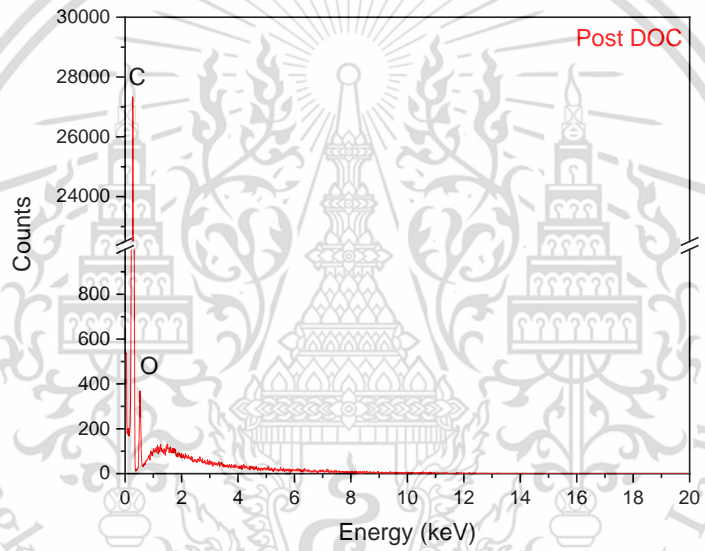
4.2.1 Elemental Composition

To see how the PM was affected by the trapping process seen in the previous section, PM from different sections were analyzed. **Figure 4.11** shows the resulting EDS spectra from soot before entering the DOC, between the DOC and P-DPF, and after leaving the P-DPF to see if the DOC and or P-DPF had contaminated PM with material from the DOC or P-DPF. The results are also summarized in **Table 4.2**. This confirms that PM is mostly carbon with the minimum carbon content being over 90% across all the spectra tested. The carbon content seems to increase, but not significantly, as the location shifts towards the end of the after-treatment system. The oxygen content also decreases as the location shifts towards the end. This could be due to the oxidation that occurs in each component of the exhaust after-treatment system. The element analysis also reveals the effect of the system on the PM. There is a higher S and Ca content before the PM enters the DOC, which could come from the engine lubricant and fuel impurity [51]. The S and Ca content may then bond to the catalyst material and cause catalyst poisoning [52]. This is supported by the drastic reduction of the S and Ca. However, in both the post-DOC and post-P-DPF, trace amounts of the engine lubricant and fuel impurity elements can be seen in the form of S and Cl. Fe can be seen in the post-DOC which may be from contamination from collection method. An addition of Al can be seen in the post-P-DPF, which may come from the P-DPF, after comparing the spectra of the fibers and flow guides. Overall, there is little to no chemical leakage from the exhaust after-treatment system to the PM. In fact, it can be argued that impurities or potentially dangerous elements are reduced by the exhaust after-treatment system, albeit due to catalyst poisoning.

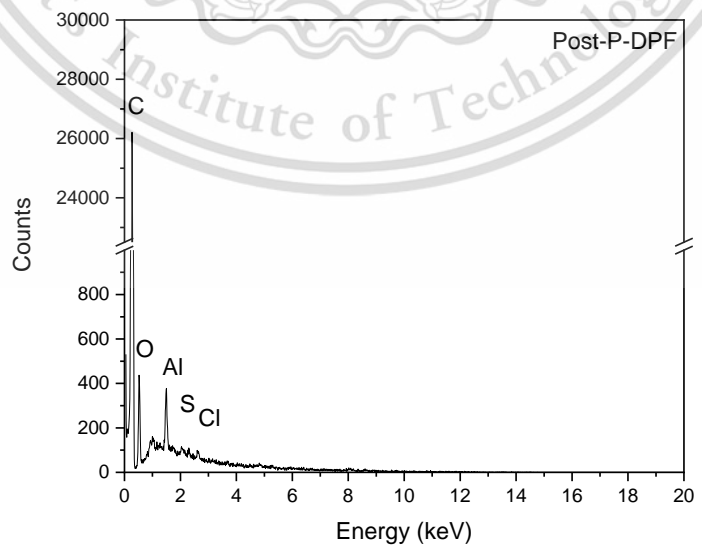
Next, since the results from the EDS showed that the PM was not significantly affected by the DOC but rather more affected by the fuel impurity, the morphology of the PM would be analyzed with respect to the agglomerate and primary particle sizes. This would be to investigate how the trapping process in the P-DPF and the continuous flow in the DOC would affect the PM's size in both the nucleation mode and accumulation mode.



(a)



(b)



(c)

Figure 4.11 EDS spectra of PM from (a) pre-DOC, (b) post-DOC, and (c) post-P-DPF.

This material is reserved for educational use only, not allowed for commercial use.

Table 4.2 Summary of elemental composition of PM from different locations in exhaust after-treatment system using EDS.

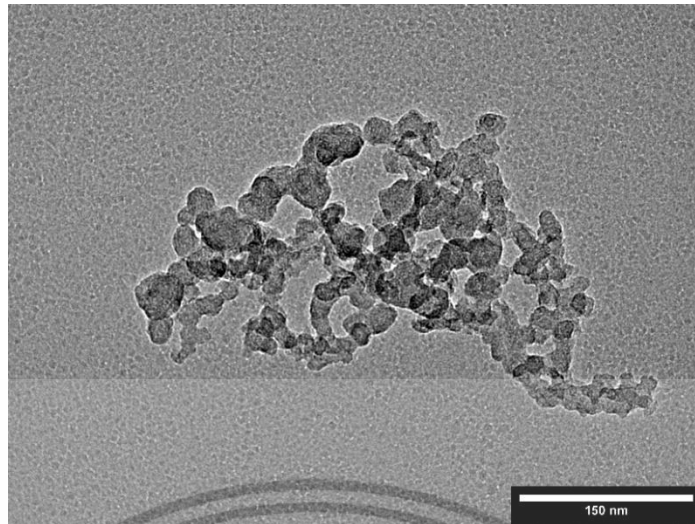
	Elements (weight %)						
	C	O	S	Ca	Fe	Cl	Al
Pre-DOC	90.6	7.7	0.4	1.3	-	-	-
Post-DOC	90.4	9.0	0.1	-	0.5	0.1	-
Post-P-DPF	94.0	5.1	0.1	-	-	0.1	0.7

4.2.2 Morphology

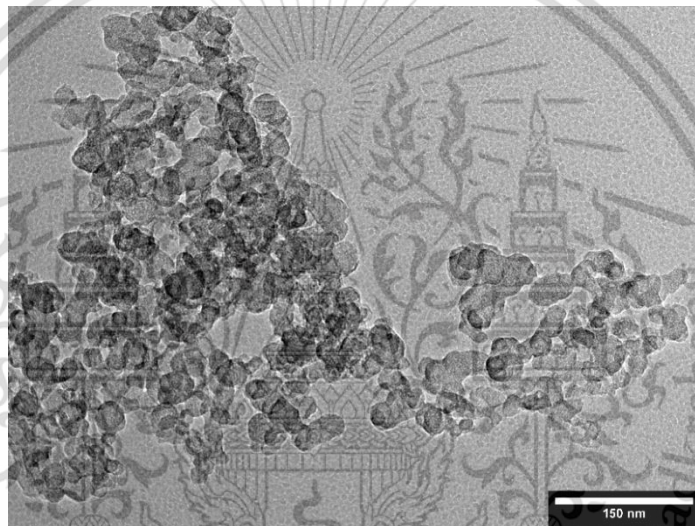
The same soot from the previous section was analyzed with TEM and nanoparticle size analyzer. **Figure 4.12** shows the TEM images of agglomerate particles of PM sourced from the different sections of the after-treatment system. The nanoparticle size analyzer detected the agglomerate particles as well as primary particles, seen by the double peak in **Figure 4.13a**. The average agglomerate sizes of 170nm, 220nm, and 450nm for PM from pre-DOC, post-DOC, and post-P-DPF, respectively. The single primary particles that make up the agglomerate particles were then analyzed using TEM at a magnification of 100,000x. The measurements were made into a particle size distribution graph in **Figure 4.13b** with average primary particle sizes of 25.2nm, 29.1nm, 27.6nm for the PM from pre-DOC, post-DOC, and post-P-DPF, respectively. The agglomerate and primary particle sizes increased along the after-treatment system.

From **Figure 4.12**, there is no obvious indication that any oxidation occurs although the P-DPF is designed to trap and oxidize PM simultaneously. However, this is because the conditions may not be optimal for oxidation at all times [37]. This points to the two different functions occurring: trapping and partial oxidation. Trapping could encourage the interception of carbon crystallites onto the carbon primary particles, which could explain the size increase seen in both analysis methods. Partial oxidation should leave behind evidence such as graphitic soot as the amorphous soot is oxidized [19]. However, the existence of the nucleation mode in **Figure 4.13b** could hint at breakup occurring due to oxidation. The nanostructure will thus be analyzed next to help understand the full picture of what is occurring here.

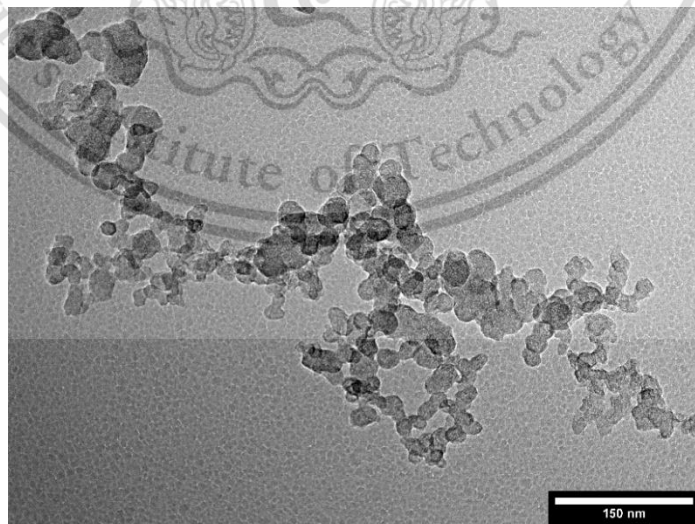
This material is reserved for educational use only, not allowed for commercial use.



(a)



(b)



(c)

Figure 4.12 TEM images of PM Agglomerates from (a) Pre-DOC, (b) Post-DOC, and (c)

Post-P-DPF.

This material is reserved for educational use only, not allowed for commercial use.

Forbidden to modify the content, and cite the document when use.

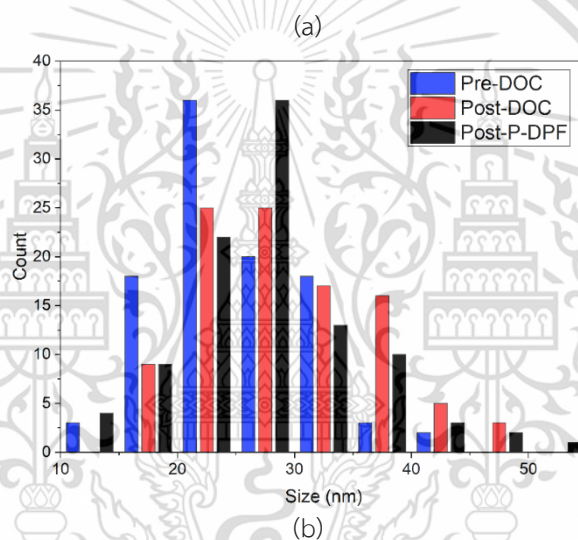
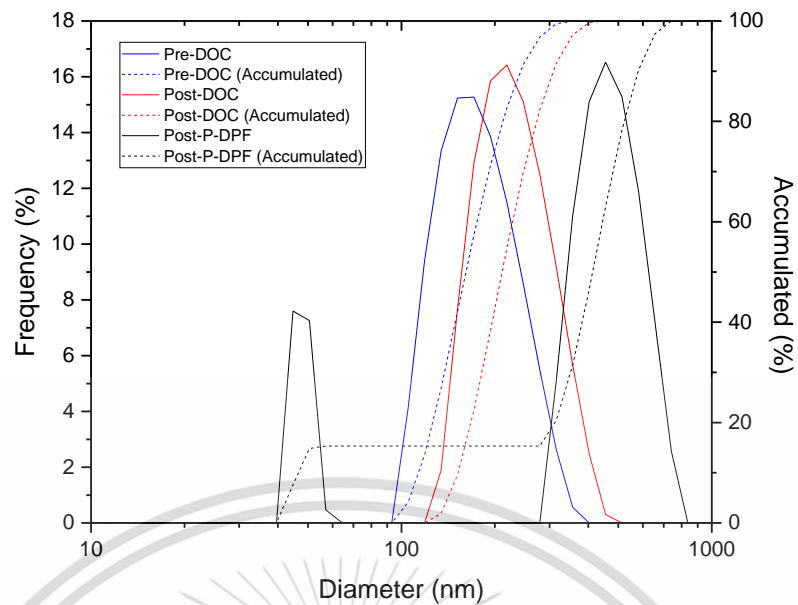


Figure 4.13 Particle size distribution from (a) scattering light method and (b) ImageJ with TEM analysis.

4.2.3 Nanostructure

4.2.3.1 TEM

Figure 4.14 shows the individual single primary particles and the carbon fringes that represent the carbon crystallites that make up the single primary particles. These TEM images were further analyzed using an image processing software. An initial step of polarizing the TEM image into black and white reveal the fringes that represent the carbon crystallite nanostructure seen in the 20x20nm images in Figure 4.15. An

This material is reserved for educational use only, not allowed for commercial use.

evolution of the fringe pattern can be seen where both the Post-DOC and Post-P-DPF are cleaner than the Pre-DOC, showing some partial oxidation as mentioned before. However, the shortening of the fringes can also be seen between the Post-DOC and Post-P-DPF.

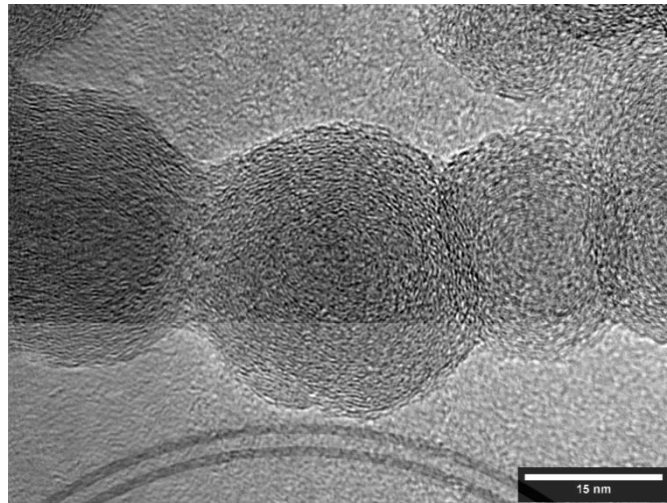
This analysis was continued in the **Figure 4.16** which shows the initial cropped image, converted black and white image, then the final skeletonized image. The details of these steps in this process were discussed in the methodology. The skeletonized images were then used to measure the lengths of the curved skeletonized fringes and interlayer or interplanar spacing. **Figure 4.17** shows the measured fringe lengths from **Figure 4.16** as a distribution plot. Although difficult to interpret, the distribution shows that the distribution curve shifts left suggesting that as the PM travels down the exhaust after-treatment system, the fringes are generally shorter.

This is supported by **Table 4.3**, which shows the summary results of the TEM fringe analysis. The average fringe length, maximum fringe length, and interlayer spacing is reduced by the exhaust after-treatment system. It should be noted that the overall exhaust after-treatment system did not significantly alter the maximum fringe length and interlayer spacing. In more detail, the fringe length and interlayer spacing, D-spacing, are usually inversely related to each other such that the reduction of one will increase the other. This is because the reduction of the fringe length is attributed to the reduction of graphitization or order, while the reduction of the interlayer spacing is associated with the increasing of graphitization due to the more compact crystallite structure [53]. It is also interesting that here the fringe length decreased while the single primary particle sizes from the morphology analysis seemed to increase. Even though the decreasing of the single primary particle size is usually paired with the decrease in fringe length [22]. These complicated phenomena will be further explained later with the comparison of the other methods.

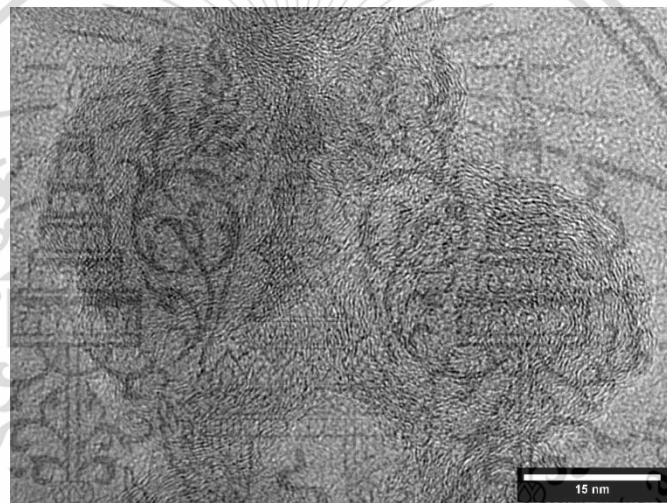
Table 4.3 Summary of TEM fringe analysis.

	Average (nm)	Total (nm)	Max (nm)	Count	D-space (nm)	D-space count
Pre-DOC	1.52	205	4.09	676	0.39	250
Post-DOC	1.44	209	3.91	730	0.38	232
Post-P-DPF	1.25	215	3.89	861	0.38	255

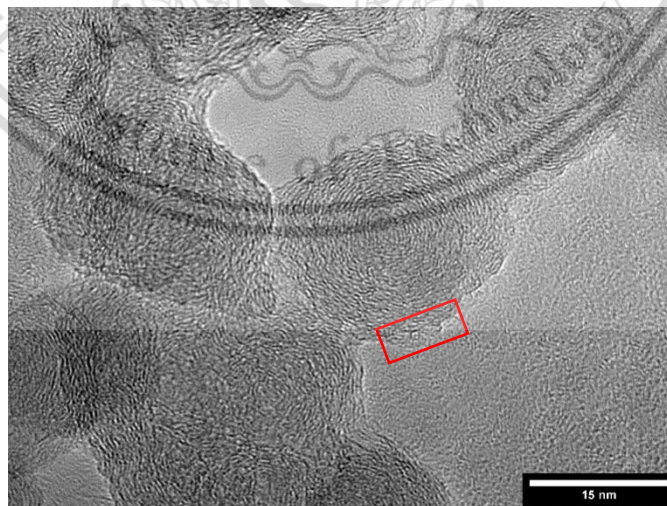
This material is reserved for educational use only, not allowed for commercial use.



(a)



(b)



(c)

Figure 4.14 TEM images showing nanostructure of PM from (a) Pre-DOC, (b) Post-DOC, and (c) Post-P-DPF.

This material is reserved for educational use only, not allowed for commercial use.

Forbidden to modify the content, and cite the document when use.

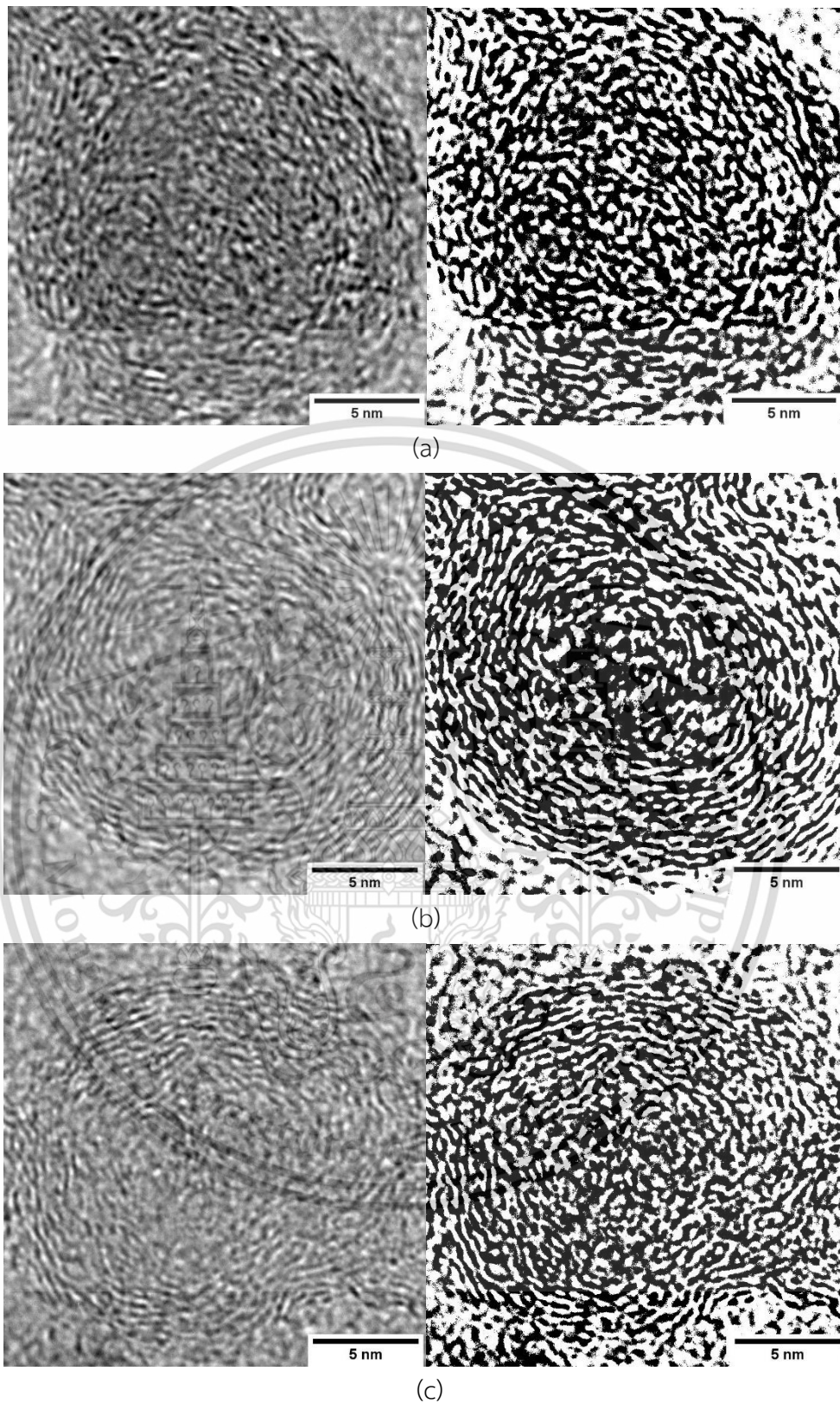


Figure 4.15 Black and white, 20x20nm images showing PM graphitic nanostructure from (a) Pre-DOC, (b) Post-DOC, and (c) Post-P-DPF.

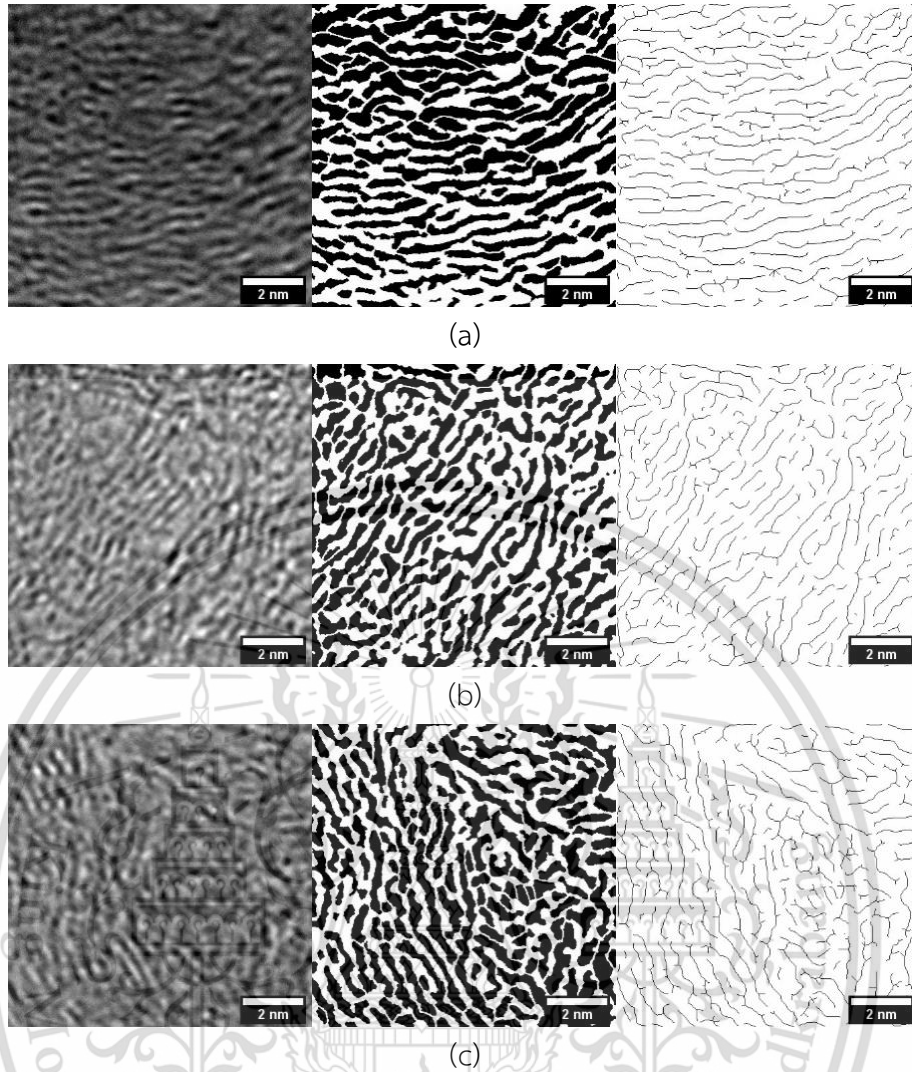


Figure 4.16 Process of analyzing TEM images for (a) Pre-DOC, (b) Post-DOC, and (c) Post-P-DPF.

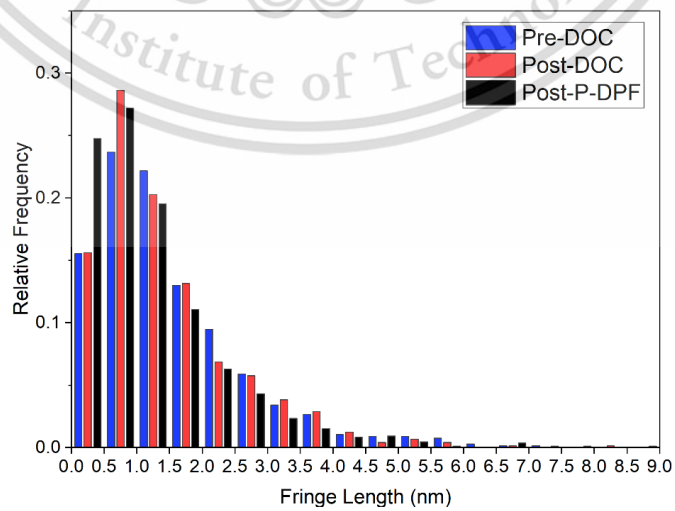


Figure 4.17 Fringe length distribution of PM along the exhaust after-treatment system.

This material is reserved for educational use only, not allowed for commercial use.

4.2.3.2 XRD

XRD was also used to analyze the PM as seen in **Figure 4.18**. The raw data was processed by using a model fit. Gaussian lines with R^2 higher than 0.95 modeled each of the curves with two curves representing a data set for the 002 and 100 planes. These Gaussian curves each gave parameters from its equation: FWHM, amplitude, and center. These parameters were then used to find the structural parameters using the equations shown in the methodology. The results of which can be seen in the middle sections in **Table 4.3** which show the comparison of all methods. It can be seen that the L_a using this method is much larger than the TEM. Nonetheless, the same trend can be seen where the L_a is reduced by the exhaust after-treatment system, but more significantly than what the TEM method showed. The d_{002} does not change significantly by the after-treatment system as a whole, but there is a small decrease after the DOC followed by a small increase after the P-DPF. The N parameter and L_c also mirrors this where both N and L_c increase after the DOC then decrease after the P-DPF. They show that the graphitization increases after the DOC most significantly. However, similarly to the TEM, the system does not impactfully change the density or compactness of the crystallite planes.

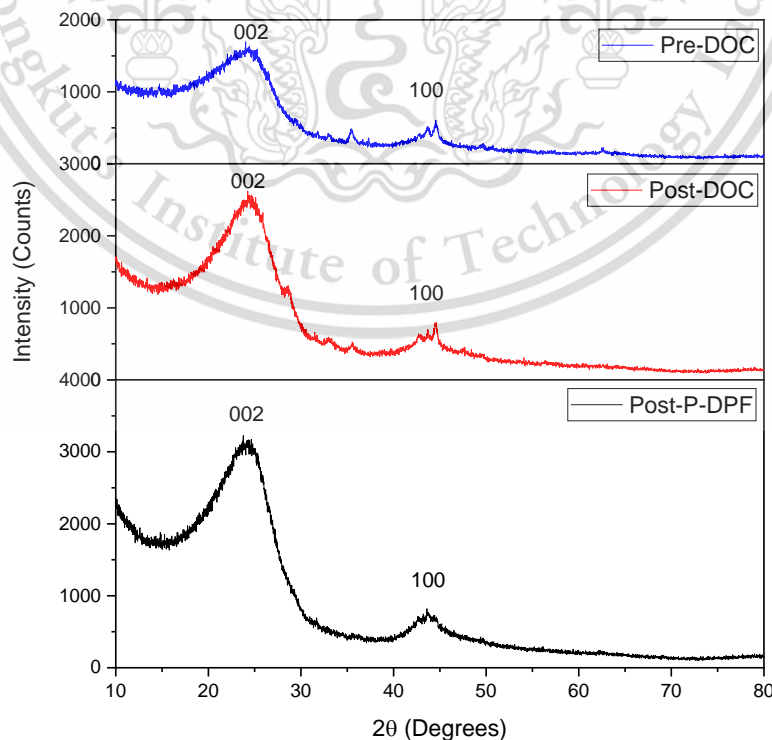


Figure 4.18 XRD spectra of PM along the exhaust after-treatment system.

This material is reserved for educational use only, not allowed for commercial use.

Table 4.4 Summary of all nanostructure analysis.

Samples	TEM Analysis		XRD analysis				RS Analysis
	D ₀₀₂ (nm)	L _a (nm)	D ₀₀₂ (nm)	N (nos.)	L _c (nm)	L _a (nm)	L _a (nm)
Pre-DOC	0.39	4.09	0.369	2.939	1.085	6.265	4.34
Post-DOC	0.38	3.91	0.366	3.113	1.139	5.731	4.10
Post-P-DPF	0.38	3.89	0.370	3.028	1.120	5.446	3.76

4.2.3.3 Raman Spectroscopy

Finally, the RS was done to show the spectra seen in **Figure 4.19**. This raw graph was then fitted with two Gaussian lines for each data set to determine the lines' parameters: FWHM, amplitude, and center. These were then converted to the intensity of the D band and G band ratio, I_D/I_G as seen in **Table 4.5**. It can be seen the I_D/I_G ratio increases along the after-treatment system. This means that the PM becomes relatively more disordered or amorphous, or the graphitization is decreased. This ratio can be converted to the L_a as seen in **Table 4.4**. The L_a also decreases as the location is moved towards the end of the system, which agrees with previous methods.

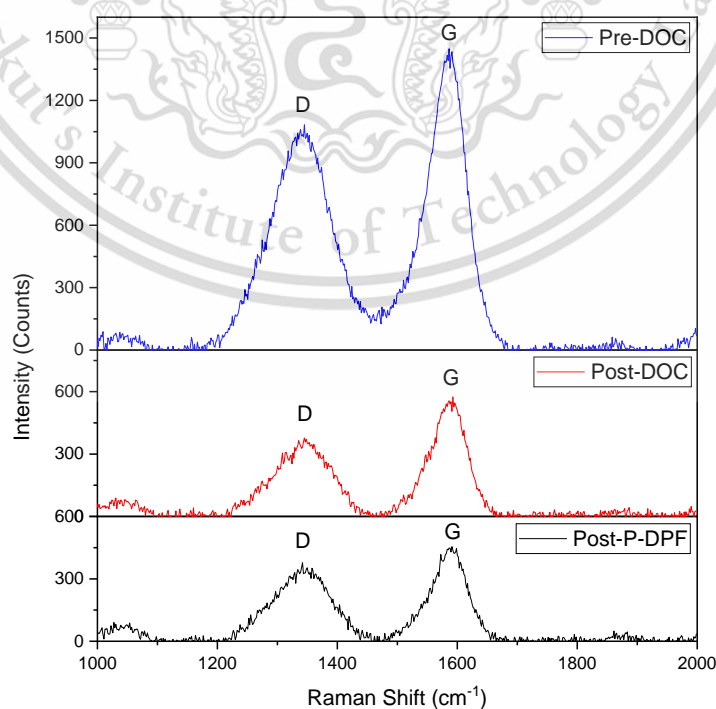


Figure 4.19 Raman spectra of PM along the exhaust aftertreatment system.

This material is reserved for educational use only, not allowed for commercial use.

Table 4.5 Summary of results for Raman spectroscopy.

Samples	D band Raman Shift (cm ⁻¹)	D band FWHM	G band Raman Shift (cm ⁻¹)	G band FWHM	I _D /I _G
Pre-DOC	1341	115	1580	78	1.03
Post-DOC	1340	106	1582	70	1.09
Post-P-DPF	1336	103	1583	73	1.17

4.2.3.4 Comparison of results

Now that all the results of the various different methods for analyzing the PM is known, they must be thoroughly compared. The pressing issue is that the morphology clearly show that the particle sizes increased, when comparing before and after the exhaust after-treatment system, yet the nanostructure showed the graphitization decreasing which is usually not the relationship seen between the morphology and nanostructure. The nanoparticle analyzer showed breakup occurring in the post-P-DPF PM, represented by the peak in the nucleation mode. To explain this, recent literature related to this manner of breakup or fragmentation was reviewed.

Liu et al. 2022 [54] investigated the fragmentation of primary particles and how it affected soot oxidation reactivity. It was seen that during aggregate fragmentation, the internal structure of soot was not destroyed. This meant that any oxidation that occurred to cause the fragmentation mostly affected the surface of the primary particles.

This may explain the duality of increasing particle size yet decreasing graphitization seen in this research. There is no evidence of internal burning in any TEM image but some evidence of surface oxidation in the form of curved fullerenes. It should be noted that more aggregate fragmentation was observed in conditions where the soot oxidation was moderate [54]. When there was more soot oxidation or fuller oxidation occurred, internal burning was more common and included a greater quantity of primary particle fragmentation [54]. This also decreased the fringe length and increased tortuosity which can both reduce the soot activation energy and allow faster and easier oxidation [21]. Then as the fragmented primary particles oxidize further, the fringe

length increases, and tortuosity decreases which can increase the soot activation energy and make it more difficult to oxidize [54].

The TEM fringe analysis in **Table 4.3**, shows that the number of fringes and the total length of the fringes both increases along the exhaust after-treatment system. This shows that more carbon crystallites are added since the analysis was done using the same 10x10nm square size. This is because the fuller oxidation described in the above literature did not take place in the DOC and P-DPF as there would not have been enough dwell time for this full oxidation to occur.

The L_a from all three soot nanostructure analysis methods overwhelmingly shows that the fringe length is decreased by the exhaust after-treatment system, which can represent a decrease in graphitization [53] [21]. This is also backed up by the TEM fringe analysis showing the average fringe length decreasing and the RS analysis showing the intensity ratio of the D band and G band increasing. However, the particle size distribution shows that PM increases in size in the single primary particle scale as it travels down the after-treatment system. The combination of increasing particle size and decreasing fringe length is intuitively contradictory. This shows the complexity of the effect of this exhaust after-treatment system. Previous sources have said that both the graphitization and sizes increase due to an exhaust after-treatment system [55]. However, it should be noted that these sources use a full-flow DPF which could significantly change the effects on the PM. This is because the physical path of the PM in the full-flow DPF and partial-flow DPF is significantly different. PM must flow through the filter material in a full-flow DPF while it may not interact with the filter material at all in a partial-flow DPF. The nature of the PM oxidation is different as PM is stored before active oxidation in the full-flow DPF while PM oxidation is continuous and partial in the partial-flow DPF.

As said in the introduction, full-flow DPF requires all exhaust to pass through a wall of the filter. The PM will have more obstructions and potential contact and/or interception due to the nature of the filter. Meanwhile, the partial-flow DPF, specifically this metallic fiber-based P-DPF, allows some exhaust fluid to avoid going through the fibrous filters, although it is all in the same control volume. The spacing between the fibers in the filter are also larger than what is seen in the wall flow filters, which allows more air flow and lower dwell time. This higher interaction with more air flow can also lead to the physical breakup or fragmentation of the PM without significant oxidation

This material is reserved for educational use only, not allowed for commercial use.

[56]. This breakup was possible due to chemical adsorbates on the surfaces of the primary particles which would lower the bonding strength between the primary particles that made up the agglomerate [56]. Nonetheless, a specific amount of exhaust PM will interact with the filter media with less potential contact in the P-DPF compared to the full flow DPF. However, it is reasonable that once PM is trapped in a P-DPF, it would interact more with the exhaust gas compared to the full flow DPF due to the lack of soot cake layer which can restrict the exhaust flow.

As for the oxidation or regeneration, the P-DPF will not utilize an active regeneration or oxidation with external energy input, under typical operating conditions. This leaves the only other method of oxidizing soot: passive oxidation. This means that the post-P-DPF in this research has been under continuous passive regeneration. Passive regeneration is usually done by utilizing the extra O molecule in NO_x to assist in oxidizing the C in the PM into CO and CO₂ by becoming adsorbed into the PM which forms an unstable intermediate that can be more easily oxidized by O₂ [28]. Numerous research has been done on this oxidation and how it differs to oxidation while using only O₂. Oxidation under O₂ usually falls under internal burning and surface oxidation. When there is NO_x present, it was found that internal burning was inhibited, and surface oxidation occurred [57]. Oxidation by O₂ is also preferential towards curved sites and end sites of the carbon fringes [58] [25]. When there is NO_x, it was found that this behavior was accelerated. For a partial-flow DPF under normal operating conditions, soot oxidation will occur continuously, albeit partially. This partial oxidation paired with the NO_x ability to promote edge and end site oxidation explains the near elimination of curved fringes seen in the internal structure of the PM in Figure 4.15. The abundance of straight carbon fringes suggests a level of graphitization. However, the outer surface in the red box in **Figure 4.14c** shows curved partially oxidized fringes that are similar in shape to the lamellae mentioned in other literature [59]. The broken-up fringes, or fullerenes, are formed due to oxidation at relatively low temperatures and low pressure, which P-DPFs are designed to operate under. If this occurs, then there would be fragmentation occurring between the single primary particles or on the bridging fringes between primary particles as this area has more disordered carbon crystallites which then allows more oxygen to diffuse into the oxidation sites [60] and explain the partial oxidation that is seen in the nanostructure analysis.

Overall, the combination of the soot nanostructure and the PM morphology reveals the phenomenon that occurs in the P-DPF. The seemingly contradictory results of the morphology and nanostructure analysis strongly supports the previously mentioned complex effect of the DOC and P-DPF exhaust after-treatment system. This is visualized in **Figure 4.20** with the simultaneous and continuous trapping and oxidation occurring in the metallic partial flow DPF. The continuous partial oxidation with the high dwell time in the P-DPF, which leads to more trapping and soot dendrite growth, results in larger PM with less graphitic soot.

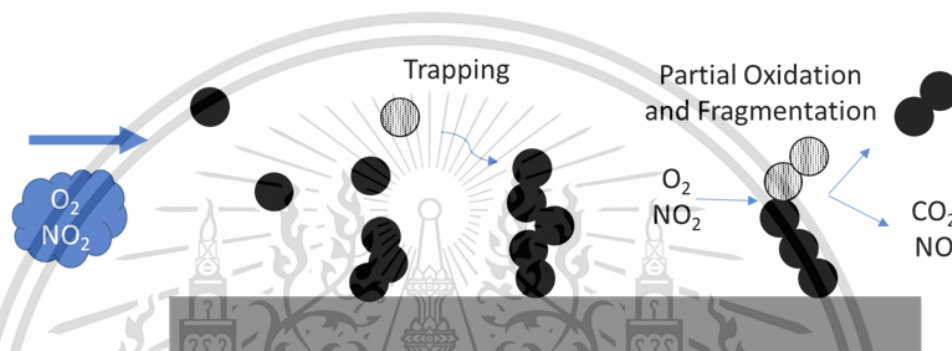


Figure 4.20 Simultaneous Trapping and Oxidation on Metallic Partial Flow DPF

4.3 Exhaust Emissions

4.3.1 Opacity

The gases before the DOC, after the DOC, and after the P-DPF were analyzed in terms of opacity, temperature, CO_2 , NO , and O_2 as shown in **Figure 4.21** to **Figure 4.25**, respectively. The opacity in **Figure 4.21** is seen to decrease after the DOC for most of the engine conditions as some PM is oxidized. However, the subsequent decrease of opacity is more pronounced as the P-DPF is doing its job of trapping PM. The effect of the P-DPF decreases at the higher loads and higher engine speeds. This could be due to the higher exhaust gas velocity at these conditions allow less dwell time or time to interact with the filter. The higher-than-expected opacity could also be from the blow-out phenomenon where the trapped PM is disturbed by the gas velocity and exits the P-DPF before it is oxidized further. This opacity result will be compared to with the other measured parameters.

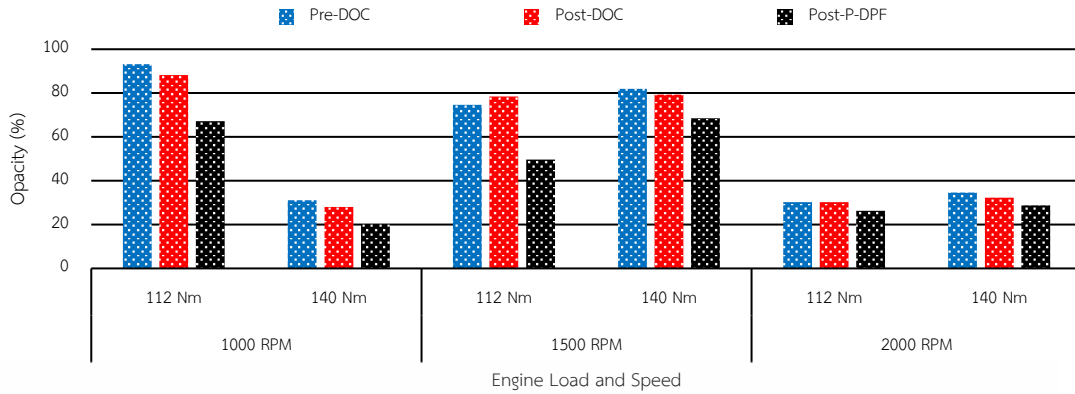


Figure 4.21 Opacity results along the exhaust after-treatment system.

4.3.2 Temperature

The temperatures in the after-treatment system can be seen in Figure 4.22. The measured temperatures increase after the DOC for most of the cases. This is because of the exothermic reactions that occur in the DOC. The temperatures then decrease after the P-DPF. This shows that heat is not generated in excess of the heat lost by diffusion to the metal internal structure and to the atmosphere by the walls. The difference of the temperature before and after the P-DPF could be from the air velocity or nominal heat generation from exothermic reaction of oxidizing soot in the P-DPF. It should be noted that every temperature recorded here was lower than what is usually needed for active oxidation to occur in order to fully oxidize PM.

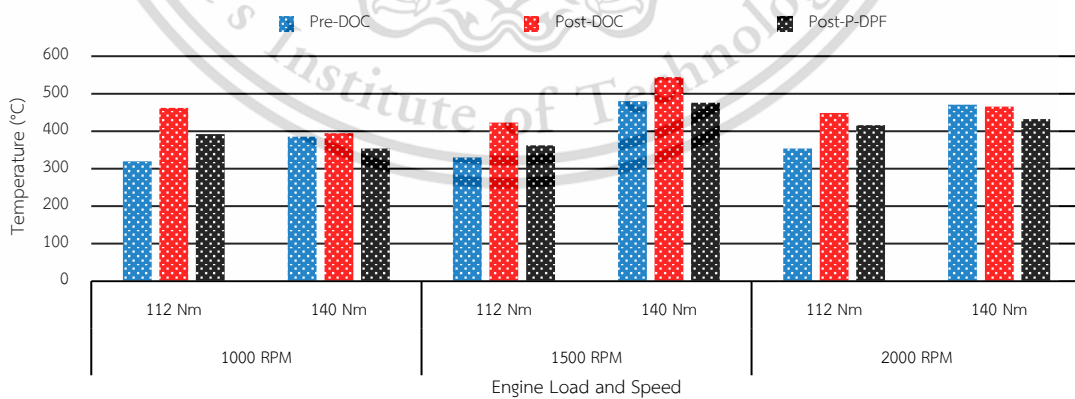


Figure 4.22 Temperature along the exhaust after-treatment system.

4.3.3 CO₂

This material is reserved for educational use only, not allowed for commercial use.

The CO₂ before the DOC, after the DOC, and after the P-DPF seen in **Figure 4.23**, under the unit of volume percent, paint a better picture of the reactions that occur in the exhaust aftertreatment system. In every condition, the CO₂ should increase after each segment. This is because HC, CO, and C oxidation increases CO₂. The DOC increases the CO₂ most significantly as the catalyst does its job. The CO₂ then increases after the P-DPF but not for every condition and not as efficiently for every condition. This subsequent increase in CO₂ should be mostly the conversion of C into CO₂ due to the lack of catalyst in this DPF. This undoubtedly proves that oxidation does occur in the P-DPF, although partially and not in every condition.

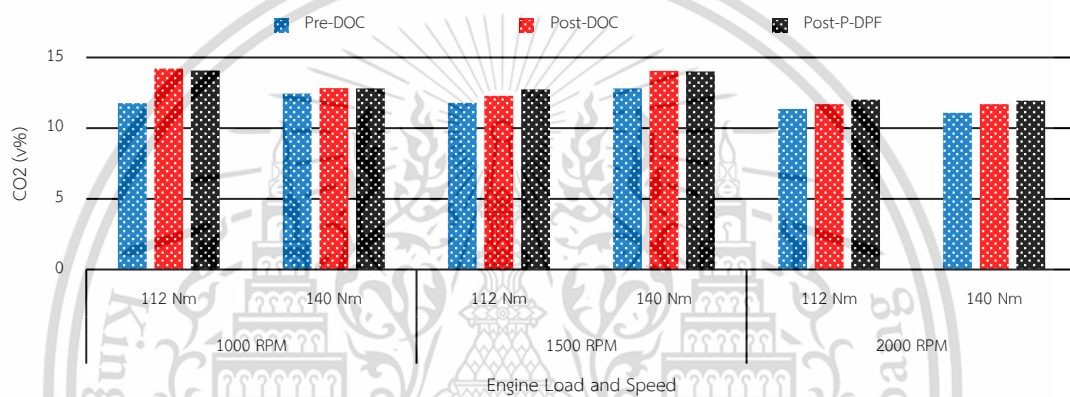


Figure 4.23 CO₂ measurements along the exhaust after-treatment system.

4.3.4 NO

This conclusion can be compared with the NO seen in **Figure 4.24** using the unit of ppm. When this parameter increases, it shows the reduction of NO₂ into NO as NO cannot form in the temperatures seen in this exhaust after-treatment system. When this parameter decreases, it shows the oxidation of NO into NO₂ that can occur in the exhaust after-treatment system. NO increased after the DOC at the 1000 and 1500 rpm conditions as NO₂ assisted in oxidizing gaseous hydrocarbons or partially oxidizing PM. This is supported by the increase in CO₂ in **Figure 4.23**. At the higher engine speed, less amounts of PM formed and so less NO₂ was converted into NO. Rather, the high temperature and engine conditions may have allowed the oxidation of NO into NO₂. In the P-DPF, NO₂ was used again to assist in oxidizing PM. This increased the NO in most of the conditions at this position. This will also be compared to the O₂ measurements.

This material is reserved for educational use only, not allowed for commercial use.

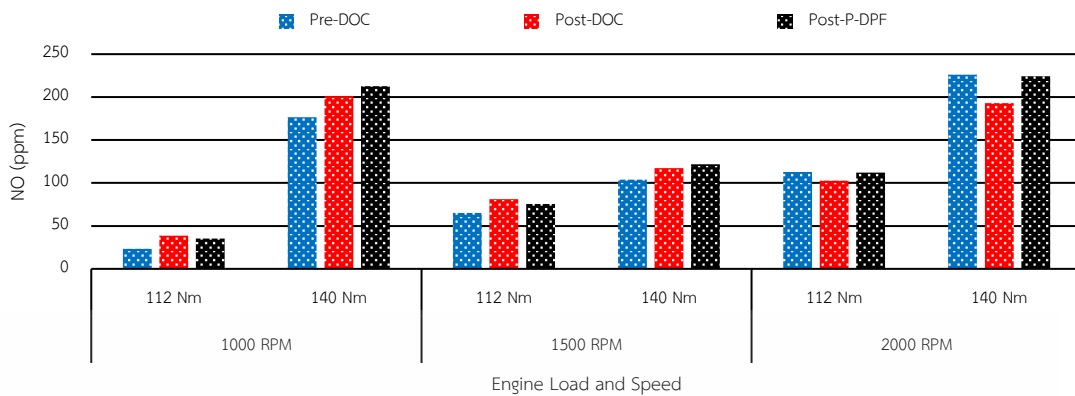


Figure 4.24 NO measurements along the exhaust after-treatment system.

4.3.5 O₂

Figure 4.25 shows the O₂ measurements in volume percent. It decreases after every segment because O₂ cannot form in this exhaust after-treatment system. The largest decrease is after the DOC which is supported by the increase in CO₂ in Figure 4.23. The subsequent lower decrease proves that oxidation occurs in the P-DPF as well. The decrease in O₂ after the P-DPF was more significant in the 2000 rpm conditions. The NO also increased after the P-DPF in these conditions. This shows that NO_x assisted soot oxidation occurred in the P-DPF as the reacted NO_x would have converted to NO and N₂. The increase of CO₂ after the P-DPF is also more significant in these conditions as well, supporting this claim. The temperature from before also show that active oxidation did not occur because the temperature was too low for soot oxidation to occur fully. This confirms the conclusion from the soot nanostructure analysis. The P-DPF did trap PM and allowed NO₂ assisted passive PM oxidation.

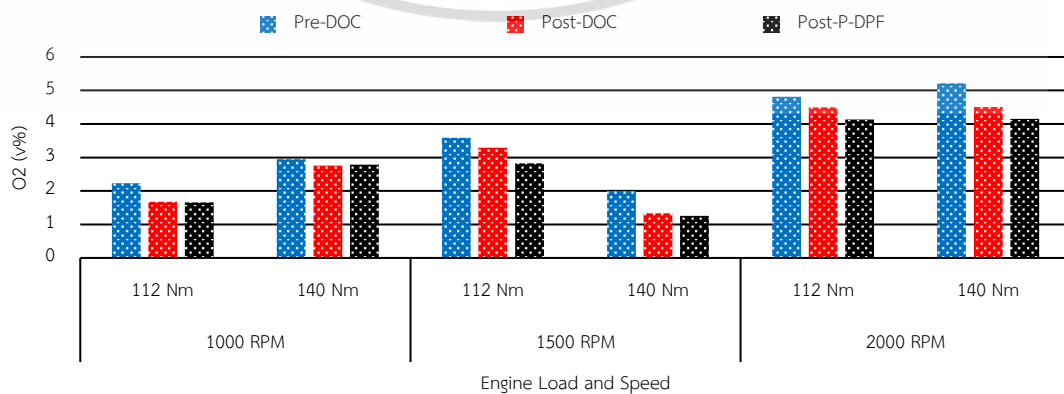


Figure 4.25 O₂ measurements along the exhaust after-treatment system.

This material is reserved for educational use only, not allowed for commercial use.

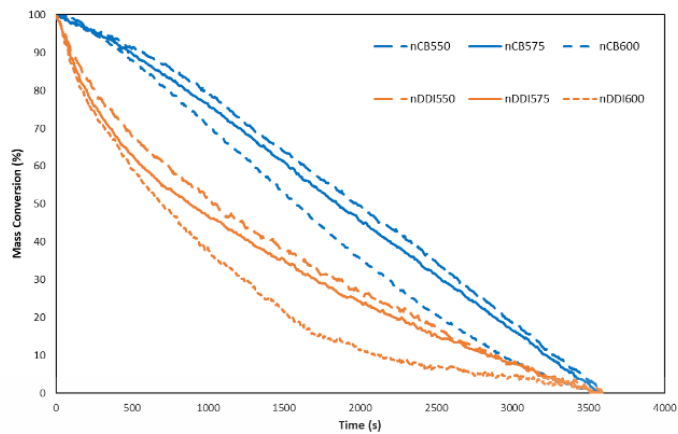
4.4 Soot Oxidation

4.4.1 No Coating

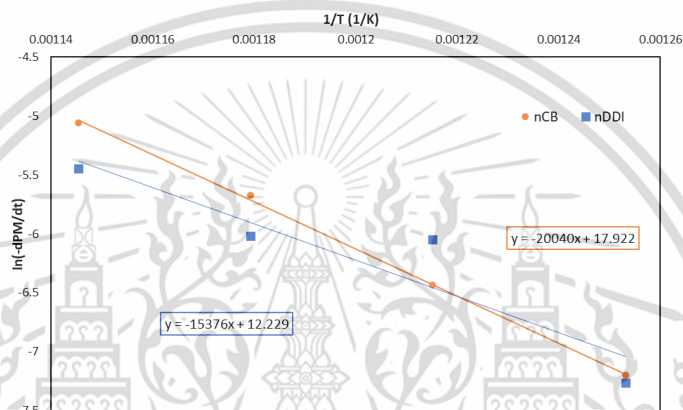
It was seen through the previous sections studying the PM and how it is affected by the exhaust after-treatment system, that the resulting PM that would be released to the atmosphere is still dangerous, although due to its larger size, it would not stay suspended in the atmosphere for as long as the smaller pre-DOC PM. The main difficulty in the P-DPF is the oxidation. The partial oxidation observed in the experimentations was too little compared to increasing PM size. It is obvious that reducing the energy required for this oxidation would be greatly beneficial.

As such, the fleece that was coated using the PVD method would be used to analyze this very purpose. But to have a direct comparison between the uncoated and coated fleece, and to analyze the effects of the structure of the soot on the uncoated metal fleece, TGA was done with the CBN330, denoted by nCB, and the diesel PM, denoted by nDDI. The n in “nCB” would refer to the oxidation occurring on the “non-coated” fleece. The mass conversion graph for these soot and uncoated fleece with key isothermal temperatures can be seen in **Figure 4.26a**. Here, as the isothermal temperature increases, the slope at which soot is oxidizes is steeper, which is self-explanatory. These slopes were then used to create the Arrhenius plot in **Figure 4.26b**. Each point in this plot is from a single isothermal mass conversion curve. The points then form a line in which the slope can be calculated to find the activation energy.

The activation energies for CBN330 and diesel PM on uncoated fleece were 167 kJ/mol and 128 kJ/mol, respectively. This comparable to previous literature despite the fact that the soot PM used here was a mixed media with the powder soot PM on the fleece and not just the powder like in the literature [13]. As such, it can be said that the raw fibers did not significantly alter the oxidation kinetics of the soot. These results can reasonably give the baseline result of the soot oxidation kinetics, more specifically the activation energy, to determine the coated fleece’s performance.



(a)



(b)

Figure 4.26 (a) Mass conversion and (b) Arrhenius plot of soot on noncoated fleece.

The activation energy for diesel PM is less than that of CBN330 because diesel PM contains more volatile and easily oxidizing fractions. This difference in ease of oxidation is most clear in **Figure 4.26a** which shows the mass conversions. Every mass conversion line from the diesel PM oxidation is in a grouping and close to each other and there is a significant gap between this group and the group from the CBN330 oxidation.

4.4.2 With Coating

4.4.2.1 Model Soot

Next, the coated metal fleece was then analyzed by loading the coated and non-coated fleece with CBN330, denoted by cCB and nCB, respectively. This would allow an analysis of the catalyst coating's ability to oxidize a more graphitic or ordered soot. The isothermal temperatures used here were the same for all cases to allow a direct

This material is reserved for educational use only, not allowed for commercial use.

comparison. **Figure 4.27a** shows the mass conversions of cCB and nCB. This was converted into the Arrhenius graph in **Figure 4.27b** for the activation energies.

It should be noted that although the mass conversion curves seemed similar, almost every point in the Arrhenius graph is significantly different between the non-coated and coated cases. It is clear that the thin film catalyst on the fleece is able to change the oxidation behavior in each temperature.

The activation energies were calculated to be 167 kJ/mol for nCB and 138 kJ/mol for cCB. This is a decrease in activation energy of 17%. This reduction clearly shows that the catalyst is able to and can reduce the activation energy for the more difficult to oxidize graphitic soot.

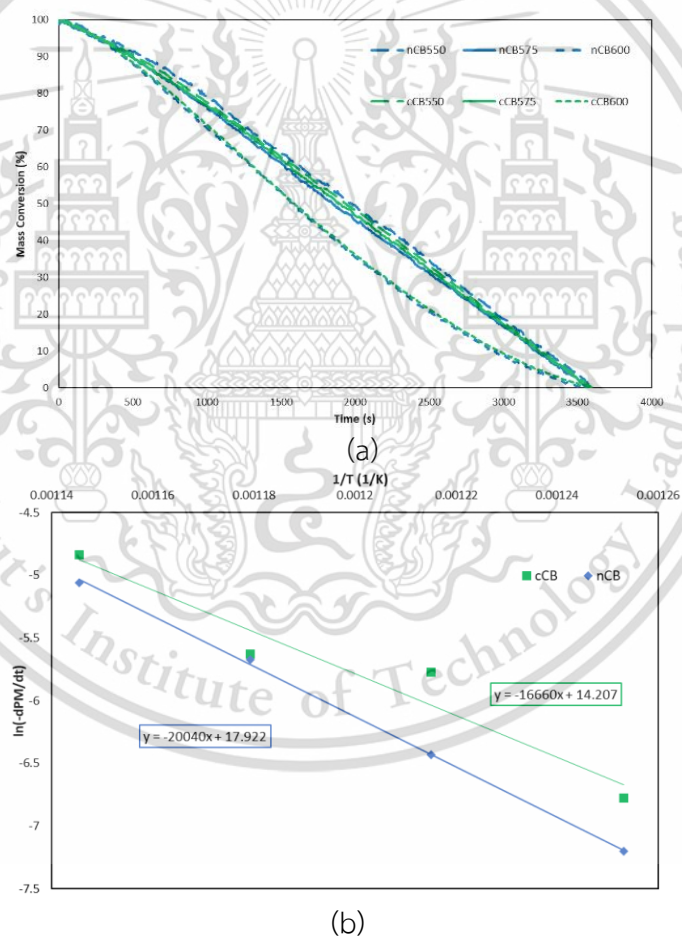


Figure 4.27 (a) Mass conversion and (b) Arrhenius plot of model soot on coated and noncoated metal fleece.

4.4.2.2 Diesel PM

Finally, diesel PM was oxidized on the non-coated, denoted by nDDI, and coated metal fleece, denoted by cDDI, using the same conditions as before. This is the most relevant to real life applications as this would directly investigate the performance of the catalyst in its intended application: to oxidize engine-borne PM. The results of here would also show the performance of the thin film catalyst on the oxidation of amorphous PM as well.

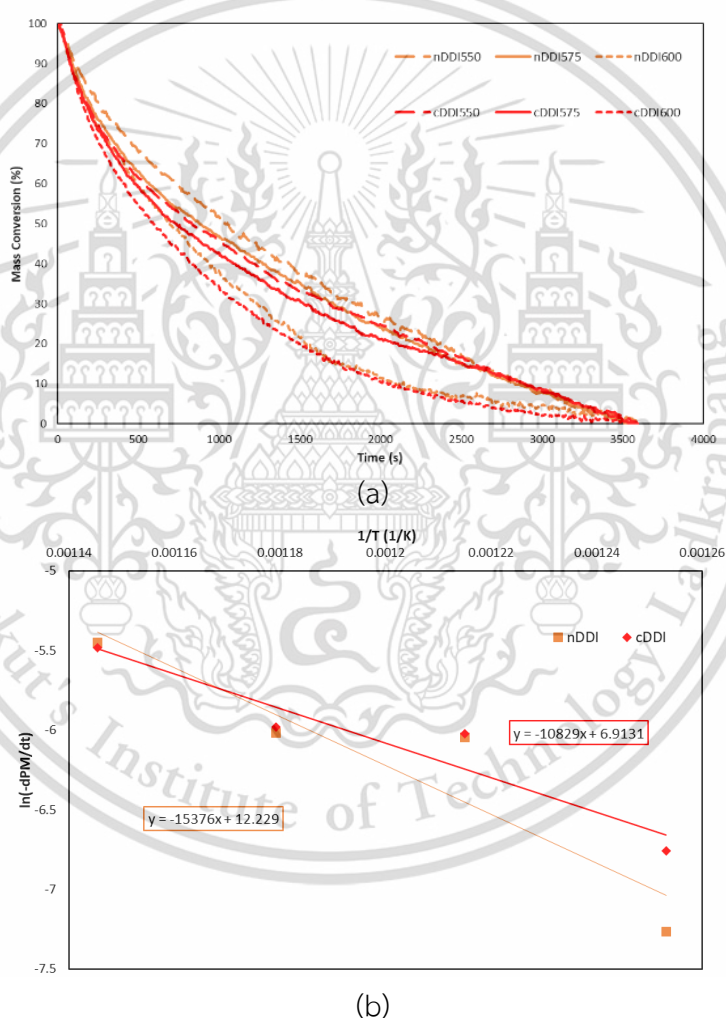
Figure 4.28a shows the mass conversions of nDDI and cDDI. Although at first glance, the mass conversion curves seem quite similar between nDDI and cDDI cases, there is an obvious difference in the slopes. The cDDI cases have steeper slopes compared to the nDDI cases. This is elaborated on by the Arrhenius graph in **Figure 4.28b**. This graph also gave the activation energies of 128 kJ/mol for nDDI and 90 kJ/mol for cDDI. The coating resulted in a 30% reduction in activation energy. This is the case despite CeO₂ is usually not the sole or main catalyst but rather a supporting catalyst for its ability to adsorb O₂ and NO₂.

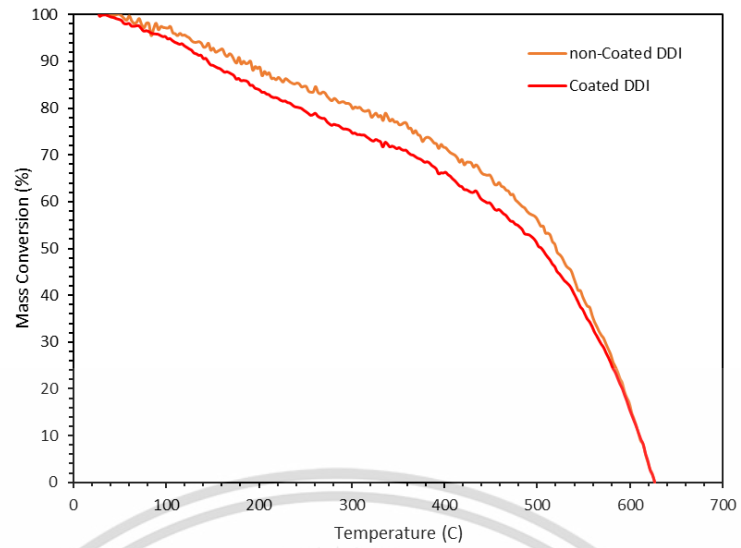
When inspecting **Figure 4.28b** in more detail, it can be seen that the points in the graph that correspond to 550, 575, and 600°C are quite similar for the nDDI and cDDI. The most significant difference in these cases is the right most or lowest temperature oxidation: 525°C. This is because a purpose of a given catalyst is to promote reactions at lower temperatures. This is clearly accomplished by the thin film catalyst here. Another explanation for the similarity for the higher temperatures is that the hydrocarbons and carbonaceous soot are being oxidized simultaneously, which can dampen the calculated effect of the catalyst on the carbonaceous soot. The hydrocarbon oxidation is quite significant when comparing the initial oxidation in nDDI and nCB. Another note is that although the points in **Figure 4.28b** are quite similar between nDDI and cDDI and it may seem that without the lowest temperature, the conclusions would be different, cDDI would still produce a lower slope or lower activation energy without the lowest temperature.

To observe the impact of the coating in the oxidation behavior and not just the kinetics, a non-isothermal mass conversion was done as seen in **Figure 4.28c**. The mass loss before 100°C was from the PM moisture evaporation. After this, the mass loss

curves are obviously more significant as the hydrocarbons are oxidized. The final and largest mass loss comes after 500°C when the carbon crystallites are oxidized.

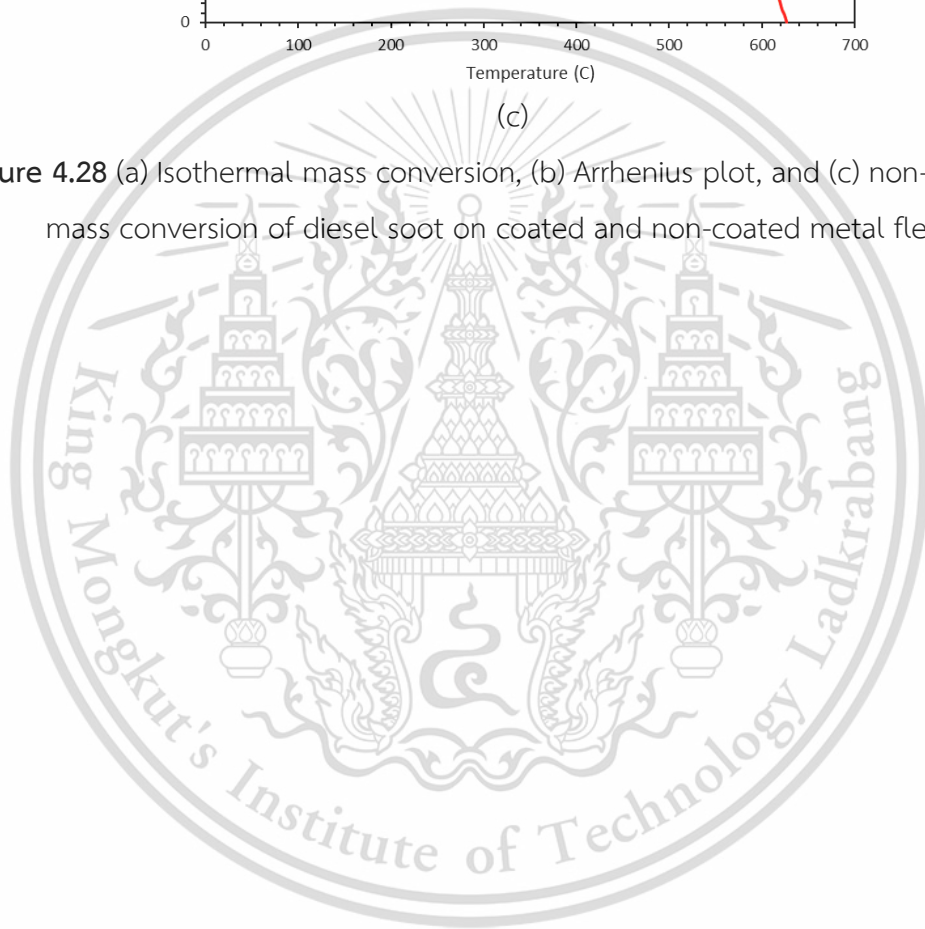
From the significant gap before 500°C, the catalyst coating shows that it allows faster hydrocarbon oxidation. The shift to carbon oxidation for cDDI also occurs before the carbon oxidation for nDDI. However, after around 550°C, it is almost impossible to differentiate between the two as the catalyst's effect seems to reach its limit. This phenomenon of the highest temperature being similar between the cDDI and nDDI supports the conclusions from the difference in **Figure 4.28b**.





(c)

Figure 4.28 (a) Isothermal mass conversion, (b) Arrhenius plot, and (c) non-isothermal mass conversion of diesel soot on coated and non-coated metal fleece.



CHAPTER 5

CONCLUSIONS AND DISCUSSION

5.1. Metallic Microfiber Partial Flow Diesel Particulate Filter

This research analyzed the metal fleece from the metallic microfiber partial flow diesel particulate filter in terms of microstructure, chemical composition, soot trapping, catalyst coating, and oxidation of soot. The metal fleece was the focus of the first part of research to investigate the most important component in the metallic microfiber partial flow diesel particulate filter. The conclusions from the microstructure analysis of the metal fleece were that the metal fibers that make up the metal fleece was covered by grains on the surface in a lengthwise linear manner. These metal fibers as well as the metal flow guide foils, which also make up the P-DPF, were then analyzed for its elemental composition with EDS. The results pointed at the material of both the metal fleece and the metal foil being stainless steel alloys which consist of Fe, Cr, Al, and some C.

Real engine exhaust was then used to simulate the trapping that would occur in the regular and real usage of the metal fleece in the P-DPF. This soot trapping was observed using SEM to show that the PM seemed to grow on the previously mentioned grains instead of the smooth metal surface. Further trapping showed that a dendritic formation was formed by the PM particles. The conditions that would be used to later oxidize the PM were also compared to this as the PM needed to be consistently loaded on the metal fleece to analyze the oxidation kinetics. The comparison showed that the manually loaded PM were in dense clumps instead of the dendritic formation. This may affect inhibit the interaction between gases and the PM.

Nonetheless, the metal fleece was also coated by a catalyst to potentially reduce the energy required to oxidize PM. A ceria catalyst was used with a PVD method known as Radio Frequency Sputtering. This would allow well controlled thicknesses and a thin film coating of approximately 300nm was achieved. This coating was also analyzed with XRD and SEM to determine the coating quality. XRD showed that the chemical composition was indeed ceria. SEM revealed the coating was dense and the bonding to the metal fibers were excellent to the extent that they did not flake off even when it underwent high stresses.

This material is reserved for educational use only, not allowed for commercial use.

Next this coating was tested with TGA to determine the performance of the catalyst. This would be compared to the uncoated fleece. Both model PM and real diesel PM would also be used here to compare the effect of the soot nanostructure as well as to see how the relevant PM would react. The catalyst coating was able to reduce the activation energy for the model soot by 17% from 167 kJ/mol to 138 kJ/mol. The catalyst coating also reduced the activation energy for the diesel PM by 30% from 128 kJ/mol to 90 kJ/mol. The method to load the soot was also compared to literature, which uses sole powder methods, and found the results to be similar when using the uncoated metal fleece.

5.2. How P-DPF effects Diesel PM

This research also investigated how PM was affected by an exhaust after-treatment system consisting of a diesel oxidation catalyst and P-DPF. This was done by analyzing the chemical composition, morphology, and nanostructure of PM from before the DOC, after the DOC, and after the P-DPF. The elemental composition was first analyzed with EDS and revealed that PM had trace elements from the engine oil before entering the exhaust after-treatment system. These trace elements were then reduced by the DOC. There were then little to no other elements also detected in the post-P-DPF PM. Overall, this analysis showed that the after-treatment system did not leak harmful elements into the PM.

Next, the morphology was investigated using TEM and nanoparticle size analyzer. The nanoparticle size analyzer gave the agglomerate size distributions for the PM. The TEM allowed measurements of the single primary particle sizes which were made into a size distribution. Both methods revealed that the PM increased in size as it travelled down the after-treatment system. An interesting note was the nanoparticle size analyzer also detected a peak in the primary particle size which suggested fragmentation.

To better understand this behavior, the nanostructure of the PM was analyzed by TEM, XRD, and RS. The high magnification TEM images hinted that partial oxidation did occur due to the change in the nanostructure. As such, all three methods concluded that there was a decrease of graphitization and the crystallite sizes decreased along the after-treatment system. This was nonconventional as usually soot oxidation

This material is reserved for educational use only, not allowed for commercial use.

increases the degree of graphitization because the amorphous carbon was easiest to oxidize. An explanation of this duality of decreasing graphitization and increasing size is that the simultaneous trapping and oxidation mechanism of the P-DPF allows both processes to occur. The relatively low temperatures in the P-DPF paired with the NO_x environment would promote surface oxidation while the continuous partial trapping and fragmentation from said oxidation would grow the size of both the primary particles and agglomerates by interception.

This was supported by measuring the opacity, temperature, CO₂, NO, and O₂ of the gas in the three stages of the exhaust after-treatment system. The opacity shows that PM is reduced by the DOC by oxidation and by the P-DPF by trapping. The CO₂, NO, and O₂ show that the carbonaceous PM in the P-DPF is passively oxidized by NO₂ and O₂.

The results from this research can provide new methods and perspectives for PM reduction as PM and how it is affected by an exhaust after-treatment system consisting of a DOC and metallic microfiber P-DPF. Future work that could be done could be on converting the thin film catalyst coated metal fleece into a full-scale experimental nano-catalyst coated P-DPF and seeing how the PM is affected by this one stage exhaust after-treatment system.

Chapter 5 Bibliography

- [1] H. Choi, "Technology-push and demand-pull factors in emerging sectors: evidence from the electric vehicle market," *Industry and Innovation*, vol. 25, no. 7, pp. 655-674, 2018.
- [2] G. Conway, A. Joshi, F. Leach, A. García and P. K. Senecal, "A review of current and future powertrain technologies and trends in 2020," *Transportation Engineering*, vol. 5, p. 100080, 2021.
- [3] M. Tran, J. D. Bishop, D. Banister and M. D. McCulloch, "Realizing the Electric Vehicle Revolution," *Nature Climate Change*, vol. 2, no. 5, pp. 328-333, 2012.
- [4] S. Z. Rajper and J. Albrecht, "Prospects of Electric Vehicles in the Developing Countries: A Literature Review," *Sustainability*, vol. 12, no. 5, 2020.
- [5] A. Karki, S. Phuyal, D. Tuladhar, S. Basnet and B. P. Shrestha, "Status of pure electric vehicle power train technology and future prospects," *Applied System Innovation*, vol. 3, no. 3, p. 35, 2020.
- [6] A. Askin, G. Barter, T. West and D. Manley, "The heavy-duty vehicle future in the United States: A parametric analysis of technology and policy tradeoffs," *Energy Policy*, vol. 81, pp. 1-13, 2015.
- [7] Department of Land Transport, "Annual Report 2020," Ministry of Transport, Bangkok, 2020.
- [8] C. ChooChuay, S. Pongpiachan, D. Tipmanee, O. Suttinun, W. Deelaman, Q. Wang, L. Xing, G. Li, Y. Han, J. Palakun and J. Cao, "Impacts of PM2.5 sources on variations in particulate chemical compounds in ambient air of Bangkok, Thailand," *Atmospheric Pollution Research*, vol. 11, no. 9, pp. 1657-1667, 2020.
- [9] N. Englert, "Fine Particles and Human Health - A Review of Epidemiological Studies," *Toxicology Letters*, vol. 1, no. 3, pp. 235-242, 2004.
- [10] S. Steiner, C. Bisig, A. Petri-Fink and B. Rothen-Rutishauser, "Diesel exhaust: current knowledge of adverse effects and underlying cellular mechanisms," *Archives of toxicology*, vol. 90, no. 7, pp. 1541--1553, 2016.
- [11] M. Williams and R. Minjares, "A Technical Summary of Euro 6 Vehicle Emission Standards," International Council on Clean Transportation, 2016.

- [12] S. Mohankumar and P. Senthilkumar, "Particulate matter formation and its control methodologies for diesel engine: A comprehensive review," *Renewable and Sustainable Energy Reviews*, vol. 80, pp. 1227-1238, 2017.
- [13] P. Karin, H. Oki, K. Hanamura and C. Charoenphonphanich, "Nanostructures and Oxidation Kinetics of Diesel Particulate Matters," *Journal of Research and Applications in Mechanical Engineering*, vol. 1, no. 2, pp. 3-8, 2012.
- [14] V. Fernandez-Alos, J. Watson, R. Vander Wal and J. Matthews, "Soot and char molecular representations generated directly from HRTEM lattice fringe images using Fringe3D," *Combustion and Flame*, vol. 158, no. 9, pp. 1807-1813, 2011.
- [15] P. Eastwood, *Particulate Emissions from Vehicles*, Chichester: John Wiley & Sons Ltd, 2008.
- [16] D. B. Kittelson, "Engines and nanoparticles: a review," *Journal of aerosol science*, vol. 29, no. 5-6, pp. 575-588, 1998.
- [17] Y. Hao, C. Gao, S. Deng, M. Yuan, W. Song, Z. Lu and Z. Qiu, "Chemical characterisation of PM_{2.5} emitted from motor vehicles powered by diesel, gasoline, natural gas and methanol fuel.," *Science of The Total Environment*, vol. 674, pp. 128-139, 2019.
- [18] R. L. Vander Wal, A. Yezerets, N. W. Currier, D. H. Kim and C. M. Wang, "HRTEM Study of diesel soot collected from diesel particulate filters," *Carbon*, vol. 45, no. 1, pp. 70-77, 2007.
- [19] B. Vazquez-Santos, E. Geissler, K. Laszlo, J.-N. Rouzaud, A. Martinez-Alonso and J. M. Tascon, "Comparative XRD, Raman, and TEM Study on Graphitization of PBO-Derived Carbon Fibers," *The Journal of Physical Chemistry*, vol. 116, pp. 257-268, 2011.
- [20] L. Pahalagedara, H. Sharma, C.-H. Kuo, S. Dharmarathna, A. Joshi, S. L. Suib and A. B. Mhadeshwar, "Structure and oxidation activity correlations for carbon blacks and diesel soot," *Energy and Fuels*, vol. 26, no. 11, pp. 6757-6764, 2012.
- [21] R. L. Vander Wal, "Soot Nanostructure: Definition, Quantification and Implications," *SAE Technical Paper*, pp. 429-436, 2005.
- [22] H. M. Oo, P. Karin, C. Charoenphonphanich, N. Chollacoop and K. Hanamura, "Physicochemical characterization of direct injection Engines's soot using TEM,

- EDS, X-ray diffraction and TGA," *Journal of the Energy Institute*, vol. 96, pp. 181-191, 2021.
- [23] F. Tuinstra and J. Koenig, "Raman Spectrum of Graphite," *The Journal of Chemical Physics*, vol. 53, p. 1126, 1970.
- [24] A. Cuesta, P. Dhamelincourt, J. Laureyns, A. Martinez-Alonso and J. Tascon, "Comparative performance of X-ray diffraction and Raman microprobe techniques for the study of carbon materials," *Journal of Materials Chemistry*, vol. 8, pp. 2875-2879, 1998.
- [25] A. Raj, G. R. da Silva and S. H. Chung, "Reaction mechanism for the free-edge oxidation of soot by O₂," *Combustion and Flame*, vol. 159, no. 11, pp. 3423-3436, 2012.
- [26] P. Karin and K. Hanamura, "Particulate matter trapping and oxidation on a catalyst membrane," *SAE International Journal of Fuels and Lubricants*, vol. 3, no. 1, pp. 368-379, 2010.
- [27] R. Matarrese, L. Castoldi and L. Lietti, "Oxidation of model soot by NO₂ and O₂ in the presence of water vapor," *Chemical Engineering Science*, vol. 173, pp. 560-569, 2017.
- [28] K. Leistner, A. Nicolle and P. Da Costa, "Detailed kinetic analysis of soot oxidation by NO₂, NO, and NO+ O₂," *The Journal of Physical Chemistry C*, vol. 116, no. 7, pp. 4642-4654, 2012.
- [29] P. Toth, D. Jacobsson, M. Ek and H. Wiinikka, "Real-time, in situ, atomic scale observation of soot oxidation," *Carbon*, vol. 145, pp. 149-160, 2019.
- [30] M. Srilomsak and K. Hanamura, "Time-lapse visualization of shrinking soot in diesel particulate filter during active-regeneration using field emission scanning electron microscopy," *Journal of Microscopy*, vol. 279, no. 2, pp. 85-97, 2020.
- [31] D. Fino, S. Bensaid, M. Piumetti and N. Russo, "A review on the catalytic combustion of soot in Diesel particulate filters for automotive applications: From powder catalysts to structured reactors," *Applied Catalysis A-general*, vol. 509, pp. 75-96, 2016.

- [32] Neha, R. Prasad and S. V. Singh, "A review on catalytic oxidation of soot emitted from diesel fuelled engines," *Journal of environmental chemical engineering*, vol. 8, no. 4, p. 103945, 2020.
- [33] S. Liu, X. Wu, D. Weng and R. Ran, "Ceria-based catalysts for soot oxidation: a review," *Journal of Rare Earths*, vol. 33, no. 6, pp. 567-590, 2015.
- [34] J. Koop and O. Deutschmann, "Detailed surface reaction mechanism for Pt-catalyzed abatement of automotive exhaust gases," *Applied Catalysis B-environmental*, vol. 91, no. 1, pp. 47-58, 2009.
- [35] S. Chatterjee, R. Conway, S. Viswanathan, M. Blomquist, B. Klusener and S. Andersson, "NOx and PM control from heavy duty diesel engines using a combination of low pressure EGT and continuously regenerating diesel particulate filter," *SAE Technical Paper*, pp. 01-0048, 2003.
- [36] B. Guan, R. Zhan, H. Lin and Z. Huang, "Review of the state-of-the-art of exhaust particulate filter technology in internal combustion engines," *Journal of Environmental Management*, pp. 225-258, 2015.
- [37] R. Brück, P. Hirth, M. Reizig, P. Treiber and J. Breuer, "Metal Supported Flow-Through Particulate Trap; a Non-Blocking Solution," *SAE Technical Paper 2001-01-0925*, 2001.
- [38] S. Govender and H. Friedrich, "Monoliths: A Review of the Basics, Preparation Methods and Their Relevance to Oxidation," *Catalysts*, vol. 7, no. 2, p. 62, 2017.
- [39] W. Qing, F. Liu, H. Yao, S. Sun, C. Chen and W. Zhang, "Functional catalytic membrane development: A review of catalyst coating techniques.," *Advances in Colloid and Interface Science*, vol. 282, p. 102207, 2020.
- [40] P.-C. Chen and X. A. Wang, "Cerium Oxide Film Growth Using Radio-Frequency Sputtering Process," *Materials Sciences and Applications*, vol. 11, no. 5, pp. 305-318, 2020.
- [41] X. Wang, H. Wang, Q. Huang, Z. Du, X. Huang, C. Jiang and S. Zhou, "Magnetron sputtering nichrome on fiber fabric to construct microwave-absorbing structure," *Applied Physics A*, vol. 126, p. 863, 2020.

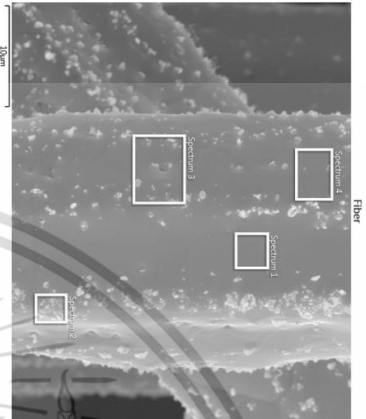
- [42] H.-Y. Lee, S.-I. Kim, Y.-P. Hong, Y.-C. Lee, Y.-H. Park and K.-H. Ko, "Controlling the texture of CeO₂ films by room temperature RF magnetron sputtering," *Surface and Coatings Technology*, vol. 173, pp. 224-228, 2003.
- [43] T. Qiu, J.-G. Yang, X.-J. Bai and Y.-L. Wang, "The preparation of synthetic graphite materials with hierarchical pores from lignite by one-step impregnation and their characterization as dye absorbents," *Royal Society of Chemistry Advances*, vol. 9, p. 12737, 2019.
- [44] D. S. Knight and W. B. White, "Characterization of diamond films by Raman Spectroscopy," *Journal of Materials Research*, vol. 4, no. 02, pp. 385-393, 1988.
- [45] P. Karin, W. Amornprapa, P. Watanawongskorn, E. Saenkhumvong, C. Charoenphonphanich and K. Hanamura, "Effect of soot particle size on four ball metallic wear using electron microscopy image analysis," *International Journal of Automotive Technology*, vol. 21, no. 3, pp. 579-589, 2020.
- [46] R. Francois, "Metal fibers obtained by bundled drawing". US Patent 5071713A, 10 12 1991.
- [47] R. De Bruyne and I. Lefever, "14. Metal Fibers," in *Ullmann's Encyclopedia of Industrial Chemistry*, Wiley-VCH Verlag GmbH, 2000.
- [48] M. T. Yurtcan, "Deposition of grid-like single-crystal Ce₂O₃ thin films on LaAlO₃(100) substrate by pulsed laser deposition," *Journal of Material Science: Material Electron*, vol. 32, pp. 3854-3862, 2021.
- [49] K. Persson, *Materials Data on Ce₂O₃ (SG:206) by Materials Project*, United States, 2016.
- [50] C. Guillen, J. Montero and J. Herrero, "Anatase and rutile TiO₂ thin films prepared by reactive DC sputtering at high deposition rates on glass and flexible polyimide substrates," *Journal of Material Science*, vol. 49, pp. 5035-5042, 2014.
- [51] P. Karin, P. Koko, C. Charoenphonphanich, N. Chollacoop and K. Hanamura, "Physicochemical Characterization of Diesel Engine's Soot and Metal Oxide Ash Nanoparticles Using Electron Microscopy, EDS and TGA," *Emission Control Science and Technology*, vol. 7, no. 2, pp. 91-104, 2021.
- [52] A. K. Neyestanaki, F. Klingstedt, T. Salmi and D. Y. Murzin, "Deactivation of postcombustion catalysts, a review," *Fuel*, vol. 83, pp. 395-408, 2004.

- [53] R. L. Vander Wal, A. J. Tomasek, K. Street, D. R. Hull and W. K. Thompson, "Carbon Nanostructure Examined by Lattice Fringe Analysis of High-Resolution Transmission Electron Microscopy Images," *Applied Spectroscopy*, vol. 58, no. 2, pp. 230-237, 2004.
- [54] Y. Liu, X. Zhang, G. Lyu, Y. Qiao, W. Zhang and C. Song, "Effect of the oxidation-induced fragmentation of primary particles on soot oxidation reactivity," *Combustion and Flame*, vol. 240, p. 112026, 2022.
- [55] A. Liati, P. D. Eggenschwiler, D. Schreiber, V. Zelenay and M. Ammann, "Variations in diesel soot reactivity along the exhaust after-treatment system, based on the morphology and nanostructure of primary soot particles," *Combustion and Flame*, vol. 160, pp. 671-681, 2013.
- [56] S. Rothenbacher, A. Messerer and G. Kasper, "Fragmentation and bond strength of airborne diesel soot agglomerates," *Particle and Fibre Toxicology*, vol. 5, no. 9, 2008.
- [57] M. Singh, M. Srilomsak, Y. Wang, K. Hanamura and R. Vander Wal, "Nanostructure changes in diesel soot during NO₂-O₂ oxidation under diesel particulate filter-like conditions toward filter regeneration," *International Journal of Engine Research*, vol. 20, no. 8, pp. 953-966, 2019.
- [58] A. Strzelec, R. L. Vander Wal, T. N. Thompson, T. J. Toops and C. S. Daw, "NO₂ oxidation reactivity and burning mode of diesel particulates," *Topics in Catalysis*, vol. 59, no. 8, pp. 686-694, 2016.
- [59] P. Toth, D. Jacobsson, M. Ek and H. Wiinikka, "Real-time, in situ, atomic scale observation of soot oxidation," *Carbon*, vol. 145, pp. 149-160, 2019.
- [60] M. Sirignano, H. Ghiassi, A. D'Anna and J. S. Lighty, "Temperature and oxygen effects on oxidation-induced fragmentation of soot particles," *Combustion and Flame*, vol. 171, pp. 15-26, 2016.

Chapter 6 APPENDIX A :
TEST REPORTS

Project 1

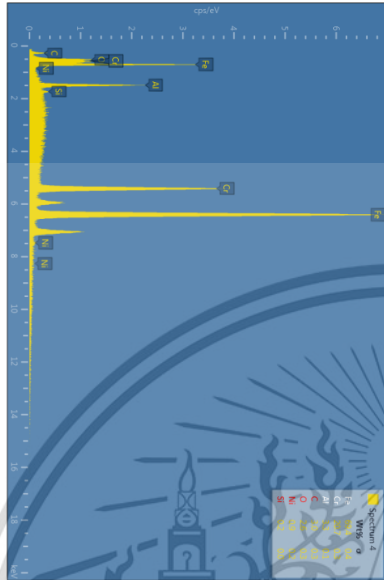
9/16/2020



Project 1

9/16/2020

Label:	Spectrum 4
Source:	Acquired
Created:	9/16/2020 5:15:10 PM
Livetime:	30.0s
Process Time:	6
Accelerating Voltage:	15.00kV
Magnification:	3000 x
Working Distance:	11.7mm
Specimen Tilt (degrees):	0.0
Elevation (degrees):	35.0
Azimuth (degrees):	0.0
Number Of Channels:	2048
Energy Range (keV):	20 keV
Energy per Channel (eV):	10.0eV
Detector Type id:	28
Detector Type:	K-Max
Window Type:	SATW
Pulse Pile Up Correction:	Succeeded
Primary Detector:	Horiba
Primary Detector Serial Number:	70527-X050



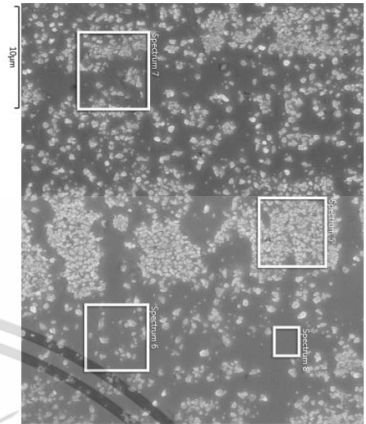
Project 1

9/16/2020

A-1 Test report of EDS on metal fleece.

Project 1

9/16/2020

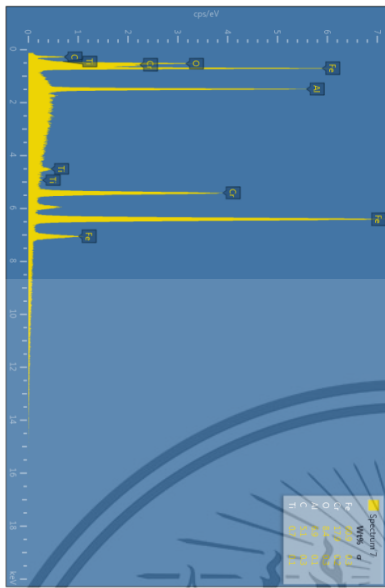


Project 1

9/16/2020

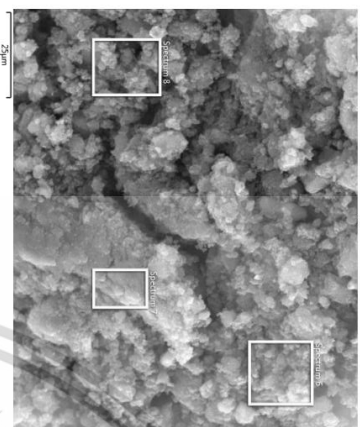
Project 1

9/16/2020

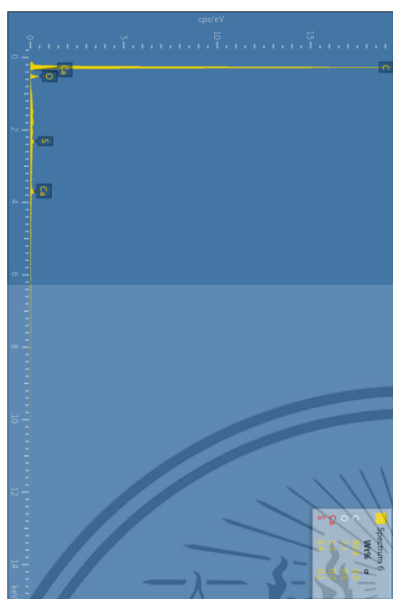


Label:	Spectrum 8
Source:	Acquired
Created:	9/16/2020 5:22:06 PM
Livetime:	50.0s
Process Time:	6
Accelerating Voltage:	15.00kV
Magnification:	3000 x
Working Distance:	12.0mm
Specimen Tilt (degrees):	0.0
Elevation (degrees):	35.0
Asimuth (degrees):	0.0
Number Of Channels:	2048
Energy Range (keV):	20 keV
Energy per Channel (eV):	10.0eV
Detector Type Id:	28
Detector Type:	X-Max
Window Type:	SATW
Pulse Pile Up Correction:	Succeeded
Primary Detector:	Horiba
Primary Detector Serial Number:	70527-X050

A-2 Test report of EDS on metal flow guides.

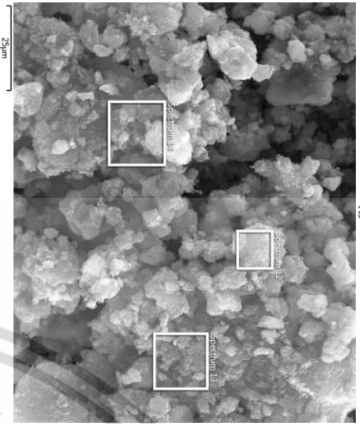


A1



Label:	Spectrum 8
Source:	Acquired
Created:	8/11/2021 11:02:04 AM
Livetime:	30.05
Process Time:	6
Accelerating Voltage:	15.00kV
Magnification:	1000 x
Working Distance:	10.8mm
Specimen Tilt (degrees):	0.0
Elevation (degrees):	35.0
Azimuth (degrees):	0.0
Number Of Channels:	2048
Energy Range (keV):	20 keV
Energy per Channel (eV):	10.0eV
Detector Type Id:	28
Detector Type:	X-Max
Window Type:	SATW
Pulse Pile Up Correction:	Disabled
Primary Detector:	Horiba
Primary Detector Serial Number:	70527-X050

A-3 Test report of EDS on pre-DOC PM.



Project 1

Label:	Spectrum 14
Source:	Acquired
Created:	8/11/2021 11:17:40 AM
Livetime:	50.4s
Process Time:	6
Accelerating Voltage:	15.00kV
Magnification:	1000 x
Working Distance:	11.0mm
Specimen Tilt (degrees):	0.0
Elevation (degrees):	35.0
Azimuth (degrees):	0.0
Number Of Channels:	2048
Energy Range (keV):	20 keV
Energy per Channel (eV):	10.0eV
Detector Type Id:	28
Detector Type:	X-Max
Window Type:	SATW
Pulse Pile Up Correction:	Disabled
Primary Detector:	Horiba
Primary Detector Serial Number:	70527-X050



Project 1

A-5 Test report of EDS on post-P-DPF PM.

NANO PARTICLE ANALYZER
BRAND : HORIBA MODEL:SZ-100V2

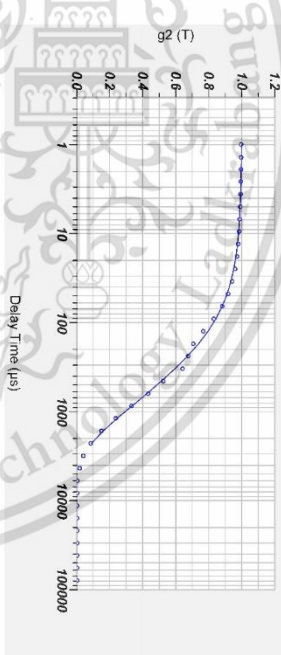
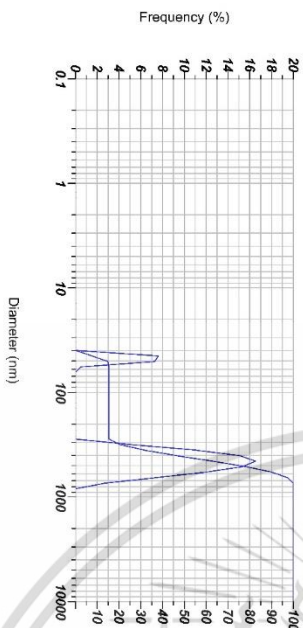
Measurement Results

Date : 27/08/2021 (Fri) 11:46:59
 Test or Assay Number : 64-U/9-3905
 Sample Name : 20210827_Z100039_A3 Post-DPF DDI Spot
 Measurement Type : Particle Size
 Scattering Angle : 90
 Temperature of the Holder : 25.0 °C
 Dispersion Medium Name : Ethanol
 Dispersion Medium Viscosity : 1.085 mPa·s
 Transmission Intensity before Meas. : 24941
 Distribution Form : Standard
 Polydispersity : Polydisperse
 Representation of Result : Scattering Light Intensity
 Count Rate : 2965 KCPS

Calculation Results

Peak No.	S.F.Area Ratio	Mean	S. D.	Mode
1	0.15	45.0 nm	3.1 nm	44.6 nm
2	0.85	450.1 nm	99.3 nm	428.0 nm
Total	1.00	388.0 nm	172.2 nm	428.0 nm

Z-Average : 260.5 nm
 P1 : 0.693
 Cumulants S. D. : 216.9 nm



Data table size

No.	Diameter	Frequency	Cumulation	No.	Diameter	Frequency	Cumulation	No.	Diameter	Frequency	Cumulation
1	0.34	0.000	0.000	31	13.50	0.000	0.000	61	513.71	15.284	73.310
2	0.36	0.000	0.000	32	14.81	0.000	0.000	62	580.41	17.897	92.207
3	0.38	0.000	0.000	33	16.35	0.000	0.000	63	659.22	20.777	113.000
4	0.45	0.000	0.000	34	18.16	0.000	0.000	64	749.89	24.572	137.500
5	0.62	0.000	0.000	35	21.50	0.000	0.000	65	853.07	29.000	166.500
6	0.62	0.000	0.000	36	24.29	0.000	0.000	66	945.74	34.000	200.500
7	0.70	0.000	0.000	37	27.45	0.000	0.000	67	1068.52	40.000	240.500
8	0.80	0.000	0.000	38	31.01	0.000	0.000	68	1207.24	47.000	287.500
9	0.90	0.000	0.000	39	35.05	0.000	0.000	69	1353.97	55.000	342.500
10	1.00	0.000	0.000	40	39.67	0.000	0.000	70	1519.70	64.000	406.500
11	1.15	0.000	0.000	41	44.42	7.500	7.500	71	1704.10	74.000	480.500
12	1.30	0.000	0.000	42	50.53	7.256	14.756	72	1907.14	85.000	565.500
13	1.47	0.000	0.000	43	57.09	0.488	15.244	73	2129.51	97.000	662.500
14	1.66	0.000	0.000	44	64.50	0.000	15.244	74	2371.05	0.000	770.000
15	1.87	0.000	0.000	45	72.87	0.000	15.244	75	2633.01	0.000	898.000
16	2.11	0.000	0.000	46	82.53	0.000	15.244	76	2915.35	0.000	1038.000
17	2.38	0.000	0.000	47	92.67	0.000	15.244	77	3218.08	0.000	1189.000
18	2.70	0.000	0.000	48	105.16	0.000	15.244	78	3541.31	0.000	1351.000
19	3.05	0.000	0.000	49	118.74	0.000	15.244	79	3885.14	0.000	1524.000
20	3.45	0.000	0.000	50	134.16	0.000	15.244	80	4258.56	0.000	1708.000
21	3.89	0.000	0.000	51	151.57	0.000	15.244	81	4661.62	0.000	1903.000
22	4.40	0.000	0.000	52	171.25	0.000	15.244	82	5094.24	0.000	2109.000
23	4.97	0.000	0.000	53	193.48	0.000	15.244	83	5556.52	0.000	2327.000
24	5.61	0.000	0.000	54	218.86	0.000	15.244	84	6048.45	0.000	2557.000
25	6.34	0.000	0.000	55	246.95	0.000	15.244	85	6570.02	0.000	2800.000
26	7.17	0.000	0.000	56	279.04	0.000	15.244	86	7121.23	0.000	3057.000
27	8.10	0.000	0.000	57	315.27	5.078	20.322	87	7702.06	0.000	3328.000
28	9.15	0.000	0.000	58	356.20	10.988	31.310	88	8312.52	0.000	3613.000
29	10.34	0.000	0.000	59	402.44	18.105	49.415	89	8952.62	0.000	3913.000
30	11.68	0.000	0.000	60	454.69	18.522	67.937	90	9622.24	0.000	4227.000

A-6 Test report of nanoparticle size analyzer on pre-DOC PM.

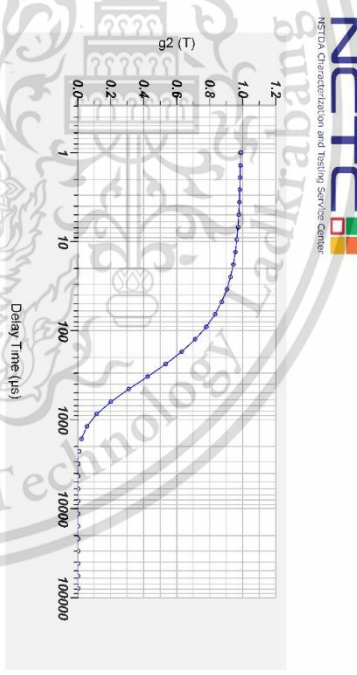
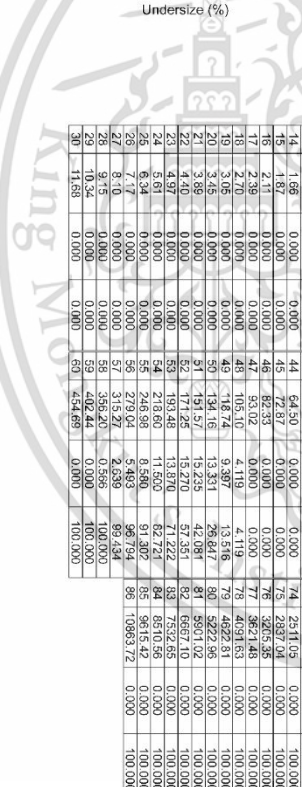
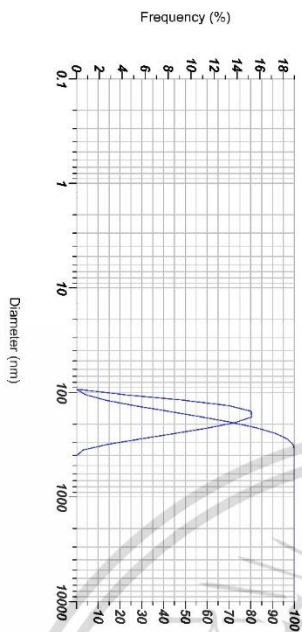
NANO PARTICLE ANALYZER
 BRAND : HORIBA MODEL:SZ-100V2

Measurement Results

Date : 01/09/2021 (Wed) 14:31:11
 Test or Assay Number : 64-U19-3974
 Sample Name : 20210901_Z100040_A1
 Measurement Type : Particle Size
 Scattering Angle : 90
 Temperature of the Holder : 25.0 °C
 Dispersion Medium Name : Ethanol
 Dispersion Medium Viscosity : 1.083 mPa·s
 Transmission Intensity before Meas. : 10061
 Distribution Form : Standard
 Distribution Form(Dispersity) : Polydisperse
 Representation of Result : Scattering Light Intensity
 Count Rate : 1190 KCPS

Calculation Results

Peak No. S.F.Area Ratio Mean S. D. Mode
 1 1.00 --- nm --- nm --- nm
 2 --- --- nm --- nm --- nm
 3 --- --- nm --- nm --- nm
 Total 1.00 170.7 nm 49.8 nm 160.2 nm
 Z-Average : 158.5 nm
 PI : 0.057
 Cumulants S. D. : 37.8 nm



Data table size

No.	Diameter	Frequency	Cumulation	No.	Diameter	Frequency	Cumulation	No.	Diameter	Frequency	Cumulation
1	0.34	0.000	0.000	31	13.20	0.000	0.000	61	513.7	0.000	100.000
2	0.38	0.000	0.000	32	14.81	0.000	0.000	62	580.4	0.000	100.000
3	0.43	0.000	0.000	33	16.84	0.000	0.000	63	656.76	0.000	100.000
4	0.48	0.000	0.000	34	19.38	0.000	0.000	64	744.0	0.000	100.000
5	0.55	0.000	0.000	35	21.80	0.000	0.000	65	832.07	0.000	100.000
6	0.62	0.000	0.000	36	24.99	0.000	0.000	66	945.74	0.000	100.000
7	0.70	0.000	0.000	37	27.45	0.000	0.000	67	1068.52	0.000	100.000
8	0.80	0.000	0.000	38	31.01	0.000	0.000	68	1207.24	0.000	100.000
9	0.90	0.000	0.000	39	35.03	0.000	0.000	69	1363.97	0.000	100.000
10	1.02	0.000	0.000	40	39.56	0.000	0.000	70	1541.04	0.000	100.000
11	1.16	0.000	0.000	41	44.65	0.000	0.000	71	1741.46	0.000	100.000
12	1.30	0.000	0.000	42	50.33	0.000	0.000	72	1967.14	0.000	100.000
13	1.47	0.000	0.000	43	57.09	0.000	0.000	73	2222.51	0.000	100.000
14	1.68	0.000	0.000	44	64.50	0.000	0.000	74	2511.09	0.000	100.000
15	1.87	0.000	0.000	45	72.87	0.000	0.000	75	2837.04	0.000	100.000
16	2.11	0.000	0.000	46	82.33	0.000	0.000	76	3205.38	0.000	100.000
17	2.39	0.000	0.000	47	93.02	0.000	0.000	77	3621.48	0.000	100.000
18	2.70	0.000	0.000	48	105.10	0.000	0.000	78	4091.40	0.000	100.000
19	3.05	0.000	0.000	49	118.74	0.000	0.000	79	4622.81	0.000	100.000
20	3.45	0.000	0.000	50	134.16	0.000	0.000	80	5222.56	0.000	100.000
21	3.89	0.000	0.000	51	151.57	0.000	0.000	81	5901.02	0.000	100.000
22	4.40	0.000	0.000	52	171.25	0.000	0.000	82	6667.10	0.000	100.000
23	4.97	0.000	0.000	53	193.48	0.000	0.000	83	7522.65	0.000	100.000
24	5.61	0.000	0.000	54	218.66	0.000	0.000	84	8478.55	0.000	100.000
25	6.32	0.000	0.000	55	247.40	0.000	0.000	85	9545.45	0.000	100.000
26	7.14	0.000	0.000	56	279.94	0.000	0.000	86	10734.99	0.000	100.000
27	8.08	0.000	0.000	57	315.27	0.000	0.000	87	12058.72	0.000	100.000
28	9.15	0.000	0.000	58	356.20	0.000	0.000	88	13528.25	0.000	100.000
29	10.34	0.000	0.000	59	402.44	0.000	0.000	89	15155.15	0.000	100.000
30	11.68	0.000	0.000	60	454.89	0.000	0.000	90	16950.93	0.000	100.000

A-7 Test report of nanoparticle size analyzer on post-DOC PM.

NANO PARTICLE ANALYZER
 BRAND : HORIBA MODEL:SZ-100VZ

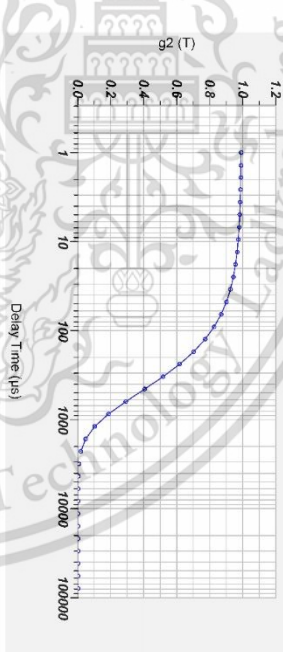
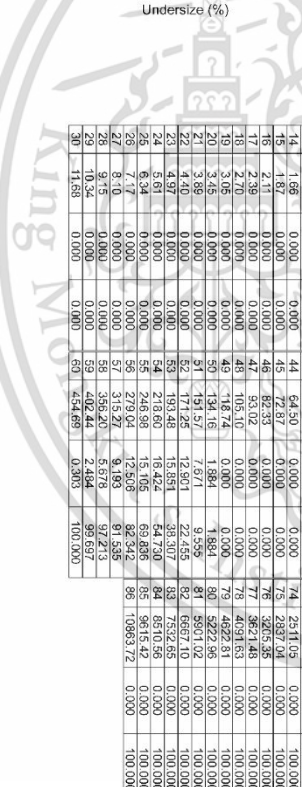
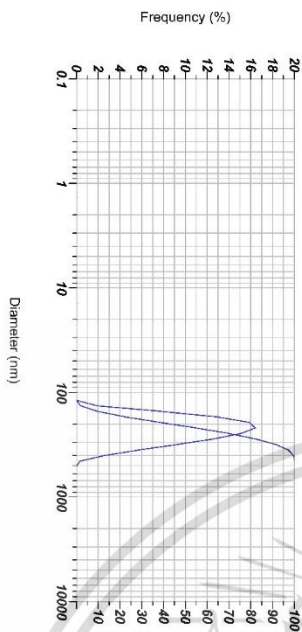
Measurement Results

Date : 01/09/2021 (Wed) 11:51:09
 Test or Assay Number : 64-U19-3974
 Sample Name : 20210901_Z100041_A2
 Measurement Type : Particle Size
 Scattering Angle : 90
 Temperature of the Holder : 25.0 °C
 Dispersion Medium Name : Ethanol
 Transmission Medium Viscosity : 1.084 mPa·s
 Distribution Intensity before Meas. : 8832
 Distribution Form : Standard
 Distribution Form(Dispersity) : Polydisperse
 Representation of Result : Scattering Light Intensity
 Count Rate : 1368 KCPS

Calculation Results

Peak No.	S.P.Area Ratio	Mean	S. D.	Mode
1	1.00	221.7 nm	60.2 nm	205.1 nm
2	---	---	---	---
3	---	---	---	---
Total	1.00	221.7 nm	60.2 nm	205.1 nm

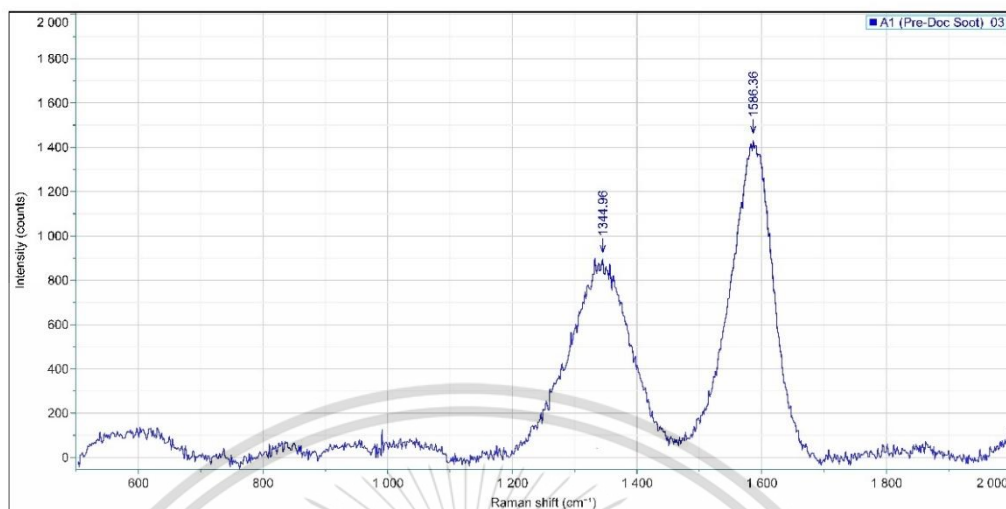
Z-Average : 205.8 nm
 Z-Average : 0.095
 Cumulants S. D. : 63.3 nm



Data table size

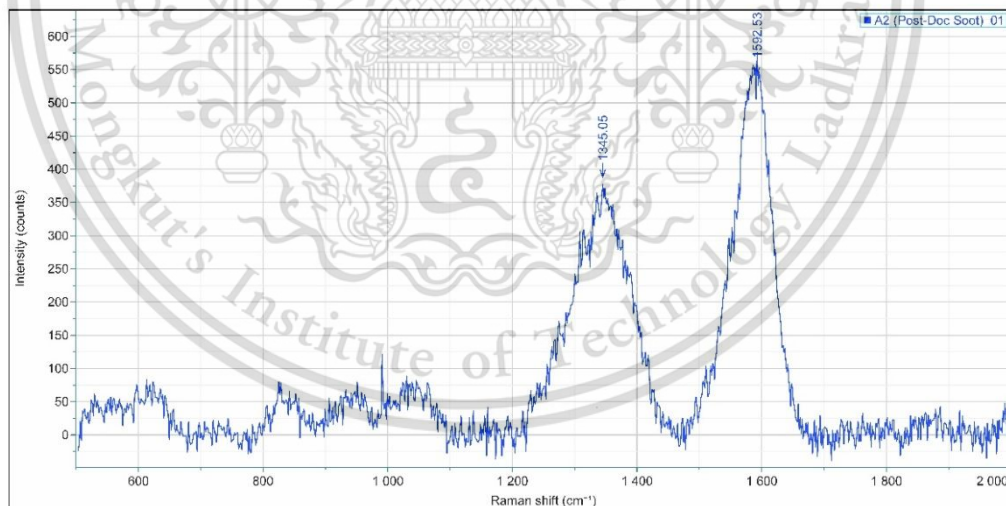
No.	Diameter	Frequency	Cumulation	No.	Diameter	Frequency	Cumulation	No.	Diameter	Frequency	Cumulation
1	0.34	0.000	0.000	31	13.20	0.000	0.000	61	513.7	0.000	100.000
2	0.36	0.000	0.000	32	14.81	0.000	0.000	62	580.4	0.000	100.000
3	0.43	0.000	0.000	33	16.84	0.000	0.000	63	656.76	0.000	100.000
4	0.45	0.000	0.000	34	18.60	0.000	0.000	64	743.90	0.000	100.000
5	0.52	0.000	0.000	35	21.60	0.000	0.000	65	832.07	0.000	100.000
6	0.62	0.000	0.000	36	24.99	0.000	0.000	66	945.74	0.000	100.000
7	0.70	0.000	0.000	37	27.45	0.000	0.000	67	1068.52	0.000	100.000
8	0.80	0.000	0.000	38	31.01	0.000	0.000	68	1207.24	0.000	100.000
9	0.90	0.000	0.000	39	35.03	0.000	0.000	69	1363.97	0.000	100.000
10	1.02	0.000	0.000	40	39.66	0.000	0.000	70	1541.06	0.000	100.000
11	1.12	0.000	0.000	41	44.84	0.000	0.000	71	1741.46	0.000	100.000
12	1.30	0.000	0.000	42	50.53	0.000	0.000	72	1967.14	0.000	100.000
13	1.47	0.000	0.000	43	57.09	0.000	0.000	73	2222.51	0.000	100.000
14	1.68	0.000	0.000	44	64.50	0.000	0.000	74	2511.09	0.000	100.000
15	1.87	0.000	0.000	45	72.87	0.000	0.000	75	2837.04	0.000	100.000
16	2.11	0.000	0.000	46	82.33	0.000	0.000	76	3205.38	0.000	100.000
17	2.39	0.000	0.000	47	93.02	0.000	0.000	77	3621.48	0.000	100.000
18	2.70	0.000	0.000	48	105.00	0.000	0.000	78	4091.00	0.000	100.000
19	3.05	0.000	0.000	49	118.14	0.000	0.000	79	4622.81	0.000	100.000
20	3.45	0.000	0.000	50	134.16	1.884	0.000	80	5222.56	0.000	100.000
21	3.89	0.000	0.000	51	151.57	7.671	9.559	81	5901.02	0.000	100.000
22	4.40	0.000	0.000	52	171.25	12.901	22.455	82	6667.10	0.000	100.000
23	4.97	0.000	0.000	53	193.48	15.851	38.307	83	7522.55	0.000	100.000
24	5.61	0.000	0.000	54	218.66	16.452	54.760	84	8481.59	0.000	100.000
25	6.32	0.000	0.000	55	247.40	15.850	70.610	85	9548.88	0.000	100.000
26	7.12	0.000	0.000	56	279.54	12.508	83.112	86	10728.14	0.000	100.000
27	8.00	0.000	0.000	57	315.27	9.193	91.536	87	12033.53	0.000	100.000
28	9.15	0.000	0.000	58	356.20	5.678	97.273	88	13470.72	0.000	100.000
29	10.34	0.000	0.000	59	402.44	2.484	99.697	89	15044.53	0.000	100.000
30	11.58	0.000	0.000	60	454.89	0.303	100.000	90	16761.00	0.000	100.000

A-8 Test report of nanoparticle size analyzer on post-P-DPF PM.



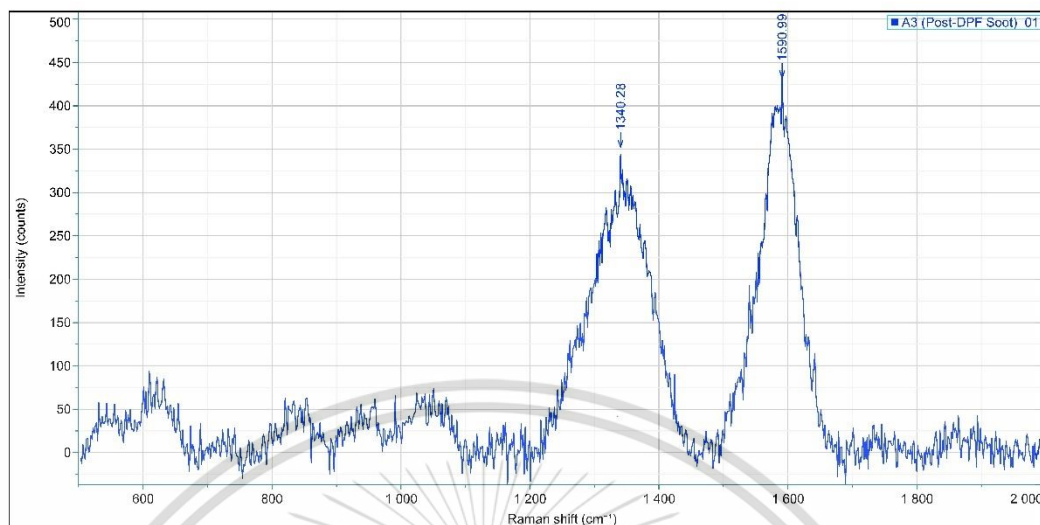
Title	A1 (Pre-Doc Soot)	Instrument	LabRAM HR Evol	Acq. time (s)	10
Accumulations	10	Laser	532nm_Edge	Hole	300.003
Detector	Syncerity OE	Grating	600 (750nm)	ND Filter	10%
Exposition		Objective	x50_VIS	Range (cm ⁻¹)	499...2000

A-9 Test report of Raman Spectroscopy on pre-DOC PM.



Title	A2 (Post-Doc Soot)	Instrument	LabRAM HR Evol	Acq. time (s)	10
Accumulations	10	Laser	532nm_Edge	Hole	300.003
Detector	Syncerity OE	Grating	600 (750nm)	ND Filter	10%
Exposition		Objective	x50_VIS	Range (cm ⁻¹)	499...2000

A-10 Test report of Raman Spectroscopy on post-DOC PM.



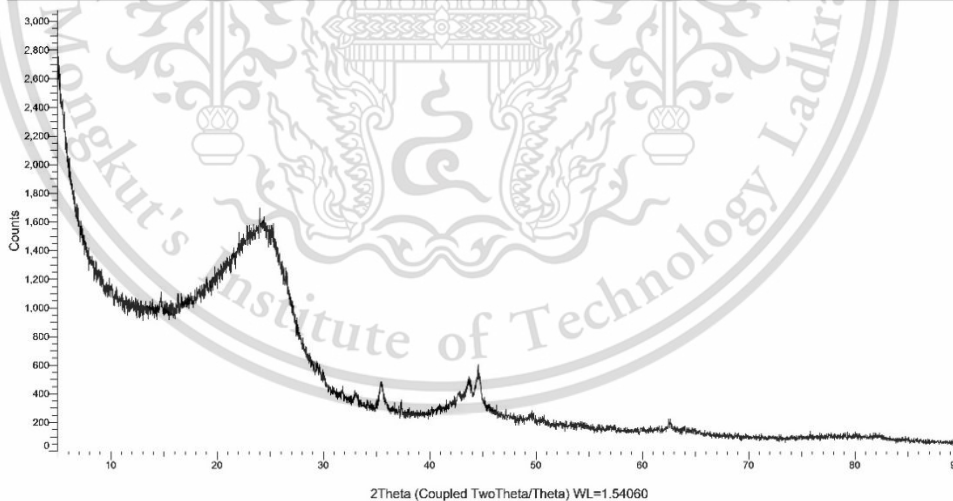
Title	A3 (Post-DPF Soot)	Instrument	LabRAM HR Evol	Acq. time (s)	10
Accumulations	10	Laser	532nm_Edge	Gate	300.003
Detector	Synovity OE	Grating	600 (750nm)	ND Filter	10%
Exposition		Objective	x50_VIS	Range (cm⁻¹)	489...2000

A-11 Test report of Raman Spectroscopy on post-P-DPF PM.

X-RAY DIFFRACTOMETER

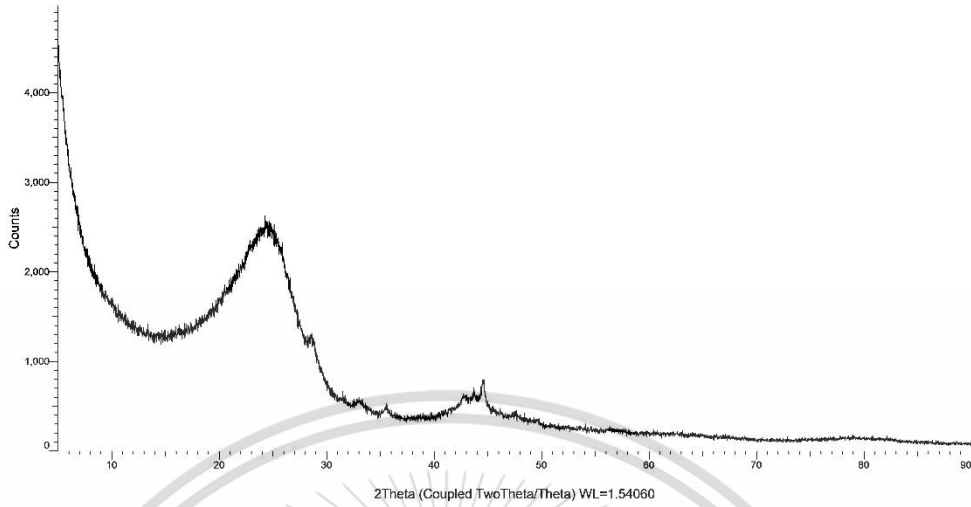
8/11/2021

20210811_2100369_A1(pre-DOC-Soot) (Coupled TwoTheta/Theta)



A-12 Test report of XRD on pre-DOC PM.

20210811_2100370_A2(post-DOC-Soot) (Coupled TwoTheta/Theta)

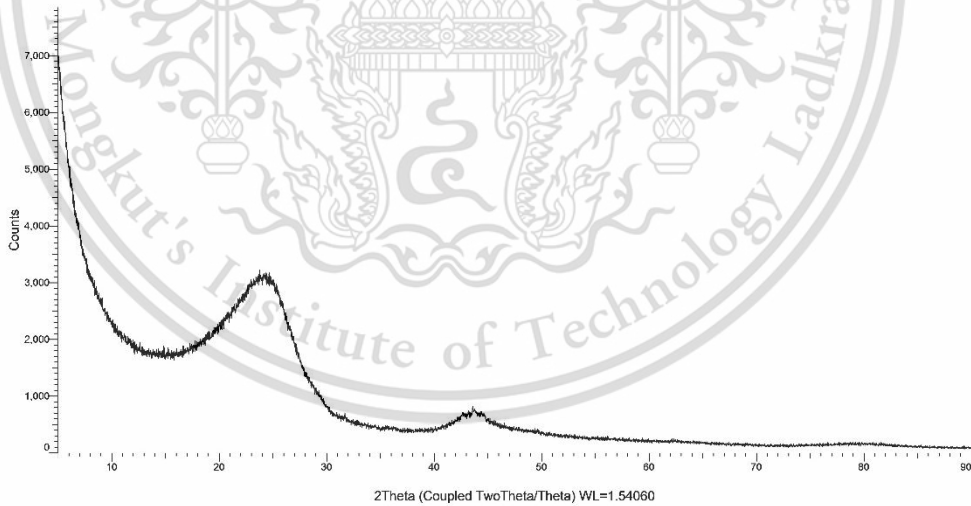


NSTDA Characterization and Testing Service Center



A-13 Test report of XRD on post-DOC PM.

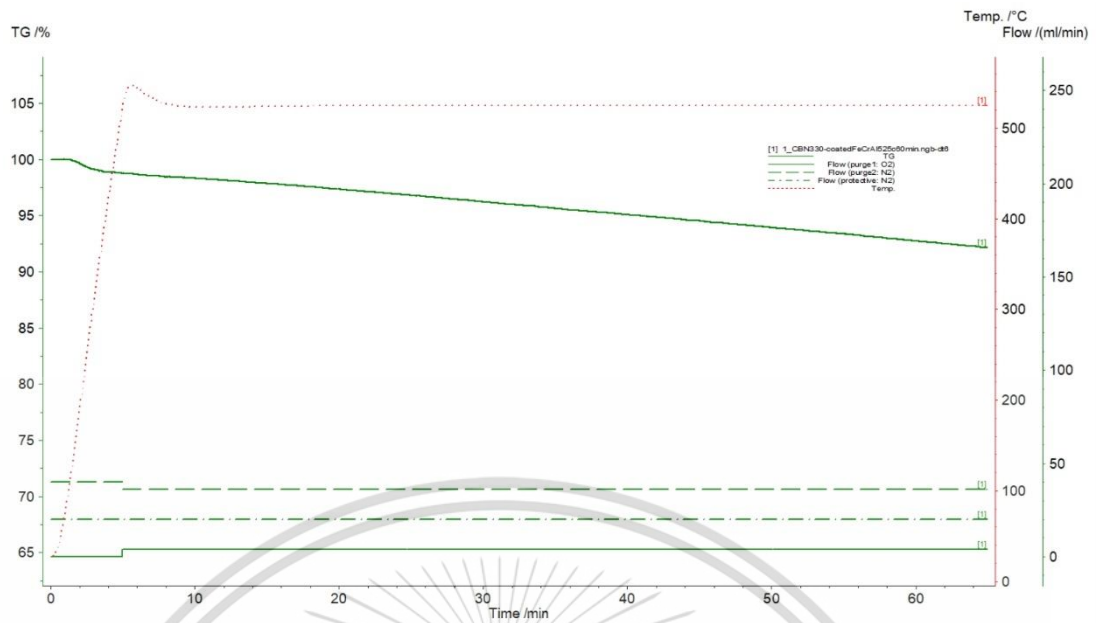
20210811_2100371_A3(post-DPF-Soot) (Coupled TwoTheta/Theta)



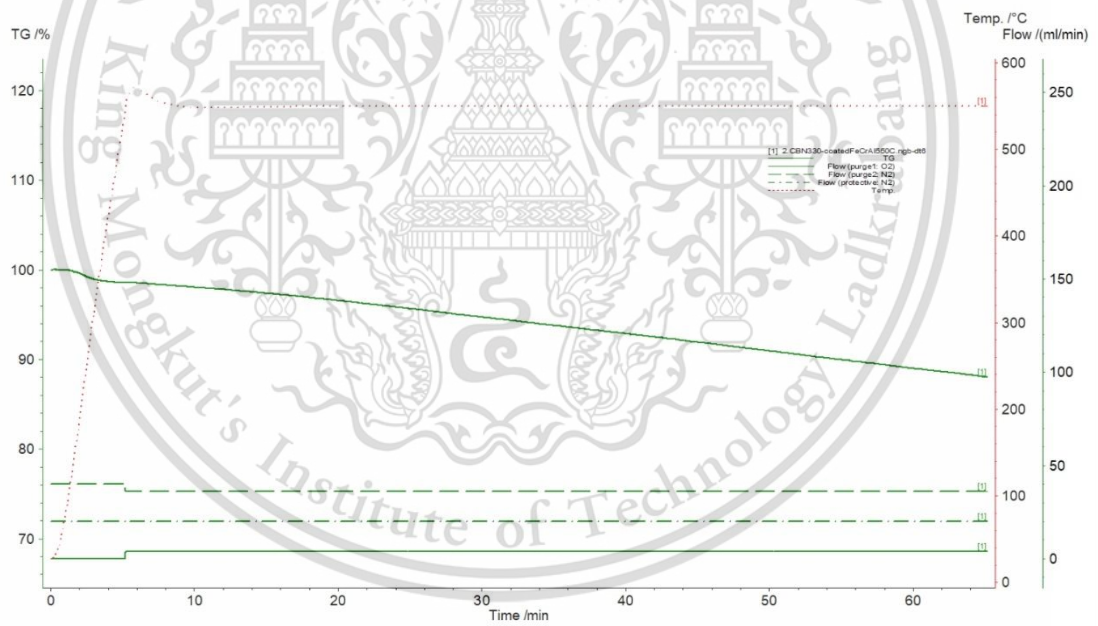
NSTDA Characterization and Testing Service Center



A-14 Test report of XRD on post-P-DPF PM.



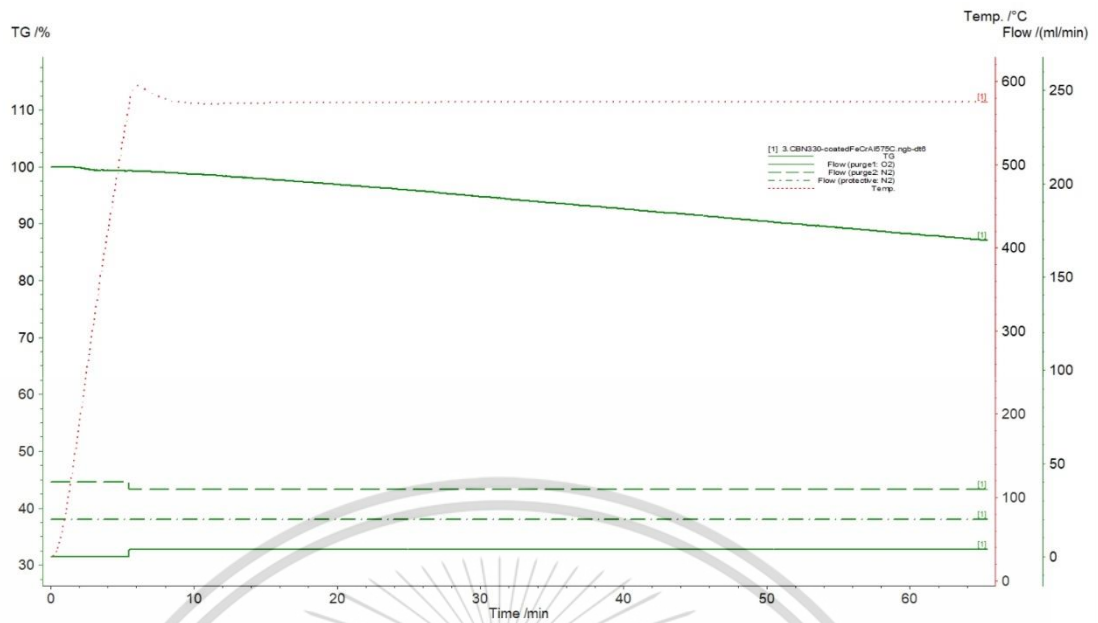
A-15 Test report of TGA cCB 525°C.



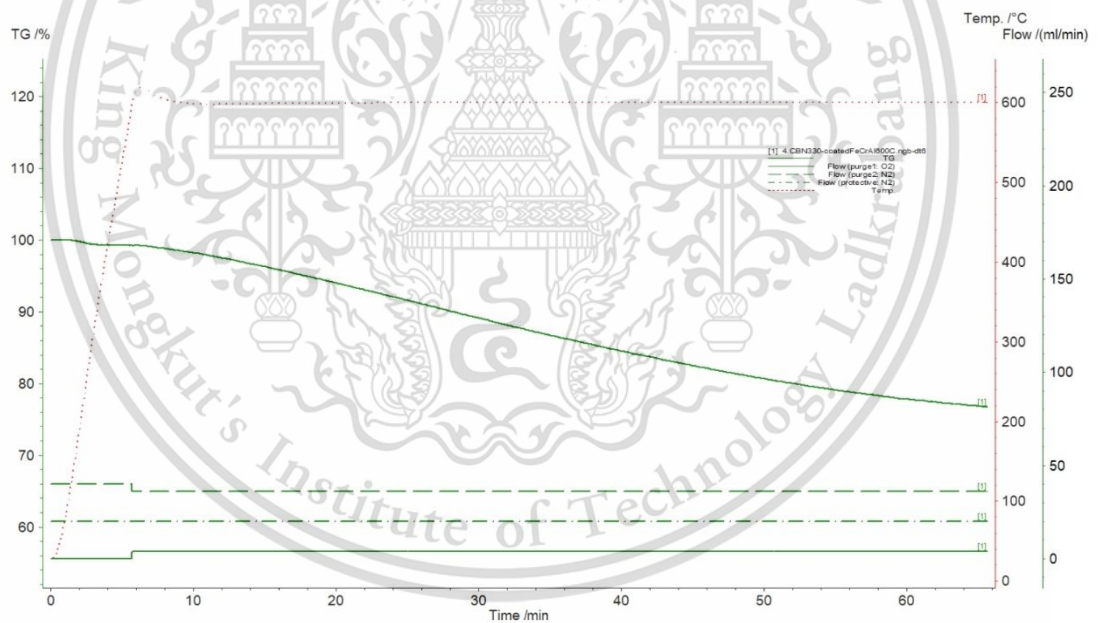
A-16 Test report of TGA cCB 550°C.

This material is reserved for educational use only, not allowed for commercial use.

Forbidden to modify the content, and cite the document when use.



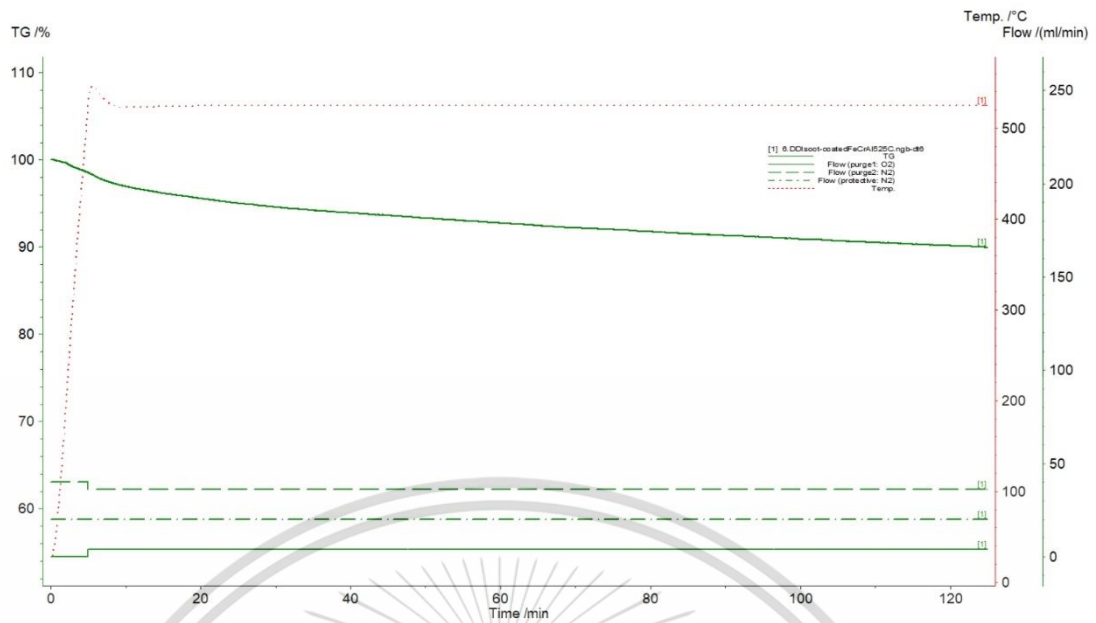
A-17 Test report of TGA cCB 575°C.



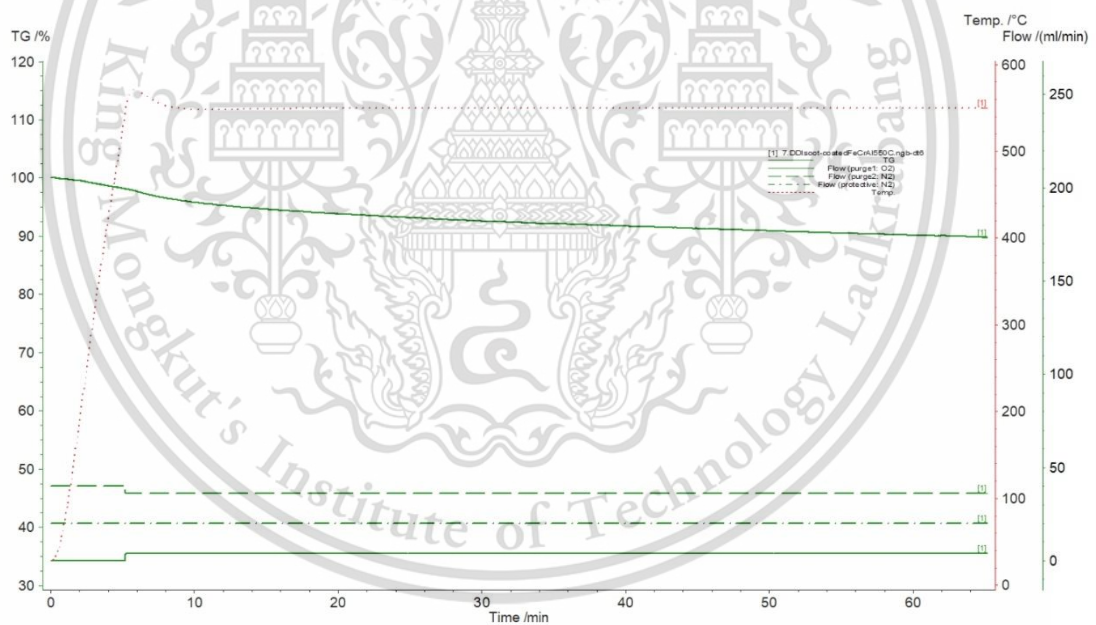
A-18 Test report of TGA cCB 600°C.

This material is reserved for educational use only, not allowed for commercial use.

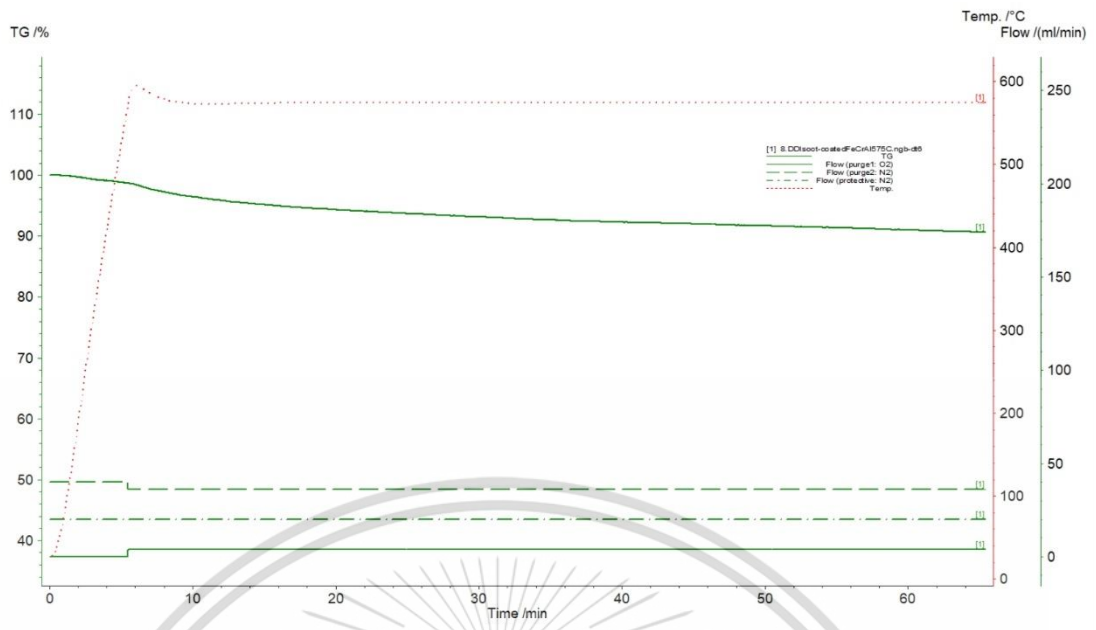
Forbidden to modify the content, and cite the document when use.



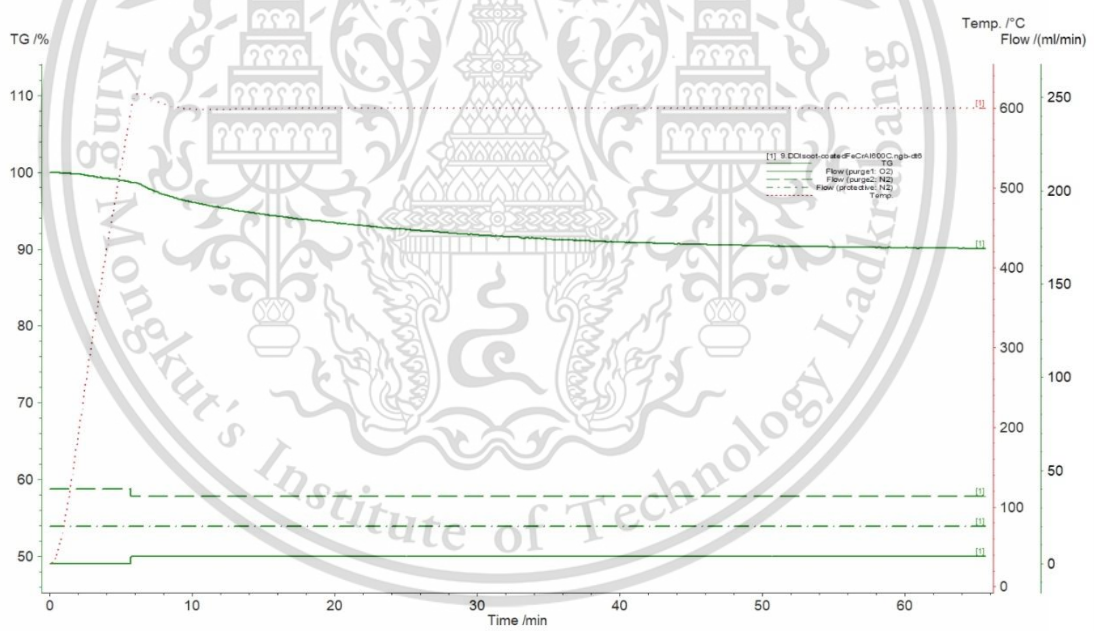
A-19 Test report of TGA cDDI 525°C.



A-20 Test report of TGA cDDI 550°C.



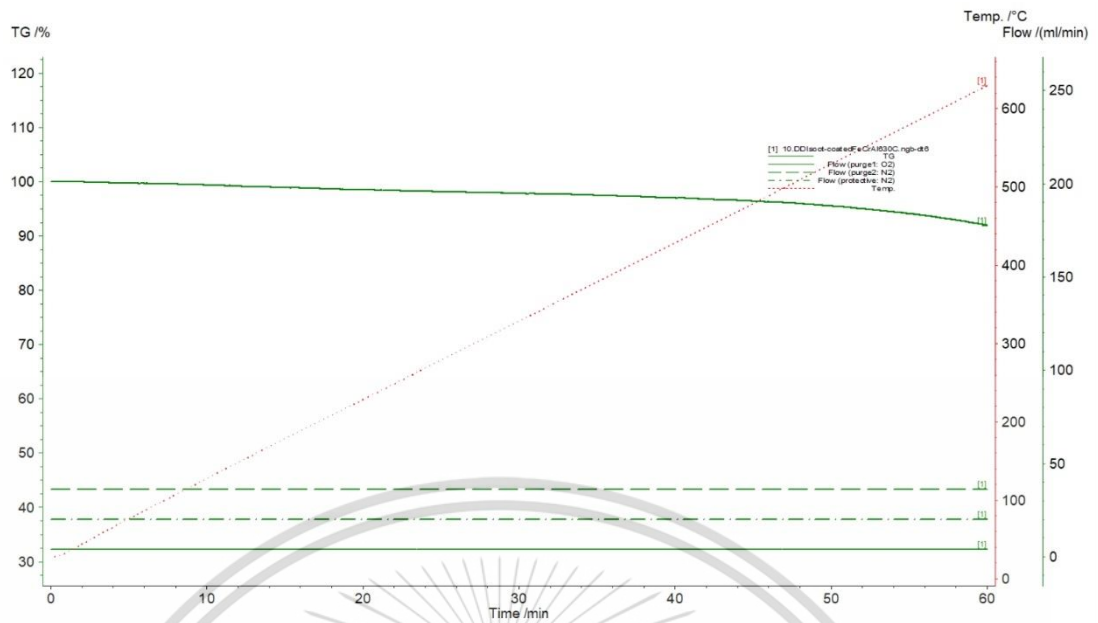
A-21 Test report of TGA cDDI 575°C.



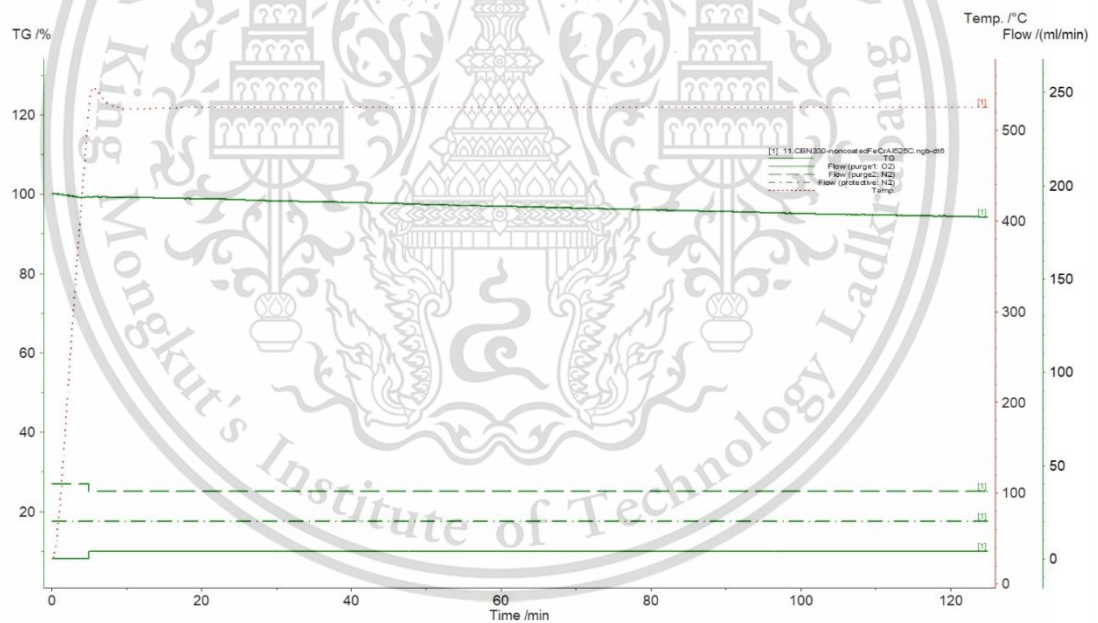
A-22 Test report of TGA cDDI 600°C.

This material is reserved for educational use only, not allowed for commercial use.

Forbidden to modify the content, and cite the document when use.



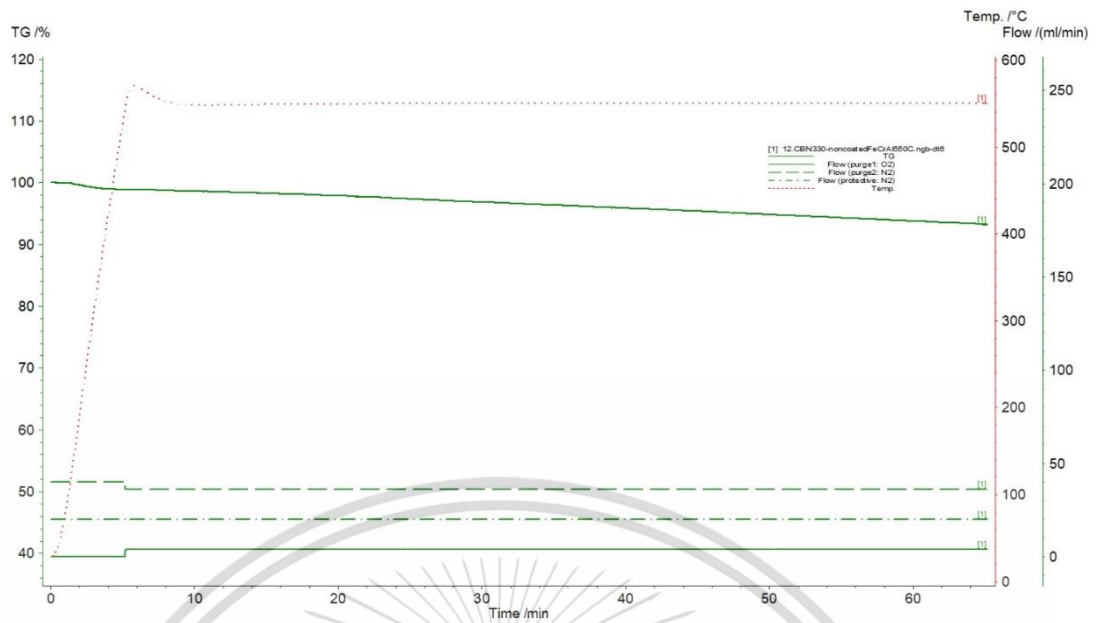
A-23 Test report of TGA cDDI non-isothermal °C.



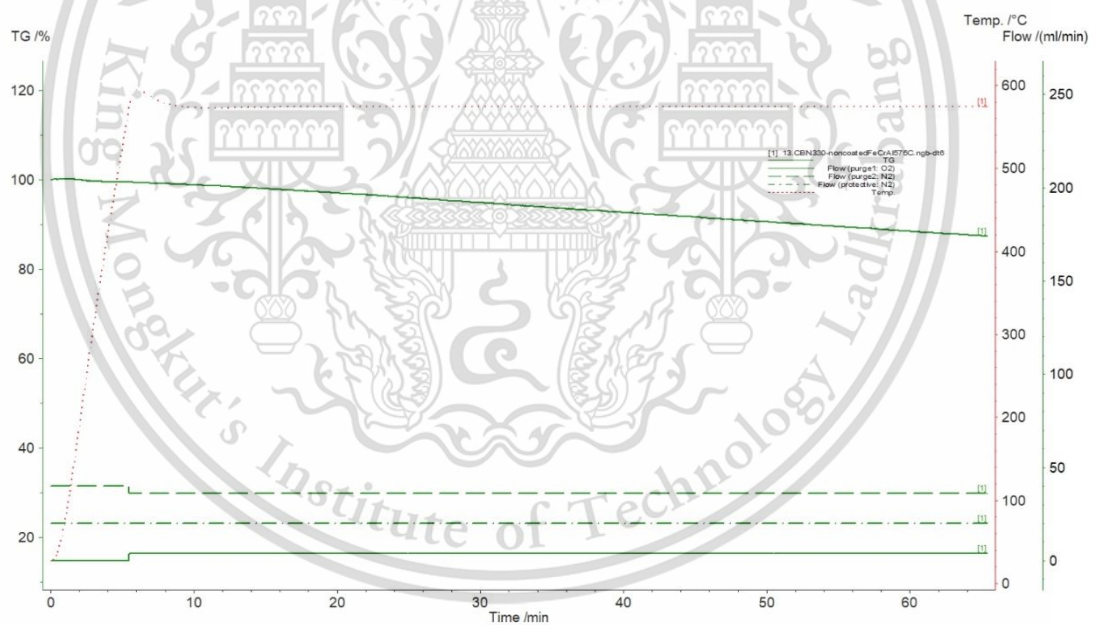
A-24 Test report of TGA nCB 525°C.

This material is reserved for educational use only, not allowed for commercial use.

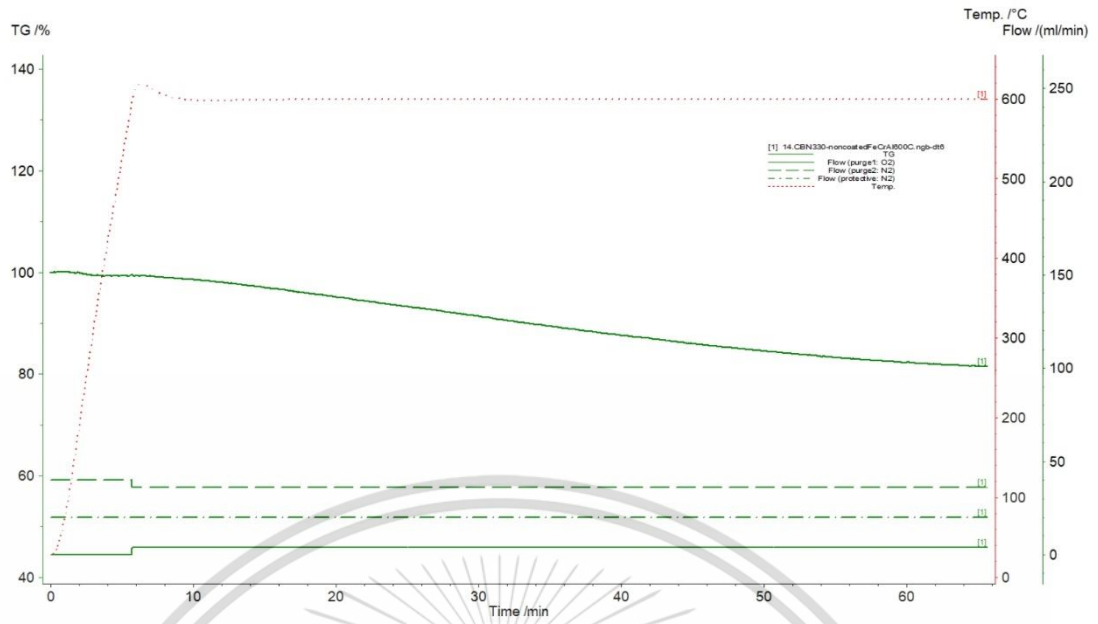
Forbidden to modify the content, and cite the document when use.



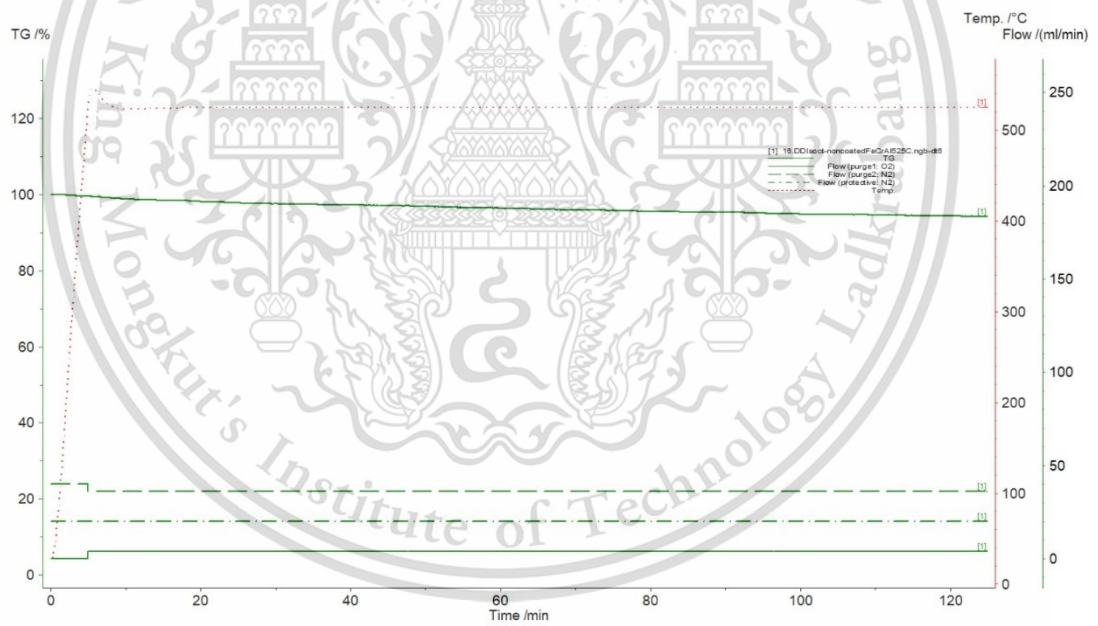
A-25 Test report of TGA nCB 550°C.



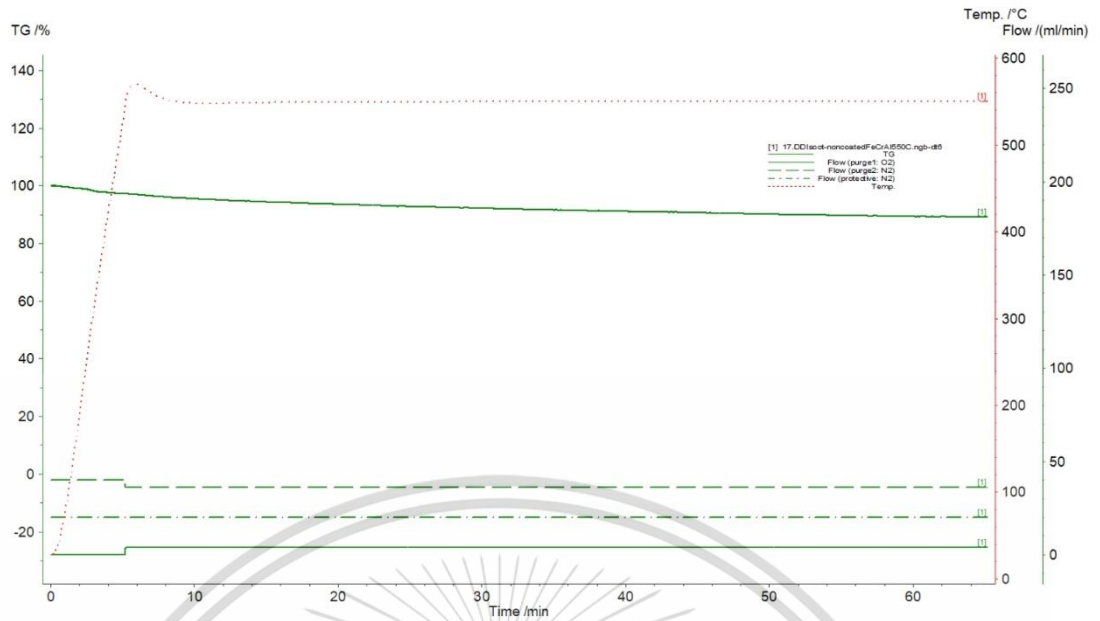
A-26 Test report of TGA nCB 575°C.



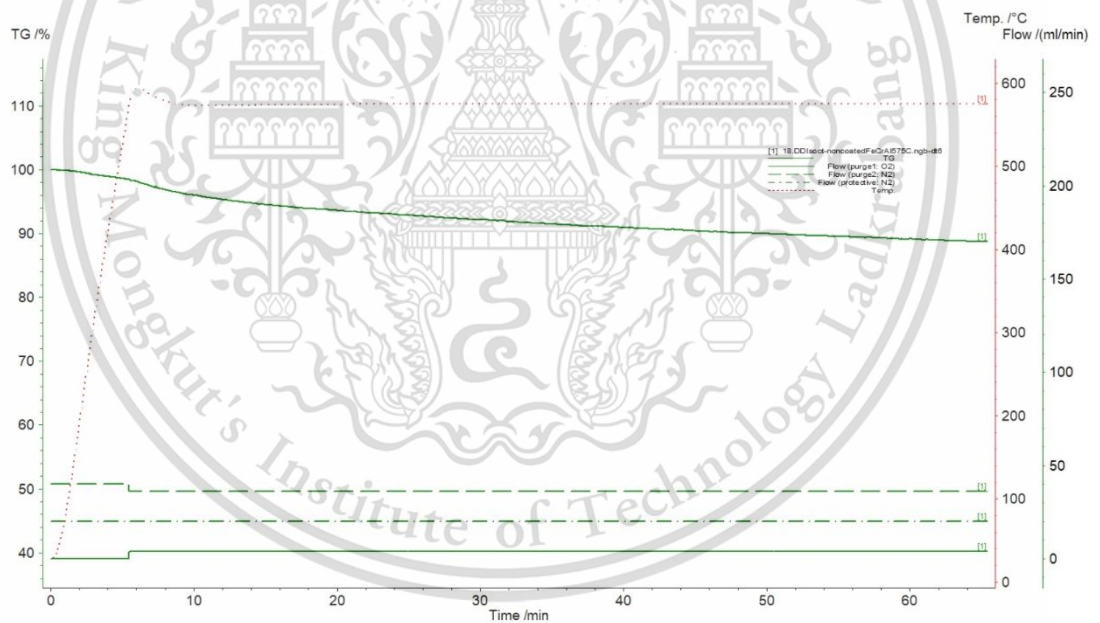
A-27 Test report of TGA nCB 600°C.



A-28 Test report of TGA nDDI 525°C.



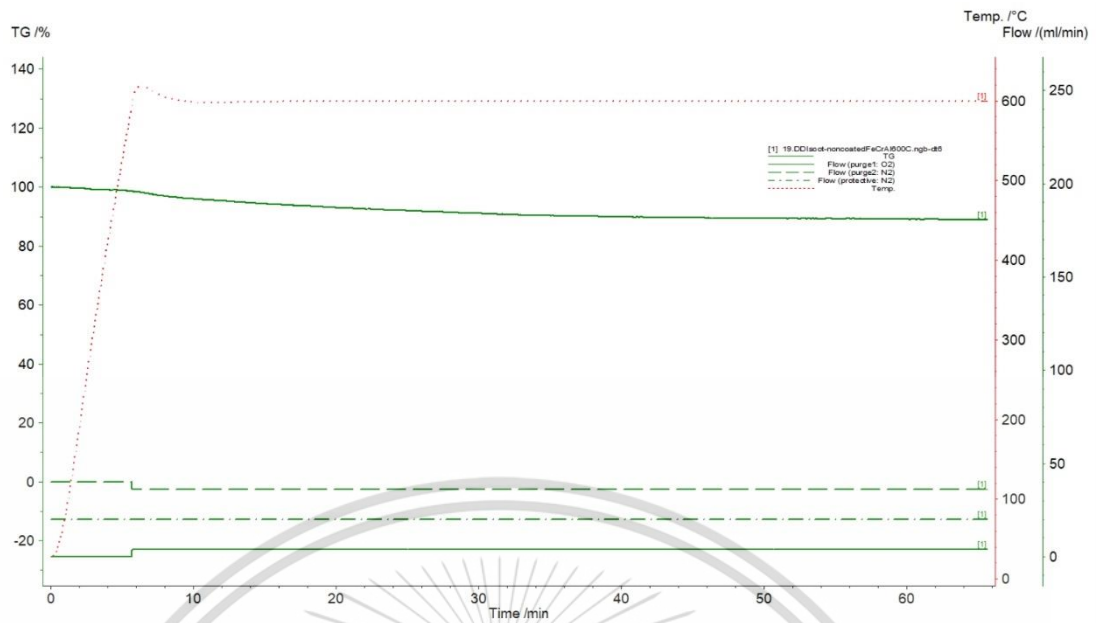
A-29 Test report of TGA nDDI 550°C.



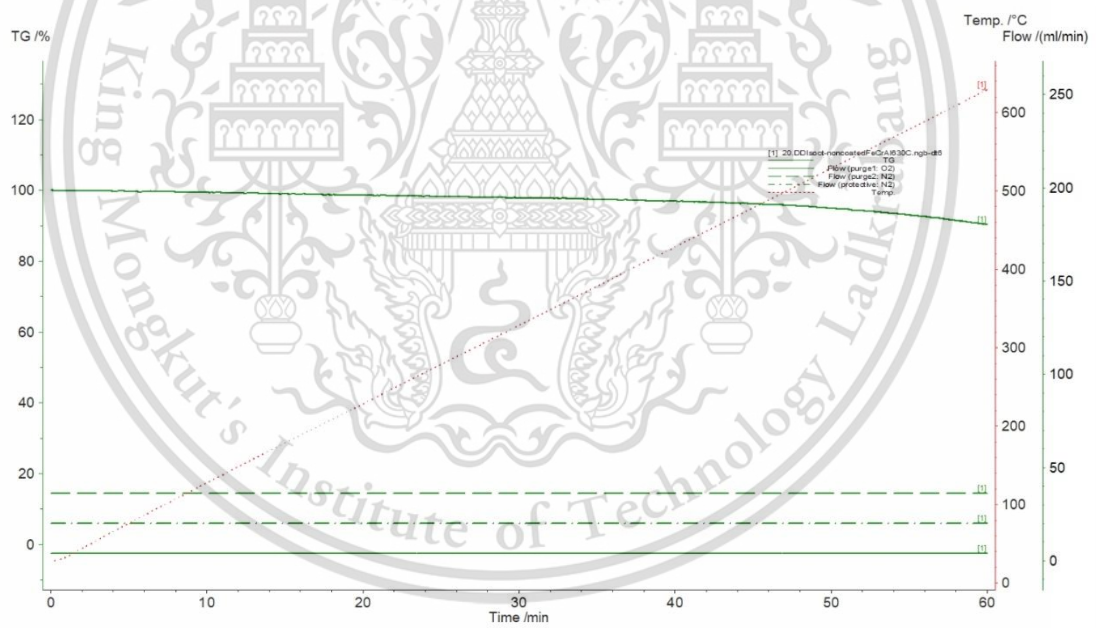
A-30 Test report of TGA nDDI 575°C.

This material is reserved for educational use only, not allowed for commercial use.

Forbidden to modify the content, and cite the document when use.



A-31 Test report of TGA nDDI 600°C.



A-32 Test report of TGA nDDI non-isothermal.

APPENDIX B : REGIONAL CONFERENCE PARTICIPATION

Materials Today: Proceedings xxx (xxxx) xxx



Contents lists available at ScienceDirect

Materials Today: Proceedings

journal homepage: www.elsevier.com/locate/matpr



Characterization of biodiesels and tire derived particulate matters in morphology and nanostructure

Ban-seok Oh^{a,*}, Preechar Karin^a, Mek Sriomsak^a, Kritin Chonvasin^a, Watcharin Po-ngen^b, Sompong Srimanosawapak^c, Katsunori Hanamura^d

^aSchool of Engineering, King Mongkut's Institute of Technology Ladkrabang, Bangkok 10520, Thailand

^bDepartment of Teacher Training in Mechanical Engineering, Faculty of Technical Education, King Mongkut's University of Technology North Bangkok, Bangsue, Bangkok 10800, Thailand

^cNational Metal and Materials Technology Center, National Science and Technology Development Agency, Pathum Thani 12120, Thailand

^dSchool of Engineering, Tokyo Institute of Technology, Tokyo 152-8550, Japan

ARTICLE INFO

Article history:
Available online xxx

Keywords:
Particulate Matter
Biodiesel
Soot
Tire

ABSTRACT

Particulate Matters (PM) are known to be dangerous to human health and the environment. Regulations have been set to limit PM levels from vehicles, including compression ignition engine vehicles. The effect of increasing biodiesel content in the fuels has been investigated with respect to the PM using scanning electron microscopy (SEM) and transmission electron microscopy (TEM). PM from tire emissions were compared against diesel PM using SEM, energy dispersive x-ray spectroscopy (EDS), TEM, particle size analysis, x-ray diffraction (XRD), and Raman spectroscopy (RS). The SEM and TEM show that increasing the biodiesel content decreased the size of the PM agglomerate particles, primary particles, and fringes. The EDS, RS, and XRD show that Tire PM are mostly carbon with silicon, calcium, zinc, and other various trace elements. They also allow comparisons with diesel PM for the carbon nanostructure. The particle size analysis shows that Tire PM are generally larger than engine derived PM. The TEM showed that the nanostructure of the carbonaceous Tire PM was the same fringe structure as the engine derived PM. The Tire PM was successfully characterized using similar methods as engine derived soot. There is strong relationship between the increasing of biodiesel content and reduction of agglomerate size, primary particle size and average fringe length.
Copyright © 2022 Elsevier Ltd. All rights reserved.
Selection and peer-review under responsibility of the 14th AUN/SEED-Net Regional Conference on Materials and 4th International Postgraduate Conference on Materials, Minerals and Polymer (RCM & MAMIP 2021).

1. Introduction

Global sentiment is shifting towards electric vehicles as a major effort to reduce greenhouse gas and other harmful emissions [1–3]. But compression ignition, or diesel, engines remain the main power source for heavy-duty trucks and demand will continue to stay strong [4]. This is because the diesel engine is considered one of the most efficient internal combustion engines with respect to fuel economy and thermal efficiency. However, a main drawback of the diesel engine is the emission, specifically the PM, or soot emissions. Diesel PM is widely known as detrimental to both human health and the environment [5–6].

Diesel PM are formed from these steps: pyrolysis, nucleation, surface growth and coagulation, then aggregation [7]. Pyrolysis occurs from the breakdown of fuel at high temperatures and low oxygen concentrations and is dependent on the engine load and fuel properties [8]. These broken-down particles, known as nuclei, intercept small hydrocarbons and form aromatic molecules [7]. More hydrocarbons and carbon chains deposit on the nuclei forming the primary particles, which aggregate with other primary particles to form the agglomerate particles. It is believed that the carbon chains that form the primary particles are multilayered graphite sheets as they have hexagonally ordered structures [9].

There are two major paths to reduce PM from the exhaust of diesel engines: reducing in the formation process or reducing after the formation process with devices. The reduction of PM in the formation process can be achieved through fuel additives or in this

* Corresponding author.
E-mail address: bsa.peter.oh@gmail.com (B.-s. Oh).

<https://doi.org/10.1016/j.matpr.2022.06.510>

2214-7853/Copyright © 2022 Elsevier Ltd. All rights reserved.

Selection and peer-review under responsibility of the 14th AUN/SEED-Net Regional Conference on Materials and 4th International Postgraduate Conference on Materials, Minerals and Polymer (RCM & MAMIP 2021).

research, increasing the biodiesel content in the fuel. However, another source of carbonous PM from vehicles remains: the tire. There has been previous research on the characterization of tire PM in terms of elemental and chemical composition [10–13]. However, analysis in terms of carbon nanostructure in a similar manner as engine-borne PM has not been fully investigated.

Tire PM should also be analyzed in similar terms as engine-borne PM for its reduction. This research investigates the morphology and nanostructure in diesel PM and how it is affected by biodiesel. This research also characterizes morphology and nanostructure in tire PM.

2. Methodology

2.1. Particulate Matters collection

A 3L 4-cylinder common rail direct injection engine (ISUZU-Dmax 4JJ1-TC) was run at numerous engine speeds and loads with three fuels of varying biodiesel content (B7, B20, and B100). The soot powder was collected from the exhaust pipe after testing under numerous engine speeds and loads for each fuel. Paper filters were used with a BOSCH smoke meter (Okuda DSM-240) to collect soot on the paper filters to examine the agglomerate particles. A Toyota Hilux Tiger pick-up truck was run at various loads and engine speeds on a chassis dynamometer. The solid emissions from the tires were deposited onto flat surfaces behind and below the tires then collected. PM is categorized by size under PM10 (diameter (D) < 10 μm), fine particles or PM2.5 (D < 2.5 μm), ultrafine particles or PM0.1 (D < 100 nm), and nanoparticles (D < 50 nm) [14].

2.2. TEM, SEM, particle size analysis

The paper filters with the engine-born agglomerate particles were examined with SEM (FE-SEM SU8200) under a magnification of 10,000. This was then analyzed with an image processing software, ImageJ, to determine the size of the agglomerate particles. The tire agglomerate particles were compared with engine derived PM with SEM (SU5000) and scattering light nano particle analyzer (Horiba SZ-100 V2). The engine PM powders were examined with TEM (JEM-2100Plus) under a magnification of 30,000 and 800,000 for primary particle and fringe analysis, respectively. The tire PM were examined with TEM under a magnification of 30,000 and 80,000 to allow a detailed investigation into the morphology and size of the biodiesel soot particles. The 30,000 magnification images for the engine PM were analyzed using ImageJ to determine the size of the single primary particles. The 800,000 magnification images for the engine PM were turned to black and white then skeletonized using ImageJ to examine the nanostructure and graphite crystallite of the particles.

2.3. EDS, XRD, RS

Energy dispersive x-ray spectroscopy (EDS) was also utilized to determine the elemental composition of the tire PM. This could allow comparisons to diesel PM as well as existing literature. X-ray diffraction (XRD) and Raman spectroscopy (RS) were also used to confirm the EDS results as well as elaborate on the carbon nanostructure and chemical composition. The XRD equipment (DB Advance) using $\text{CuK}\alpha$ -radiation was used to scan the Tire PM powder in the range: $10^\circ < 2\theta < 90^\circ$. The RS equipment (Horiba LabRAM-HR) was done with Raman shift range of 500 –

2000 cm^{-1} . The different equipment also allowed the comparison of methods for nanostructure and chemical composition analysis.

3. Results and discussion

3.1. Engine PM morphology

The PM from B7, B20, and B100 was investigated for morphology. The SEM images, Fig. 1 show the agglomerate particles on the fibers of the paper filter. They vary in size from hundreds of nanometers to the micron scale. Agglomerated PM derived from the different fuels seem similar in form although there are far fewer B100 derived PM agglomerates. ImageJ was used to measure agglomerate sizes to make agglomerate particle size distributions as shown in Fig. 2. The distributions show a trend where the agglomerate distribution curve shifts to the left, or the size decreases, as the biodiesel content increases.

PM was investigated with 30,000 magnification of TEM for the morphology of the single particles. This can be shown in Fig. 3 with the single primary particles being visibly distinct from each other in an agglomerate. The particle sizes are measured using ImageJ to make the single primary particle size distributions as shown in Fig. 4. Both the average size and the size distribution show the relationship between the increasing biodiesel content and the decreasing size. The size distribution seen in Fig. 4 represents this well with the distribution curve shifting left, or decreasing, as biodiesel content increases.

3.2. Engine PM nanostructure

The PMs derived from the various fuels were investigated for nanostructure. TEM images with a magnification of 800,000 were used, as shown in Fig. 5. Three 10x10 nm squares were cropped from each image and turned to black and white. Then they were cleaned up before turning them into skeleton images where a thick line would transform into a thickness of one pixel. These skeleton images were analyzed to determine the length of the skeletonized fringes. Three squares were done to minimize operator bias. This gave an average fringe length of 1.42, 1.32, and 1.23 nm for B7, B20, and B100, respectively. More information from this analysis can be found in Table 1. It can be seen that increasing the biodiesel content decreases the average fringe length and longest fringe length.

The skeletonized images were also used to determine the interplanar spacing between the graphite platelets that make up the particulate matter. The result of this analysis can be seen in Table 1. The interplanar spacing is very similar, and a relationship cannot be made between the spacing and the biodiesel content. This spacing between the graphite crystallite represents the interlayer spacing between graphene layers or sheets. Braun [15] claimed that PM was composed of varying sizes of these graphene sheets. This would have happened in the accumulation mode of PM formation where carbon crystallites would have accumulated with each other to form the primary particles.

3.3. Tire PM morphology vs. Diesel PM

The tire wear PM was analyzed for morphology. The agglomerated particles of tire wear can be seen in a SEM image, Fig. 6a. The particles are generally ovalar in shape but nonuniform. This can be compared with other research [10,13]. A single primary particle of tire wear can be seen in the TEM image: Fig. 6b. The single primary particle is quite circular but a notable difference between the tire

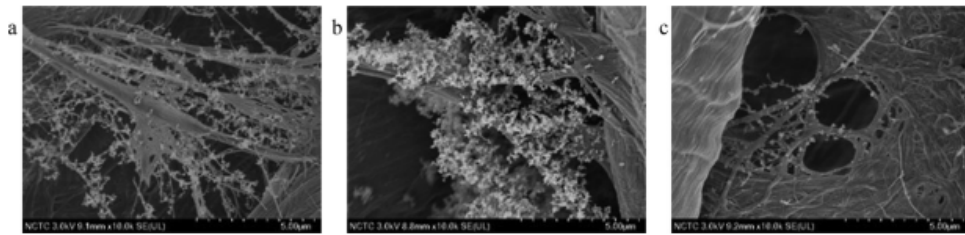


Fig. 1. SEM Images of (a) B7, (b) B20, (c) B100 Derived PM Agglomerates on Paper Filters.

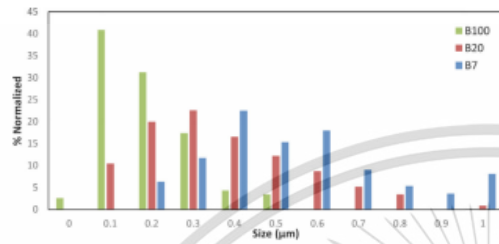


Fig. 2. Size Distribution of B7, B20, B100 Derived PM Agglomerates.

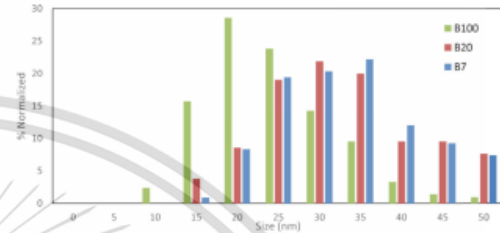


Fig. 4. Size Distribution of B7, B20, B100 Derived PM Primary Particles.

PM and engine-borne PM is that the single primary particle cannot be seen clearly from the agglomerate particle. The agglomerate particle is very much a clumped mass of single primary particles, making it difficult to differentiate between individual primary particles. The agglomerated particles were measured with a scattering light particle size analyzer to show Fig. 7 with an average size of 2.09 µm. Although this average is below the categorization of PM_{2.5}, a significant portion of this curve is larger than this category. This also contrasts with the smaller size of engine-borne PM also seen in Fig. 7 and with an average size of 170 nm. The nanostructure of tire PM was observed using TEM in Fig. 6c. It can be compared with Fig. 5 to show that the nanostructure is quite similar. This is due to the high carbon content in both diesel PM and tire PM.

3.4. Tire PM elemental and chemical composition vs. Diesel PM

The elemental composition of the tire PM was also analyzed with EDS as shown in Fig. 8a. 10 elements were detected: C, O, Fe, Ca, S, Si, Zn, Al, Na, and Cl. These elements were also detected in previous literature with Zn being a favorable marker or tracer

for tire wear PM in overall analysis of atmospheric PM [11–13]. The elemental composition of diesel PM was also analyzed as shown in Fig. 8b. There were significantly fewer elements detected with only C, O, Ca, and S, the latter two representing the ash contamination from engine oil [14].

The chemical composition of the tire PM was then analyzed with XRD and RS as shown in Fig. 9 and Fig. 10, respectively. Fig. 9b also shows the profile matching of ZnO and C₉H₄O₅. As said previously, Zn is used as a tracer and the practicality of this is shown in this figure. The profile of C₉H₄O₅ represents oxygenated polycyclic aromatic hydrocarbons, which is confirmed by the RS analysis shown in Fig. 10. The two peaks shown in Fig. 10 usually represent the carbon nanostructure in terms of degree of graphitization [16]. However, literature suggests these peaks can also represent hydrocarbons and polycyclic aromatic hydrocarbons [17]. This goes back to confirm the profile of C₉H₄O₅, an end product of the oxidation of polycyclic aromatic hydrocarbons.

The XRD and RS results can also give information about the carbon nanostructure, as said previously. Fig. 9a. show that the Tire PM XRD curve was significantly more vibrant compared to the Die-



Fig. 3. 30,000x Magnified TEM Images of (a) B7, (b) B20, (c) B100 Derived PM Primary Particles.

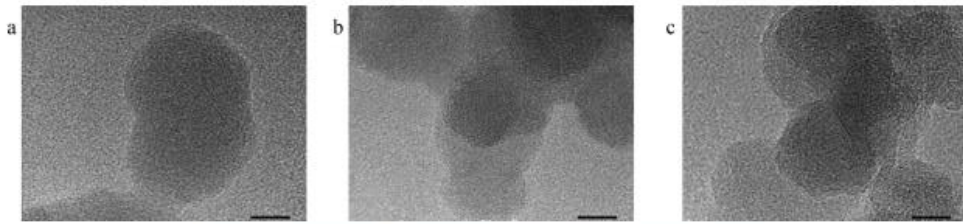


Fig. 5. 800,000x Magnified TEM Images of (a) B7, (b) B20, (c) B100 Derived PM Particles.

Table 1
Summary of Results from Fringe Analysis.

Measurement	B7	B20	B100
Average Fringe Length (nm)	1.42	1.32	1.23
Largest Fringe Length (nm)	6.49	5.28	4.11
Interplanar Spacing (nm)	0.39	0.397	0.386

sel PM with various peaks showing the chemical profiles. However, the two main broad peaks in the Diesel PM represent the [002] and [100] lattice plane which correspond to the amorphous and graphitic nature of the carbon nanostructure [18]. These two peaks

can also be seen in the Tire PM, although not as clearly. This suggests the same methods used to analyze carbon structure in engine-borne PM can also be used on Tire PM, but with caution due to the narrow peaks that correspond to chemical profiles. Fig. 10. show very similar curves between the Tire PM and Diesel PM. These two peaks represent the D and G band, with the D band on the left and the G band on the right [19]. However, it can also be seen that the peak on the right is significantly higher than the peak on the left, which would mean the Tire PM is significantly more graphitic than the Diesel PM. But as discussed before, these peaks and other peaks can represent hydrocarbons and polycyclic aromatic hydrocarbons.



Fig. 6. Tire PM under Magnification of (a) 300x, Agglomerate, (b) 80,000x, Primary Particle, and (c) 800,000x, Crystallites.

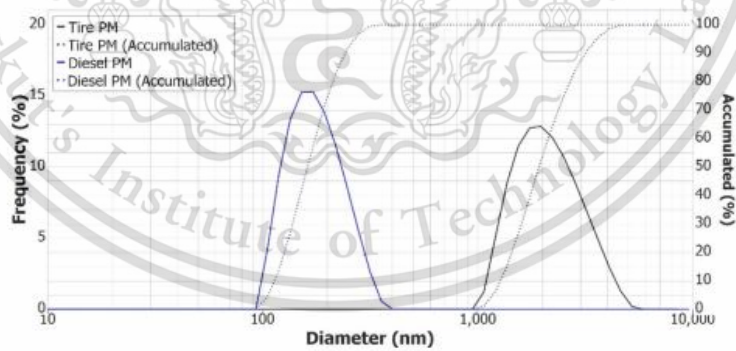


Fig. 7. Size Distribution of Tire PM and Diesel PM.

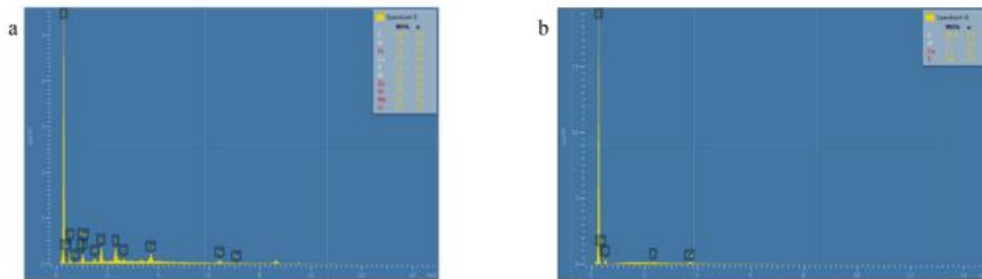


Fig. 8. EDS spectra of (a) Tire PM and (b) Diesel PM.

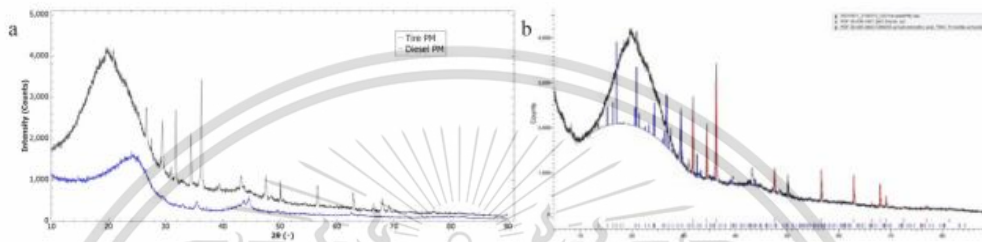


Fig. 9. XRD Diffractograms (a) comparing Tire PM with Diesel PM and (b) with (blue) ZnO and (red) C₉H₄O₅ profiles. (For interpretation of the references to colour in this figure legend, the reader is referred to the web version of this article.)

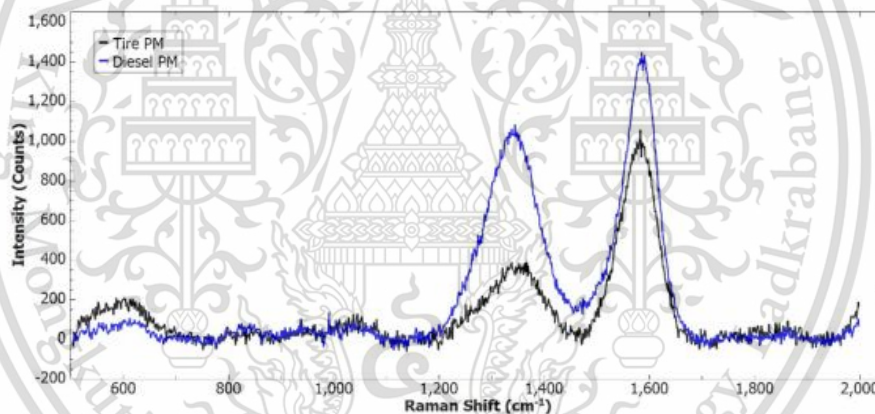


Fig. 10. Raman Spectra of Tire PM and Diesel PM.

4. Conclusion

The soot from varying biodiesel contents (B7, B20, B100) and tire emissions were collected and investigated. The morphology of the soot agglomerate particle and single primary particles were observed using SEM and TEM in terms of size distribution. These distributions showed that there is a relationship between the biodiesel content and distribution curve. An increase of biodiesel con-

tent shifted the distribution curve left, meaning the size of both the agglomerate particles and single primary particles decreased as the biodiesel content increased from B7 to B20 to B100. As for the fringe analysis, a relationship between the biodiesel content and fringes can also be seen. The average fringe length and the largest fringe length decreased as the biodiesel content increased. The interplanar spacing was similar for all three fuel-derived PM, and so a relationship between the spacing and the biodiesel content

cannot be definitively made. Nonetheless, there exists a relationship between the biodiesel content and the PM nanostructure and morphology.

Tire wear PM was analyzed in terms of size distribution, elemental composition, and nanostructure. The average size of an agglomerated tire PM was 2.09 μm and the shape of the tire PM was generally ovalar but irregular. The tracer element of Zn was detected, along with seven other elements that are not C or O. The XRD confirmed this as well as bring up the profile of an end-product of oxidized polycyclic aromatic hydrocarbons. This was confirmed using RS and comparisons with other literature. The nanostructure of the tire PM has a significant carbon portion which could allow fringe-based analysis in the future as well as comparison between XRD and RS results for graphitization.

The relationship between biodiesel content, morphology, and findings from this research can be utilized in future research on the reduction of PM from the exhaust of compression ignition engines, such as PM trapping and oxidizing devices like the diesel particulate filters. The ability to analyze tire wear with focus on the carbon portion could also allow future research in the trapping and reduction of tire wear emissions.

Declaration of Competing Interest

The authors declare that they have no known competing financial interests or personal relationships that could have appeared to influence the work reported in this paper.

Acknowledgements

The authors would like to thank the National Research Council of Thailand (Diesel Engine's Particulate Matters Reduction using Ethanol- Biodiesel- Diesel Blends and Particulate Filter 398/2563) and King Mongkut's Institute of Technology Ladkrabang for their support.

References

- [1] H. Choi, Technology-push and demand-pull factors in emerging sectors: evidence from the electric vehicle market, *Industry Innov.* 25 (2018) 655–674, <https://doi.org/10.1080/13662716.2017.1346502>.
- [2] M. Tran, J.D. Bishop, D. Banister, M.D. McCulloch, Realizing the electric vehicle revolution, *Nat. Cl. Change* 2 (2012) 328–333, <https://doi.org/10.1038/nclimate429>.
- [3] P. Hertzke, N. Müller, S. Schenk, Dynamics in the global electric-vehicle market, *McKinsey Center for Future Mobility* (2017).
- [4] A. Askin, G. Barter, T. West, D. Manley, The heavy-duty vehicle future in the United States: A parametric analysis of technology and policy tradeoffs, *Energy Policy* 81 (2015) 1–13, <https://doi.org/10.1016/j.enpol.2015.02.005>.
- [5] N. Englert, Fine Particles and Human Health - A review of epidemiological studies, *Toxicol. Lett.* 3 (2004) 235–242, <https://doi.org/10.1016/j.toxlet.2003.12.035>.
- [6] S. Steiner, C. Bisig, A. Petri-Fink, B. Rothen-Rutishauser, Diesel exhaust: current knowledge of adverse effects and underlying cellular mechanisms, *Arch. Toxicol.* 90 (2016) 1541–1553, <https://doi.org/10.1007/s00204-016-1736-5>.
- [7] S. Mohankumar, P. Senthilkumar, Particulate matter formation and its control methodologies for diesel engine: A comprehensive review, *Renew. Sust. Energy Rev.* 80 (2017) 1227–1238, <https://doi.org/10.1016/j.rser.2017.05.133>.
- [8] P. Karin, H. Oki, K. Hanamura, C. Charoenphonphanich, Nanostructures and oxidation kinetics of diesel particulate matters, *J. Res. App. Mech. Engr.* 2 (2012) 3–8.
- [9] V. Fernandez-Alos, J. Watson, R. Vander Wal, J. Matthews, Soot and char molecular representations generated directly from HRTEM lattice fringe images using Fringe3D, *Comb. Flame* 158 (2011) 1807–1813, <https://doi.org/10.1016/j.combustflame.2011.01.003>.
- [10] Y. Tonegawa, S. Sasaki, Development of tire-wear particle emission measurements for passenger vehicles, *Emission Control Sci. Tech.* 7 (2021) 56–62, <https://doi.org/10.1007/s40825-020-00181-z>.
- [11] J.K. Gietl, R. Lawrence, A.J. Thorpe, R.M. Harrison, Identification of brake wear particles and derivation of a quantitative tracer for brake dust at a major road, *Atm. Env.* 44 (2010) 141–146, <https://doi.org/10.1016/j.atmosenv.2009.10.016>.
- [12] A. Thorpe, R.M. Harrison, Sources and properties of non-exhaust particulate matter from road traffic: a review, *Sci. Tot. Env.* 400 (2008) 270–282, <https://doi.org/10.1016/j.scitotenv.2008.06.007>.
- [13] M. Kovochich, M. Liong, J.A. Parker, S.C. Lee, J.P. Oh, L. Xi, M.L. Kreider, K.M. Unice, Chemical mapping of tire and road wear particles for single particle analysis, *Sci. Tot. Env.* 757 (2021), <https://doi.org/10.1016/j.scitotenv.2020.144085>.
- [14] D.B. Kittelson, Engines and nanoparticles: a review, *J. Aerosol Sci.* 29 (1998) 575–588, [https://doi.org/10.1016/S0021-8502\(97\)10037-4](https://doi.org/10.1016/S0021-8502(97)10037-4).
- [15] A. Braun, F.E. Huggins, S. Seifert, J. Ilafsky, N. Shah, K.E. Kelly, A. Sharofim, G.P. Huffman, Size-range analysis of diesel soot with ultra-small angle X-ray scattering, *Comb. Flame* 137 (2004) 63–72, <https://doi.org/10.1016/j.combustflame.2004.01.003>.
- [16] F. Tuinstra, J. Koenig, Raman spectrum of graphite, *J. Chem. Phys.* 53 (1970) 1126, <https://doi.org/10.1063/1.1674108>.
- [17] X. Li, J. Hayashi, C.Z. Li, FT-Raman spectroscopic study of the evolution of char structure during the pyrolysis of a Victorian brown coal, *Fuel* 85 (2006) 1700–1707, <https://doi.org/10.1016/j.fuel.2006.03.008>.
- [18] A. Coesta, P. Dhameinacourt, J. Laureyns, A. Martinez-Alonso, J. Tascon, Comparative performance of X-ray diffraction and Raman microprobe techniques for the study of carbon material, *J. Mat. Chem.* 8 (1998) 2875–2879.
- [19] Y. Wang, D. Alsmeyer, R. McCreery, Raman spectroscopy of carbon materials: structural basis of observed spectra, *Chem. Mat.* 2 (1990) 557–563, <https://doi.org/10.1021/cm00011a018>.

Thin film Ceria Using RF Sputtering on Metal Fibers for Catalyzing Diesel Soot Oxidation

Ban-seok Oh¹⁾ Preechar Karin¹⁾ Mek Srilomsak¹⁾ Watcharin Po-ngen²⁾ Sompong Srimanosawapak³⁾ Withawat Wongpisan³⁾ Katsunori Hanamura⁴⁾

1) School of Engineering, King Mongkut's Institute of Technology Ladkrabang, Bangkok, 10520, Thailand

2) Faculty of Technical education, King Mongkut's University of Technology North Bangkok, Bangsue, Bangkok, 10800, Thailand

3) National Metal and Materials Technology Center, National Science and Technology Development Agency, Pathum Thani, 12120, Thailand

4) School of Engineering, Tokyo Institute of Technology, Tokyo, 152-8550, Japan

ABSTRACT: Metallic Partial-Flow Diesel Particulate Filter Fibers were coated using RF Sputtering with CeO₂ for the purpose of catalyzing the oxidation of diesel soot particles trapped on the fibers. The coating process was a Physical Vapor Deposition (PVD) Method using a cerium oxide target. The coated filter was then compared with the non-coated filter in terms of chemical structure with X-ray diffraction analysis and oxidation with thermogravimetric analysis using carbon black and diesel soot from a light duty engine. The coated filter with Ceria using PVD was confirmed and that it could reduce the activation energy of the soots' oxidation.

KEY WORDS: heat engine, particulate filter, harmful emissions, Soot Oxidation, RF Sputtering (A1)

1. INTRODUCTION

Diesel powered vehicles are widely used in the developing world, including Thailand where light-duty diesel trucks alone make up over a third of the private automotive market share. This is because of diesel engines have a relatively high thermal efficiency and fuel economy. But this also contributes significantly to the local pollution due to the harmful emissions from diesel combustion, especially particulate matter (PM).

In order to reduce these emissions, exhaust after-treatment systems are widely used, such as a diesel oxidation catalyst (DOC) and diesel particulate filter (DPF). DPFs are categorized into full-flow and partial-flow where the full or partial amount of the exhaust is forced through a filter, respectively. Full-flow DPFs are usually more efficient at filtering PM, but require an active system to monitor and regenerate the filter once it is saturated. They are usually made up of a ceramic honeycomb structure.

Partial-flow DPFs do not require an active system but has lower filtration performance. They are usually made up of microscale metal fibers and metal flow guides that guide a portion of the exhaust into the filter media⁽¹⁾. For both DPFs, a DOC can be paired with them so that the exhaust gas is treated⁽²⁾. However, this requires more space in the engine bay. So an increasing amount of DPFs are produced with a catalyst coating so that this catalyzed DPF (CDPF) can function as both a DOC and DPF while taking up less space. Another benefit of combining these functions is that the energy required to regenerate the filters and heat capacity of the whole unit can be reduced by the catalyst coating.

The DPF coating can be done using various methods including various dip coating techniques⁽³⁾. However, it is difficult to form nanoscale thin layer coatings on microscale fibers using these techniques. This can be desired in order to maintain the high porosity that is associated with the partial-flow DPF. To achieve this, a physical vapor deposition (PVD) method can be used. This method allows for consistent thin layer coatings using a wide array of catalyst materials for various applications. This research will be concerned about using this thin layer coating as a nanocatalyst for PM oxidation.

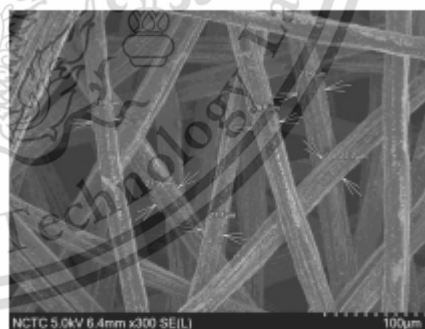


Fig.1 SEM of metal microfibers used in this research with some diameter measurements

2. METAL FIBERS AND COATING

2.1. Uncoated metal fibers

Fig.1 shows the metal fibers that make up the metal fleece used in this research. The fibers are 20-30 μm in diameter and

are randomly nonwoven into a fleece. This fleece is then wound together with a flow guide foil such that a portion of the exhaust gas is forced towards the filter. This filter allows PM to become trapped on the fibers. To maintain its peak trapping performance, the filter has to oxidize the trapped soot.

The fibers alone do not have catalyzing elements as shown by the electron dispersive spectroscopy in Fig.2. It is made up of Fe, Cr, Al, and C with a trace amount of Si. The first three elements are the main elements that make up the alloy used in this fiber, i.e., stainless steel. The stainless steel is used here because of its corrosion resistant properties and ability to withstand thermal cycling. These also allow a long lifetime of the product without worrying too much about the maintenance. The C detected here is from the contamination of dust and from the strengthening alloy. The Si is from the lubrication that is used to produce these metal microfibers.

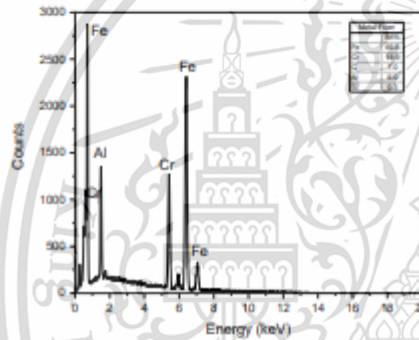


Fig.2 EDS of metallic microfibers

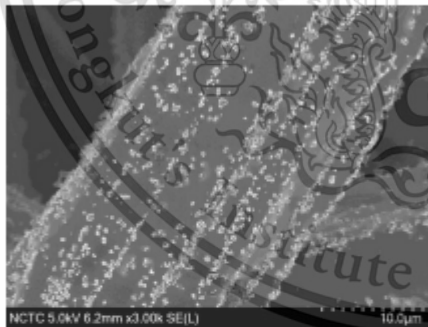


Fig.3 SEM of metal fibers showing surface microstructure

Fig.3 shows the microstructure of the metal fibers at a magnification of 3000x. It can be seen that the surface is full of small external grains less than 1 micron in diameter. They also seem to be in some pores of the fiber. These grains also seem to

be in a linear formation with relation to the length of the fiber. This suggests it is related to the manufacturing of these fibers. Because these fibers are formed by drawing, it is reasonable to assume these grains are due to the high stresses between each of the bundled fibers. As such, these grains will be called impurity grains.

2.2. Coating process

The PVD method was used to coat CeO_2 onto the fibers. Previous research proved that this thin coating method is possible on fibers smaller than the ones used here⁽⁴⁾. The target was a CeO_2 ceramic target and RF sputtering was used to deposit the thin layer of catalyst material. A CeO_2 ceramic target was used instead of a Ce metallic target because of the relative ease of the atmosphere balance. The metallic target requires a delicate control of the O in the atmosphere to form CeO_2 instead of pure Ce or the oxygen deficient Ce_2O_3 . Even using the ceramic CeO_2 target can allow Ce_2O_3 to form because of how O has the tendency to diffuse into the sputtering atmosphere. Some literature have mitigated this by introducing O into the atmosphere but this will not be used here⁽⁵⁾.

First, pre-sputtering was done to clean the target and the substrate. 10W power and a substrate bias of -109 V was used for 20 minutes with the target shutter closed so that the substrate was not coated during this cleaning. The sputtering atmosphere was Ar at a base pressure of 70 mtorr and a deposition pressure of 6.3×10^{-2} mbar. The substrate temperature was at room temperature with a bias of -10V and was rotated in a speed of 1rpm. The substrate was not separately heated because previous literature showed that this was not necessary⁽⁵⁾. The bias was used to help the substrate attract the coating material and increase the deposition rate as well as improve the coating performance for this filter material. The rotation was to help the uniform deposition of the coating material.

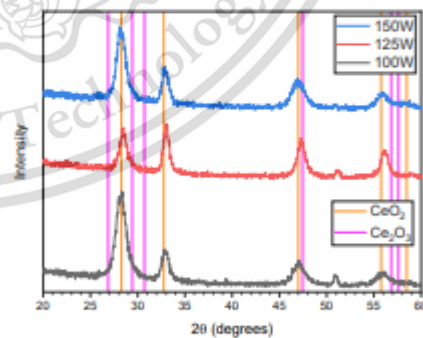


Fig.4 XRD of coating under various power sources

Power sources of 100W, 125W, and 150W were used for 20 minutes on a Si wafer to confirm the sputtered coating was in fact CeO_2 instead of the O deficient Ce_2O_3 . The O deficient Ce_2O_3 is less efficient in catalytic performance as well. The analysis can be seen in Fig.4 where x-ray diffraction was used to determine the phase locations of the sputtered coating. All three power sources showed that the coating matched better with the CeO_2 phase locations than the Ce_2O_3 phase locations.

After the phases were confirmed, the 100W and 150W power sources were investigated to determine the deposition rates, the ideal power source, and depositing time. The 150W was chosen with a deposition time of 1 hour because the calculated deposition rate was over 5 nm/min. The result of the coating on the Si wafer can be seen in Fig.5, where the thickness was measured to be around 337-354 nm.

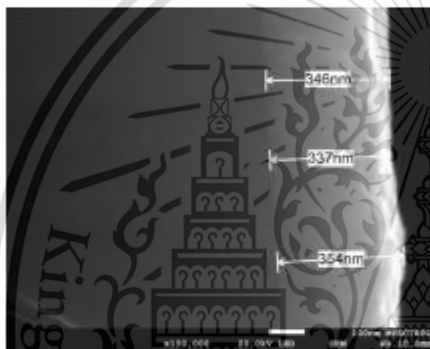


Fig.5 SEM of coating on Si wafer to determine thickness

Since the substrate type does not most significantly alter the deposition and formation, a consistent deposition rate was assumed across both the Si wafer and the metal microfibrinous fleece⁽⁴⁾. This would mean that the coated fibers would still maintain their high porosity as this addition of thickness was only 2% of the original diameter. This was less than the deviation of the fiber diameter seen in Fig.1 which would mean porosity of the filter media would stay virtually unchanged.

2.3. Coated metal fibers

The coating can be observed in Fig.6. The surface is much smoother than before due to the uniform coating by the PVD method. The impurity grains can still be seen but it is essentially buried under the CeO_2 coating. The coating is also quite difficult to distinguish at some areas due to how thin film it is.

However Fig.6 shows that some areas formed granular CeO_2 instead of the uniform coating as seen before. This can be

mistaken for the previously rough surface of the uncoated metal fibers but the grains are different in that they are grouped together and on top of each other. They are also larger than the impurity grains from before.

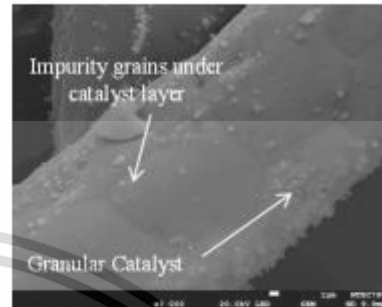


Fig.6 SEM of coating on microfiber

Although the catalyst grains are not ideal in terms of the coating, it could be beneficial to the oxidation of the PM as there is more surface area and therefore more potential contact between the catalyst and the soot. However, the grains could mean that the coating was not dense and could flake off.



Fig.7 SEM of sheared microfiber with coating on top

Fig.7 shows the cross sectional cut of a metal fiber using a metal shear. The coating is noted to be the lighter color. This image shows the direction of the cut but it also shows that the coating behaved like a flour coating stuck on a piece of dough. The coating did not flake off and when the deformation occurred, the coating moved with the metal material to shows the behavior of the overall metal and not just the coating. This shows that the coating was well done with the material bonding well with the metal fiber instead of forming a shell-like outerlayer of the coating.

3. SOOT OXIDATION ON METAL FLEECE

3.1. Mechanism in trapping and regeneration

In order to test the performance of the catalyst coating, the oxidation of soot had to be examined with and without the coating. For this, thermogravimetric analysis (TGA) was used with the isothermal method quantitatively analyze the oxidation and the non-isothermal method with a heating ramp of 10°C/min to view the oxidation behavior. Temperatures of 525, 550, 575, and 600°C were maintained under the isothermal method while the soot was oxidized in the test to determine the activation energy from the oxidation curve. To imitate the real life conditions, soot was loaded onto the fibers before the experiment, this combination was then inserted into the TGA equipment.

To obtain repeatability and enough soot mass for the equipment to detect, soot had to be loaded manually on the fibers before oxidized. This manual loading had to be compared with the realistic soot trapping to determine if the loading and contact between the soot and fibers were similar enough to assume this method was not primarily responsible for a potential difference in oxidation mechanisms.

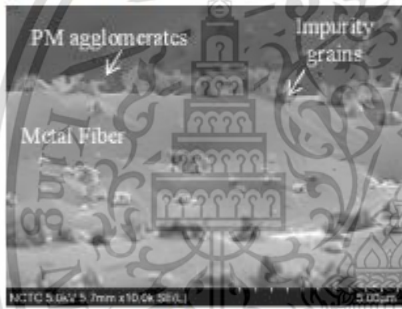


Fig.8 Soot trapping after 1 second

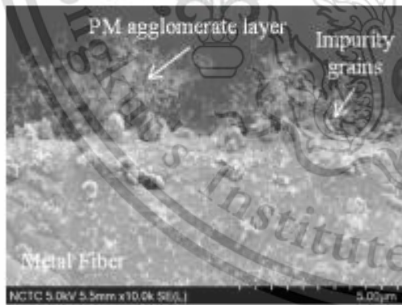


Fig.9 Soot trapping after 30 seconds

Soot was trapped on pieces of metal fleece by introducing raw diesel engine exhaust for 1 second and 30 seconds. Fig.8 shows the metal fibers after 1s of trapping diesel PM. This shows

the initial trapping mechanism and behaviors. The PM seems to be attracted to the impurity grains and it formed on top of them rather than the clean metal surface. Fig.9 shows the metal fibers after 30s of trapping PM. This shows the subsequent layer formation and growth of the trapped PM. The PM is seen to be attracted to each other and is on top of other PM instead of the clean metal surface.

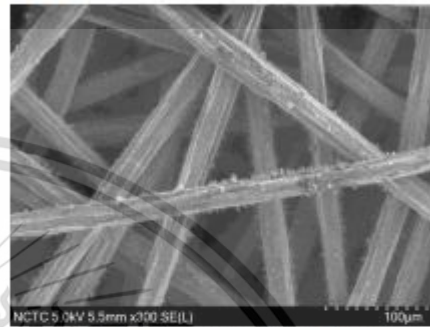


Fig.10 Wider scale of realistic soot loading



Fig.11 Wider scale of manual soot loading

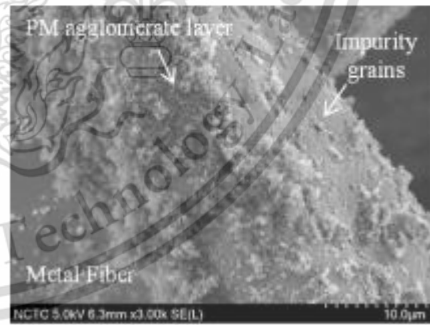


Fig.12 Manual soot loading

The overall image of the 30s trapping seen in Fig.10 can be compared with the manually loaded fleece in Fig.11. The

realistic trapping shows PM trapped in dendritic clumps on top of the initial layer of PM. The manual soot trapping is much denser and is not as uniformly distributed as the realistic trapping. It seems that some sections of the metal fleece has no PM trapped. Fig.12 shows the contact between the PM and the metal fibers. The manually trapped PM is denser and there seems to be more PM on the fibers than the realistic trapping, but the PM trapping is quite similar for both trapping conditions in some segments of the surface. It should be noted that there is more contact between the PM and the fiber which may allow more influence of the catalyst, although the higher interaction between the aerosol PM and the exhaust gases will not be replicated in the TGA.

The oxidation mechanism analyzed will be the activation energy of the oxidation of soot. The chemical equation that summarizes this reaction is seen in Equation (1). This can then be represented by Equation (2) in terms of chemical reaction kinetics where PM is the mass of the carbonaceous PM, t is time, k is the chemical reaction rate, and m and n are the reaction orders of PM and O_2 , respectively.



$$-d[PM] / dt = k [PM]^m [O_2]^n \quad (2)$$

The reaction order n is assumed to be 1 as a complete internal surface diffusion model where the rate of reaction would be proportional to the PM. This reaction can be expressed as the Arrhenius equation in Equation (3) where A represents the frequency factor, E_a is the activation energy, R is the universal gas constant, and T is the temperature in Kelvin.

$$K = A e^{-E_a/RT} \quad (3)$$

Equation (2) and Equation (3) can be combined to form Equation (4) which represents the change of the PM mass as a percentage.

$$-d[PM] / dt / [PM] = A e^{-E_a/RT} [O_2]^n \quad (4)$$

This can be derived into an Arrhenius equation as seen in Equation (5) where C represents the constant in Equation (6). This allows a simple linear calculation of the activation energy where the left hand side is the y -axis, the $-E_a/R$ represents the linear constant, and the $1/T$ represents the x -axis.

$$\ln(-d[PM] / dt / [PM]) = (-E_a/R) \times (1/T) + C \quad (5)$$

$$C = \ln A + m \ln [O_2] \quad (6)$$

The activation energy is the external energy needed for a reaction to occur. This is especially important for PM because the most convenient way to regenerate a DPF, after it is saturated with PM, is to oxidize the PM on the DPF. This will allow the DPF to trap PM while also minimizing back pressure which

could hinder the engine's performance. If the thin layer coating can reduce this activation energy and by how much will be seen in the following sections.

3.2. Soot oxidation on uncoated metal fleece

Model PM and real diesel PM were oxidized on the metal fleece to allow future research to substitute diesel PM with the model PM due to the difficulty of sourcing real engine borne PM in quantities enough to run TGA tests. The real diesel PM was sourced from a light-duty diesel engine. The model PM is CBN330 and it is almost entirely carbon with primary particles that are on average 30 nm in diameter (7). Although both diesel PM and CBN330 are primarily carbon, diesel PM is made up of unstable hydrocarbons and disordered carbon (8). CBN330 is generally more graphitic and more difficult to oxidize due to this higher ordered carbon but this is the most similar in size to the primary particles that make up the carbonaceous soot in diesel PM (9). By analyzing the oxidation of both soots, the impact of the catalyst on different nanostructures will also be shown.

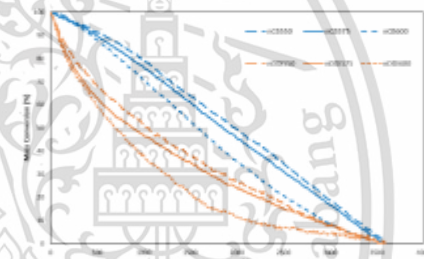


Fig.13 Mass conversion of soot on non-coated fleece



Fig.14 Arrhenius plot of soot on non-coated fleece

To analyze the effects of the structure of the soot on the uncoated metal fleece, TGA was done with the CBN330 (nCB) and the diesel PM (nDDI). The mass conversion graph with key isothermal temperatures can be seen in Fig.13. It can be seen that as the isothermal temperature increases, the slope at which soot

is oxidizes is steeper. These slopes were then used to create the Arrhenius plot in Fig.14. Each point in this plot is from a single isothermal mass conversion curve. The points then form a line in which the slope can be calculated to find the activation energy. The activation energies for CBN330 and diesel PM were 167 kJ/mol and 128 kJ/mol, respectively. This is an acceptable activation energy when compared to previous literature even though the samples used here are not powder-based like in the literature ⁽¹⁰⁾. This meant that the raw fibers alone did not significantly alter the oxidation kinetics of the soot.

It can be seen that the activation energy for diesel PM is lower than CBN330 due to the previously mentioned fact that diesel PM contains more easily oxidizing fractions. This is the most clear when comparing the mass conversion curves in Fig.13. Every mass conversion curve from the oxidation of diesel PM is grouped together with each other and there is a significant gap between this group and the group from the CBN330 oxidation. Anyways, these results also give the baseline result of the soot oxidation kinetics so that comparisons with the coated metal fleece can be made.

3.3. Effect of catalyst coating on CBN330 oxidation

The previously mentioned coated metal fleece were then analyzed by loading the coated and non-coated fleece with CBN330 (cCB and nCB in the graphs, respectively). This was to analyze the effect of the catalyst on CBN330 oxidation and therefore the carbon structure of the soot. The isothermal temperatures used here were the same as before to allow a direct comparison.

Fig.15 shows the mass conversions of CBN330 with the coated and uncoated metal fleece. The curves seem quite similar between the coated and non-coated case, therefore, further analysis is needed. This comes in the form of the Arrhenius graph in Fig.16.

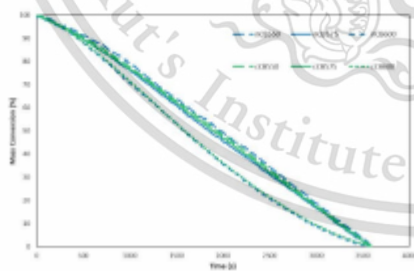


Fig.15 Mass conversion of CBN330 on coated and non-coated fleece

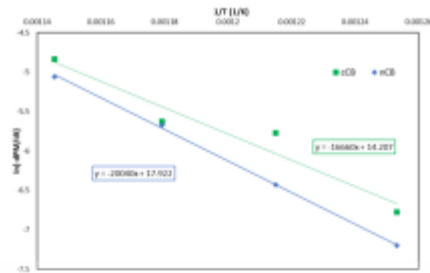


Fig.16 Arrhenius plot of CBN330 on coated and non-coated fleece

It should be noted that almost every point in the Arrhenius graph is significantly different between the non-coated and coated cases. It is clearly shown that the catalyst is able to change the oxidation behavior in each temperature.

The activation energies were calculated to be 167 kJ/mol and 138 kJ/mol for oxidation of the metal fleece without and with the coating, respectively. It can be seen that the catalyst coating decreased the activation energy by 17%. This clearly shows that the catalyst can reduce the activation energy for even the more highly ordered carbon in CBN330.

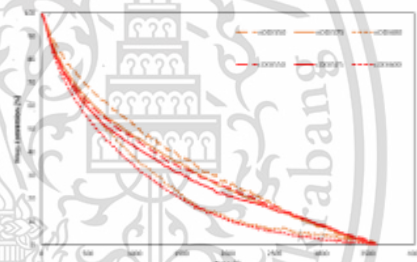


Fig.17 Mass conversion of diesel PM on coated and non-coated fleece

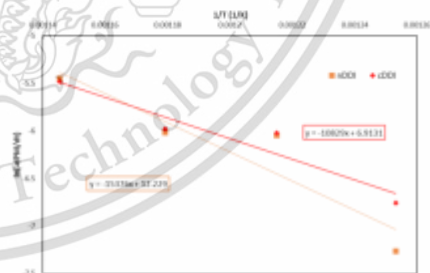


Fig.18 Arrhenius plot of diesel PM on coated and non-coated fleece

3.4. Effect of catalyst coating on diesel PM oxidation

Finally, diesel PM was oxidized on the non-coated and coated metal fleece (nDDI and cDDI in the graphs, respectively) using the same conditions as before. This is to directly investigate the impact of the catalyst on the oxidation of engine-borne PM. The impact of the catalyst on disordered carbon with hydrocarbons will also be seen here.

Fig.17 shows the mass conversions of diesel PM with and without the coated metal fleece. The curves again seem quite similar between the coated and the uncoated cases, however there is a noticeable difference in the slopes with the coated cases having steeper slopes. This is confirmed by the Arrhenius graph in Fig.18. The activation energies were calculated to be 128 kJ/mol and 90 kJ/mol for the diesel PM on the non-coated and coated metal fleece, respectively. The catalyst coating decreased the activation energy by 30%. This is the case even though a major advantage of using CeO₂ as a catalyst is its ability to adsorb NO₂, however the only gases used in here were N₂ and O₂, and in temperatures not high enough to produce NO₂.

It should be noted that the points in the Arrhenius graph are quite similar for the coated and non-coated cases except for a significant difference in the right most or lowest temperature oxidation. This is because the main advantage of a catalyst is that it can promote reactions at lower temperatures. This is clearly shown here. Another reason for this similarity is that the simultaneous oxidation of both the hydrocarbons and carbonaceous soot can dampen the real effect of the catalyst as the oxidation of the hydrocarbons is quite significant as seen without the coating when comparing the CBN330 and diesel PM. This will be shown in the final mass conversion analysis. It should also be noted that even though the points are quite similar for the uncoated and coated cases, the coated cases would produce a lower slope or lower activation energy without the last case due to the larger difference in the y-axis.

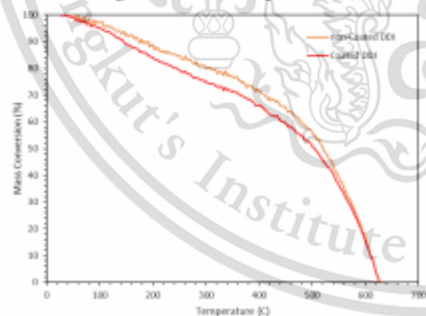


Fig.19 Non-isothermal mass conversion of diesel PM on coated and non-coated fleece

To further analyze how the coating changed the oxidation behavior, a non-isothermal mass conversion was done as seen in Fig.19. There is some mass loss before 100°C from the evaporation of the moisture on the PM. Then the mass loss is more significant after this as the hydrocarbons are oxidized. Finally, the largest mass loss comes after 500°C where the carbonaceous soot is oxidized.

It is obvious from the figure that the catalyst coating allows faster hydrocarbon oxidation seen by the significant gap before 500°C. The shift towards the significant carbon oxidation for the coated case also occurs before the non-coated case. However, it is indistinguishable after around 550°C as it seems to reach a limit of the catalyst's effect. This confirms the right most point in Fig.18 being most different when comparing between the non-coated and coated cases.

4. CONCLUSIONS

The metallic microfiber fleece from a partial-flow diesel particulate filter were coated using RF Sputtering with CeO₂ to catalyze the oxidation of diesel soot particles trapped on the fibers. The non-coated fibers were analyzed with SEM and EDS before being coated. After the coating, it was analyzed with SEM again and with X-ray diffraction for its chemical composition and with thermogravimetric analysis for the catalyst performance using carbon black and diesel soot from a light duty engine. The following results were obtained.

1. Metallic microfibers can be effectively coated with RF sputtering and with a ceramic CeO₂ target.
2. The catalyst coating on the microfibers reduced the activation energy of the soot oxidation by 17% for CBN330 and 30% for diesel PM.
3. Coating by RF sputtering can form an effective catalyst.

Reference

- (1) R. Brück, P. Hirth, M. Reizig, P. Treiber, J. Breuer: Metal Supported Flow-Through Particulate Trap; a Non-Blocking Solution, SAE Technical Paper (2001), 2001-01-0925
- (2) S. Okawara, S. Taji, M. Inoue, T. Itatsu, T. Nohara, K. Komatsu: Soot trapping and continuously oxidizing behavior by flow-through Metallic PM filter, SAE Technical Paper (2005), 2005-09-28
- (3) V. Meille: Review on methods to deposit catalysts on structured surfaces, Applied Catalysis A-general (2006), vol. 315, p. 1-17
- (4) X. Wang, H. Wang, Q. Huang, Z. Du, X. Huang, C. Jiang, S. Zhou: Magnetron sputtering nichrome on fiber fabric to construct microwave-absorbing structure, Applied Physics A (2020), vol. 126, p. 863
- (5) H.-Y. Lee, S.-I. Kim, Y.-P. Hong, Y.-C. Lee, Y.-H. Park, K.-H. Ko: Controlling the texture of CeO₂ films by room temperature RF

magnetron sputtering, *Surface and Coatings Technology* (2003), vol. 173, p. 224-228

(6) C. Guillen, J. Montero and J. Herreso: Anatase and rutile TiO₂ thin films prepared by reactive DC sputtering at high deposition rates on glass and flexible polyimide substrates, *Journal of Material Science* (2014), vol. 49, p. 5035-5042

(7) P. Karin, W. Amornprapa, P. Watanawongskorn, E. Saenkhumvong, C. Charoenphonphanich, K. Hanamura: Effect of soot particle size on four ball metallic wear using electron microscopy image analysis, *International Journal of Automotive Technology* (2020), vol. 21, no. 3, p. 579-589

(8) S. Mohankumar, P. Senthikumar: Particulate matter formation and its control methodologies for diesel engine: A Comprehensive Review, *Renewable and Sustainable Energy Reviews* (2017), vol. 80, p. 1227-1238

(9) H. M. Oo, P. Karin, C. Charoenphonphanich, N. Chollacoop, K. Hanamura: Physicochemical characterization of direct injection Engines's soot using TEM, EDS, X-ray diffraction and TGA, *Journal of the Energy Institute* (2021), vol. 96, p. 181-191

(10) P. Karin, H. Oki, K. Hanamura, C. Charoenphonphanich: Nanostructures and Oxidation Kinetics of Diesel Particulate Matters, *Journal of Research and Applications in Mechanical Engineering* (2012), vol. 1, no. 2, p. 3-8



APPENDIX D :

International Journal Submission

Effect of Metallic Microfiber Flow Through Diesel Particulate Filter System on Diesel Engine's Particle Emission Physicochemical Characteristics

Ban-seok Oh¹, Poonnat Thaeviriyakul¹, Watanyoo Phairote¹, Mek Srilomsak¹, Chinda Charoenphonphanich¹, Watcharin Po-ngen², Sompong Srimanosaowapak³, Katsunori Hanamura⁴, Preechar Karin^{1*}

¹School of Engineering, King Mongkut's Institute of Technology Ladkrabang, Bangkok 10520, Thailand

²Faculty of Technical Education, King Mongkut's University of Technology North Bangkok, Bangkok 10800, Thailand

³National Metal and Materials Technology Center, National Science and Technology Development Agency, Pathum Thani 12120, Thailand

⁴School of Engineering, Tokyo Institute of Technology, Tokyo 152-8550, Japan

* Corresponding author: preechar.ka@kmitl.ac.th

Abstract

It is well known that Particulate Matter (PM) from diesel compression ignition engines are harmful to the environment and to human health. To reduce engine PM emissions, exhaust after-treatment systems are utilized. A basic high-performance system can be composed of a diesel oxidation catalyst (DOC) and diesel particulate filter (DPF). This study used a system composed of a DOC and a partial flow DPF. Partial flow refers to how only a portion of the exhaust gas is filtered using metal fibrous filters instead of the full flow using ceramic filters. The PM deposited on the side wall of the stages of the system were investigated with respect to elemental composition, morphology, and nanostructure. This was to determine the effect of each component on the PM. The elemental composition analysis found traces of the engine lubricant oil in the PM collected before entering the DOC. This was then eliminated by the DOC and the remaining PM was not significantly impacted by the exhaust after-treatment system. The morphology and nanostructure show an interesting relationship where the size of the single primary particles increased while the graphitic nature of the carbon in the PM seemed to decrease. This can be explained by the simultaneous nature of partial trapping and partial oxidation that occurs in the partial-flow DPF. The emission measurements of opacity, temperature, CO₂, NO, and O₂ from each position also supports this.

Keywords: P-DPF, PM, Soot, Carbon Nanostructure, Exhaust after-treatment, Diesel Emissions

**APPENDIX E :
AUTHOR BIOGRAPHY**

Author: Mr. Ban-seok Oh
Nationality: Republic of Korea
Place of Birth: Bangkok, Thailand
Email: 63601189@kmitl.ac.th

Education:

2022 Master of Engineering, Automotive and Advanced Transportation Engineering, Faculty of Engineering, King Mongkut's Institute of Technology Ladkrabang, Bangkok, Thailand

2020 Bachelor of Science, Engineering (Mechanical Concentration) with Minor in Business, Calvin University, Grand Rapids, MI, USA

Conference Participation and Publications:

- 1) B. Oh, P. Karin, M. Srilomsak, K. Chonvasin, W. Po-ngen, S. Srimanosaowapak, and K. Hanamura, "Characterization of Biodiesels and Tire Derived Particulate Matters in Morphology and Nanostructure.", 14th AUN/SEED- Net Regional Conference on Materials & 4th International Postgraduate Conference on Materials, Minerals and Polymer, 2021
- 2) B. Oh, P. Karin, M. Srilomsak, W. Po-ngen, S. Srimanosaowapak, W. Wongpisan, and K. Hanamura, "Thin film Ceria Using RF Sputtering on Metal Fibers for Catalyzing Diesel Soot Oxidation.", 2022 JSAE Annual Congress (Spring), 2022
- 3) B. Oh, P. Thaeviriyakul, W. Phairote, M. Srilomsak, C. Charoenphonphanich, W. Po-ngen, S. Srimanosaowapak, K. Hanamura, P. Karin, "Effect of Metallic Microfiber Flow Through Diesel Particulate Filter System on Diesel Engine's Particle Emission Physicochemical Characteristics.", Submitted, 2022